A Robotic Platform for Internal Inspection

B. Alexander Cope

Thesis Paper submitted to the faculty of the Virginia Polytechnic Institute and State University in partial fulfillment of the requirements for the degree of

Master of Science

In

Mechanical Engineering

Alfred L. Wicks (Chair)

Corina Sandu

Steve Southward

November 22, 2012

Blacksburg, Virginia

Keywords: Mobile Robot, NDE Inspection, Internal Inspection, Robotic Crawler

A Robotic Platform for Internal Inspection

B. Alexander Cope

Abstract

This thesis describes the design of a robotic inspection tool which is based on a differential track-drive platform. The robotic inspection tool is a one man-portable UGV that has been developed for the purpose of non-destructive evaluation (NDE) and internal inspection of environments where human penetration may be difficult or hazardous. Various NDE and sensing techniques are described in this paper but the focus is on the mechanical and electrical design of the platform itself. The platform is a versatile device for mobile robotics research and development that supports a wide variety of instrumentation and payloads. Variable height control of the payload is achieved with a scissor lift assembly that provides accurate positioning of equipped sensors and instrumentation. The architecture of the platform was designed to support future autonomous implementations.

Acknowledgments

To my parents and family; thank you for your support all of these years. You have provided me with a set of underlying skills and principles that have allowed me to succeed. I would not be where I am today if it weren't for you guys and for that I'm thankful.

My appreciation goes out to my committee members Dr. Steve Southward and Dr. Corina Sandu. Thank for your diligent support, especially here towards the end.

Thank you Dr. O'Brien for your continuing support throughout this project and for providing the opportunity to prove my skills.

Thank you to all my fellow friends and coworkers in the Mechatronics Laboratory. I could have never completed this without everyone's insight. Special thanks goes to John Bird for his fantastic introductory courses Mechatronics I & II that teach the fundamental basics of which have allowed me to excel.

I'd like to thank Patrick Currier who was a fellow PhD student here at Virginia Tech before graduating and accepting a faculty position at Embry Riddle Aeronautical University. Patrick, your demeanor has always demonstrated vast amounts of professionalism and excellence. I attribute credit to you for the majority of my hands on skills and commonsense that I have acquired during my time in this program. You always had a positive outlook on everything and you are great person to be around. Thank you for everything you have done for me.

Most importantly, thank you Dr. Wicks for all the time and effort you have spent with me and for continuing to provide guidance to the endless cycle of students at Virginia Tech. You have provided me with many incredible opportunities and experiences that have allowed me to continue to improve upon myself. I think it is import for you to know that my respect for you is immense. I have always had a drive for success, but your push has forced me to prove to myself that I can accomplish anything if I apply myself and put my mind to it. Your ability to challenge me is phenomenal and for that I thank you.

Table of Contents

List of Figures

List of Tables

Chapter 1: Introduction

There is a need for a robotic inspection platform capable of transporting onboard instrumentation for testing and development of new technology and computer algorithms. This work will focus on a robotic inspection tool platform that was developed for the purpose of internal inspection through non-destructive evaluation (NDE) of hazardous environments or environments where human penetration is not feasible. NDE is critical for many applications because it improves efficiency and economical cost as compared to conventional inspection methods that may require invasive techniques. Improved documentation records can also be achieved over conventional inspection methods.

The focus of this thesis is on the robotic platform itself and not on the instrumentation or software required for NDE inspections. Characteristic features of the platform are reviewed and the overall construction is outlined. Figure 1 displays the robotic inspection tool designed at the Virginia Tech Mechatronics Laboratory:

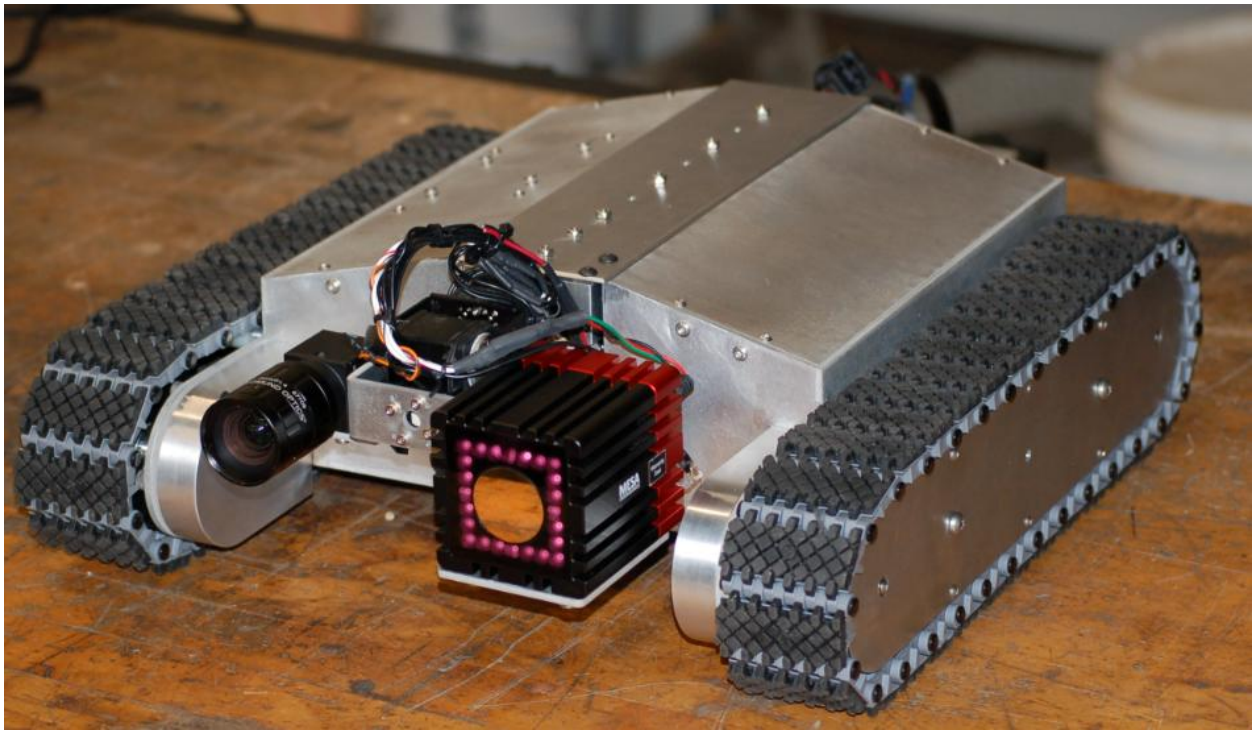

Figure 1 - Robotic inspection platform for NDE of hazardous environments.

The robotic inspection tool consists of a differential drive platform with a scissor lift for raising and lowering of the instrumentation package. The chassis of the inspection tool is a five piece aluminum unit

with a rigid design. Overall construction with associated FEA torsional analysis is discussed. The mechanical design of the tracks is outlined as well. The mechanical design of the inspection tool is discussed in Section 3.2.

The electro-mechanical design, discussed in Section 3.3, of the inspection tool includes powertrain design and motor selection for the drive motors and scissor lift motor. An overview of current DC motor technology is outlined and a complete analysis is provided for load requirements and component selection.

The electrical design of the inspection tool consists of drive camera selection, onboard controller selection and architecture, communications selection and architecture, and power distribution. Each is discussed in detail in Section 3.4.

Finally, the inspection tool capabilities are demonstrated in Section 4.3 by completing a NDE inspection of a test environment. An overview of the overall performance of the inspection tool including maximum operating speed and maximum angle of inclination is discussed. The performance of the scissor lift is outlined and a vibrational analysis is shown in Section 4.2 of vibrations seen by the instrumentation package.

Chapter 2: Literature Review

Many robotic systems exist for various tasks that are difficult, dangerous, or tedious. These robots have been utilized in industry for many decades. Examples of these robots are the cartesian or gantry robot, cylindrical robot, spherical or polar robot, SCARA robot, articulated robot, and parallel robot. They can handle dangerous chemicals, perform assemblies in manufacturing environments, and lift oddly shaped, heavy objects. These robots do not make errors related to fatiguing and are capable of working continuously until the end of their service lives [1]. Although these robots have been around for decades, they are fixed in location or confined to their work station or manufacturing plant.

Other robots do, however, exist based on mobile platforms that have a wide variety of capabilities. These mobile robotic systems are finding their way into all sorts of environments in which previous systems could not breach. Mobile robots have the capability to perform various inspection tasks in a given environment without being fixed to one location. More and more mobile robotic systems are replacing difficult, dangerous, or cumbersome tasks that were previously performed by human workers. This is because technology such as robot vision, perception, sensing and instrumentation continues to improve as manufacturing capabilities and computing power increases year after year.

Inspection robots for use in hazardous environments can be very useful as opposed to a human inspector. Robotic systems can enter dangerous environments that may be unsafe for a human and documentation records are more complete and more consistent. Humans tend to have biased reasoning for most any task. Therefore, when multiple human inspectors are involved with the same inspection at different points in time, the same inspection may provide different results. This means that a documented inspection varies based on the technician conducting the inspection. Integrating a robotic inspection system into a given application removes the human bias allowing for consistent inspection results. The focus of this chapter is to provide an overview of potential hazardous environments and the mobile robot platforms that are used in those environments, as well as the most common sensing capabilities of these platforms.

2.1 Hazardous Environments

The focus of this section is to provide an overview of possible hazardous environments that an internal inspection tool may encounter where human inspection is just not feasible. Many applicable environments exist so only the most common are discussed.

2.1.1 Commodity Pipelines

In Western Pennsylvania the first petroleum line in the world was laid down during the year of 1862. Ever since then pipelines have spread rapidly and have been used to transport various commodities all over the world. Examples of these commodities are crude oil, natural gas, water, ammonia, hydrogen, steam, gasoline, powdered coal, butane, coffee beans, beer, and many more. The largest of pipelines are operated in a similar manner to railroads. They have many branches and terminals that control the direction and synchronization of flow. These intricate pipelines prove to be a very efficient means of transportation as opposed to other methods. Pipelines do not have to transport the weight of themselves from and to their destination, where as rail cars, tanker ships, and tractor trailers do. There is also a reduction in loss of product from evaporation and the product remains safer underground [2]. An example of a commodity pipeline is shown in Figure 2 and Figure 3.

Figure 2 - Shown is an elevated section of the Trans-Alaska Pipeline. [Public Domain]

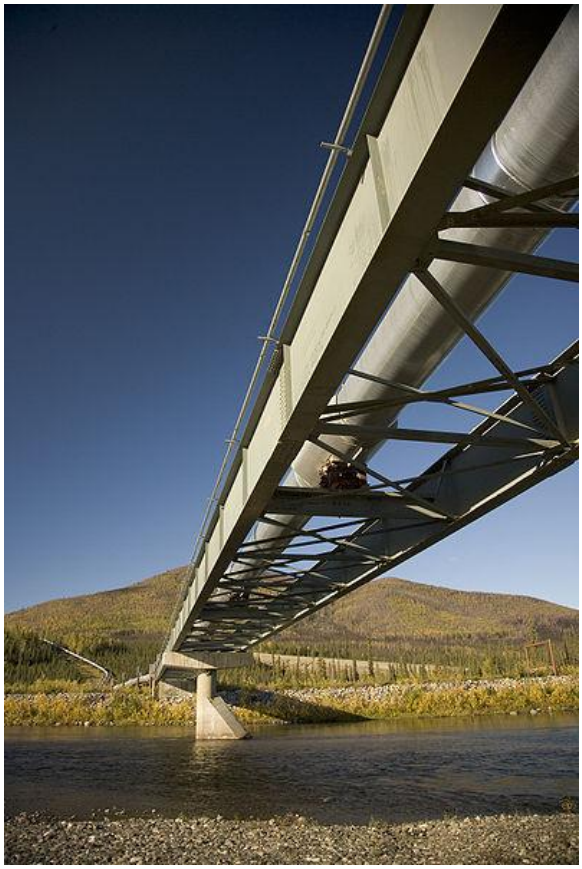

Figure 3 - This is a section of the Trans-Alaska oil pipeline crossing the South fork Koyukuk River [Public Domain].

In today's world, accurate and reliable assessments of pipelines are needed due to today's stringent regulations and intensive fiscal pressure. As operators continue to discover new integrity threats, systems must be in place to mitigate and locate these threats. As a result, inline inspection tools that incorporate differing technologies must be run to assess and inspect as resourcefully as possible. The majority of inspections are done without stopping the flow of the product in the pipeline and the flow itself is the primary means of propulsion.

Inline inspection tools are currently used that incorporate a variety of differing technologies to complete an inspection of a pipeline. This is because the primary propulsion system for many pipeline inspection tools is the flow of the commodity itself. Therefore, multiple data sets are collected simultaneously from these deferring technologies allowing the inspection tool to make only a single run. The data sets gathered usually include mapping of the pipe, deformation measurements for bore and strain calculations, and diameter sensors for verification of material loss and surface conditions [3]. Inspection technologies vary with magnetic and ultrasonic methods most common. Other techniques used are visual inspection, X-ray, and eddy currents [4].

2.1.2 Urban Water Environments

Other hazardous environments that are similar to commodity pipelines exist. Urban water pipelines and sewer networks are complex networks that are located in every town and city. These pipelines are generally very structured environments. However, lack of global planning due to the expansion of these networks over time has led to many special challenges when overcoming the navigation of their interior. Older towns tend to suffer more from this because part of the network was installed long ago without the standards that have been established today. Current networks suffering with this issue may consist of pipes with unknown diameter reductions, nonlevel joints or welding defects, or blockages from welding defects and deposits [5]. Figure 4 shows a sanitary sewer from a manhole access point.

Figure 4 - Shown is a sanitary sewer pipeline. [Public Domain]

These networks can be difficult to inspect with a humans and may contain various gases such as methane, carbon dioxide, and other toxic substances.

2.1.3 Military Hazardous Environments

Robotic inspection tools are used more now than ever to hunt for chemical and nuclear weapons as well as clearing improvised explosive devices (IEDs) from roads and cars. Ever since the catastrophic event on September 11, 2001, mobile robots are finding purpose performing tasks such as structural inspections

and detection of hazardous materials in environments where human presence is unsafe. Other examples are hazardous site cleanup in disaster areas, inspection of caves and mines, and remote reconnaissance of vehicles, roads, and buildings [6]. Figure 5 demonstrates soldiers in Afghanistan searching for roadside IEDs using handheld detectors.

Figure 5 - Soldiers search for roadside IEDs in Afghanistan. [Fair Use, http://www.defencetalk.com/threat-of-terrorist-ieds-growing-44728/]

These soldiers could be removed from harm's way by replacing the manned inspection with a mobile robotic system.

2.2 Robotic Platforms

Many motion mechanisms have been developed to date. Some utilize a passive propulsive system and others use an active drive mechanism. Passive drive inspection tools are used in pipelines where the flow of the commodity provides the propulsion for the inspection tool. This process is known as pigging, where pipeline inspection gauges (pigs) are used to perform these inspections. An example of a pig is shown below in Figure 6.

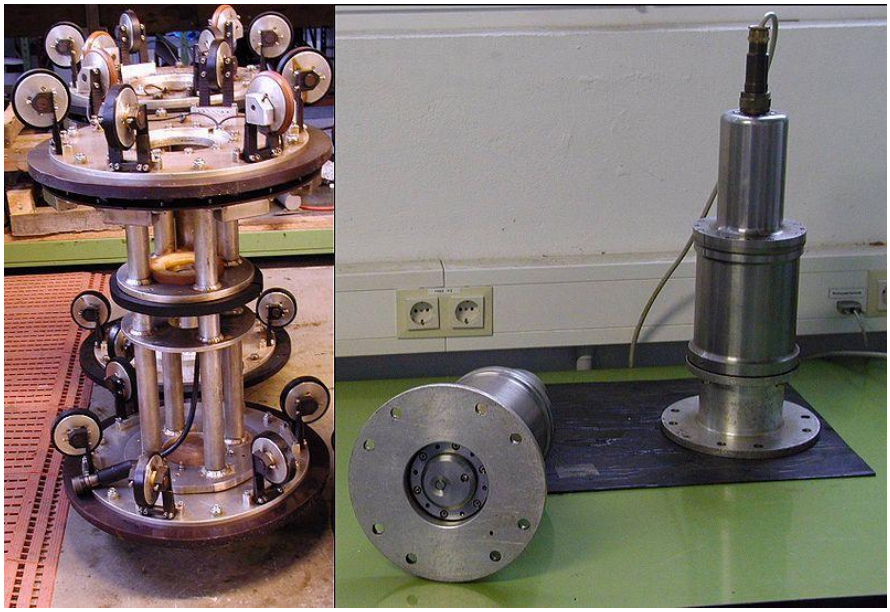

Figure 6 - Ultrasonic measuring heads are utilized on this crack detection pig [Public Domain]

Pigs are loaded into a pig launcher, where the pressure is equalized with that of the pipeline before released. The pig is then captured at the destination point where the pig is depressurized and removed via the receiver. Shown in Figure 7 is a pig launcher/receiver. The empty concrete blocks shown in front of the pipe flanges are where the pig traps are bolted down for capturing and insertion of the pig [4].

Figure 7 - Pig launcher/receiver utilized by a natural gas pipeline in Switzerland [GNU Free Documentation License – photographed by Audrius Meskauskas]

Other robotic platforms utilize different types of active driving mechanisms such as wheeled, tracked, legged, inchworm, snake, and screw types [7]. Oya and Okada have developed a steerable, wheel-type, flat robot that presses against the interior wall of a pipe while still allowing for obstacle avoidance. [8]. Bradbeer, Harrold, Nickols and Yeung developed a legged platform that utilizes pneumatic actuated legs for walking and positioning inside a pipe [9]. Choi, Park, and Jung have developed an inch-worm mechanism for locomotion of a feeder pipe inspection robot that consists of gripper, translation, and rotation actuators [10]. However, this robotic system is affixed to the outside of the pipe and is therefore limited to above ground pipelines. Anthierens, Ciftci, and Betemps designed an inch-worm platform that is capable of internal traversing up vertical pipes [11]. Rome, Hertzberg, Kirchner, Licht, and Christaller developed a five-segmented, articulated robot that contains active joints for flexibility [12]. More recently, Nassiraei, Kawamura, Ahrary, Mikuriya, and Ishii have developed a fully autonomous pipe inspection robot called KANTARO [13]. KANTARO utilizes a patented naSIR drive mechanism that has four wheels parallel with the horizontal plane, each independently controlled.

Outside of academia, many companies have been founded that develop remote inspection robots for inspection applications. Inuktun Services Ltd., a Canadian company founded in 1989, develops remotely operated vehicles that are used for internal inspection. Inuktun has a wide variety of crawlers that are modular and can be equipped with various components. Inuktun crawlers use differential track drive as the drive mechanism of choice [14]. Pure Technologies developed a similar robotic inspection platform called PureRobotics which are modular systems capable of transporting multi-sensor configurations [15]. Finally, Envirosight manufactures the ROVVER line of configurable inspection crawlers that have many different chassis, wheel, and camera configuration options [16].

As for inspection robots used in hazardous military environments, many different platforms exist. One example of a platform that is commonly used to perform a variety of different tasks and carry many different sensors and instrumentation is the iRobot PackBot. The PackBot has been used to clear IEDs as well as detect hazardous gas, radiation, and chemical weapons in military environments where human inspection should be avoided [17]. Figure 8 shows the Packbot equipped with IED detection hardware where its primary function is for explosive ordnance disposal.

Figure 8 - iRobot's Packbot is used for explosive ordnance disposal. [Public Domain]

2.3 Sensing Technology

This section focuses on the sensing and instrumentation techniques used for NDE internal inspections. An understanding of these technologies is required as there may be platform accommodations that need to be considered when selecting a base platform. The sensor technology selected for an inspection can directly impact the design of a base platform. It can impact the power distribution such as power supplies and power conversion electronics. It can impact the weight and size of the base platform which influences the selection and power requirements of motors and actuators. It may also have an impact over the control techniques and hardware that is required to support positioning of the sensors. Investigation of these sensing technologies should be completed before the build of a base platform. This section outlines the most common sensing technologies used for NDE inspections.

2.3.1 Magnetic Flux Leakage

Magnetic flux leakage (MFL) has been the most commonly used NDE technique for decades. In 1933, the first MFL technique was performed by Watts [18]. The inspection tools are equipped with magnets which generate a magnetic field. The pipe interacts with the magnetic field and effectively distorts the flux lines of the field. Refer to Figure 9.

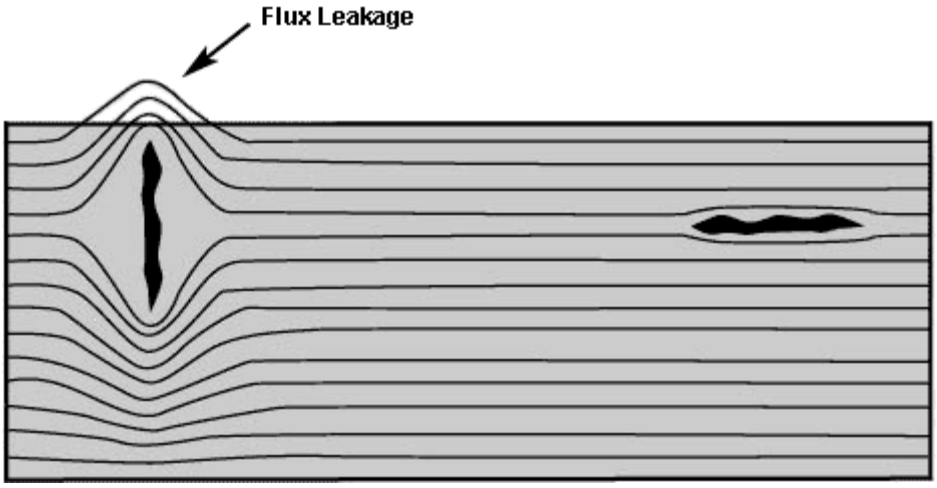

Figure 9 - Shown is magnetic flux line distortion from defects within a material. [Fair Use, www.ndt-ed.org]

The field is then recorded and the data analyzed for anomalies. In earlier days, the flux leakage was detected through the use of induction-coil sensors but today high resolution Hall effect sensors are used. MFL techniques can find missing material or corrosion as well as mechanical damage due to plastic deformation. MFL does have some disadvantageous such as product flow restriction or permanent magnetization of the pipe [19] [20].

2.3.2 Ultrasonic Testing

Ultrasonic testing (UT) techniques are another common technology used to provide similar data as MFL. Ultrasonic pulses are directed into the pipe wall and the reflected signal is collected. Refer to Figure 10. Arrival time, amplitude, and attenuation among other signal properties can be extracted from the return signal. This is commonly used to determine pipe geometry, wall thickness, and internal flaws.

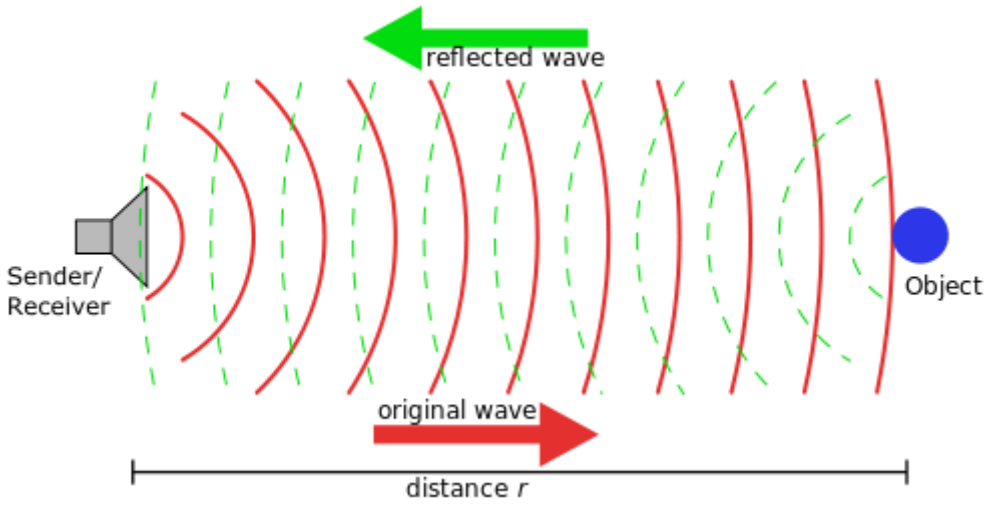

Figure 10 - The UT technique emits a wave and measures the return signal. [GNU Free Documentation License, drawing by Georg Wiora]

This technology does not work well with dirty pipes such as crude oil lines where paraffin build-up may be present [20]. Ultrasonic frequencies generally vary based on the application from 0.1 MHz to 50 Mhz. As the transducer frequency is increased the wavelength is effectively shortened and the working resolution is increased. However, larger frequencies are typically associated with larger acoustic attenuation. An appropriate frequency is usually selected based on the application where there is a compromise between wave length and attenuation [4]. More recently, a new ultrasonic technology called ultrasonic phased array has been introduced to the field. Figure 11 shows a technician testing a pipeline weld for defects using an ultrasonic phased array.

Figure 11 - A technician checks a pipeline using an ultrasonic phased array for weld defects [Public Domain].

Previously applications utilized multiple independent transducers where each transducer was specifically oriented in order to send pulses in a given direction. The ultrasonic phased array consists of an array of transducers where each element in the array can be controlled through electronic adjustment. The cooperative pulse generation between the elements in the array determines the overall pulse beam direction which allows for focusing at any desired points. Linear, matrix-shaped, circular, and annular phase arrays exist. The most common and economical are linear arrays [21].

2.3.3 Eddy Current Testing

Eddy Current Testing (ET) is a non-destructive testing method that can determine crack detection, size and material variations. Eddy currents are created when a conductor experiences a change in a magnetic field and as a result electrical currents are induced within the conductor. This change can be the intensity or direction of a magnetic field at any point within the conductor. An example of this would be to apply an alternating current to a coil where the intensity of the coil's magnetic field depends on the

frequency of the alternating current. The changing magnetic field would cause eddy currents to flow in a conductor. These eddy currents then induce their own magnetic fields that can cause repulsive or attractive effects. Refer to Figure 12

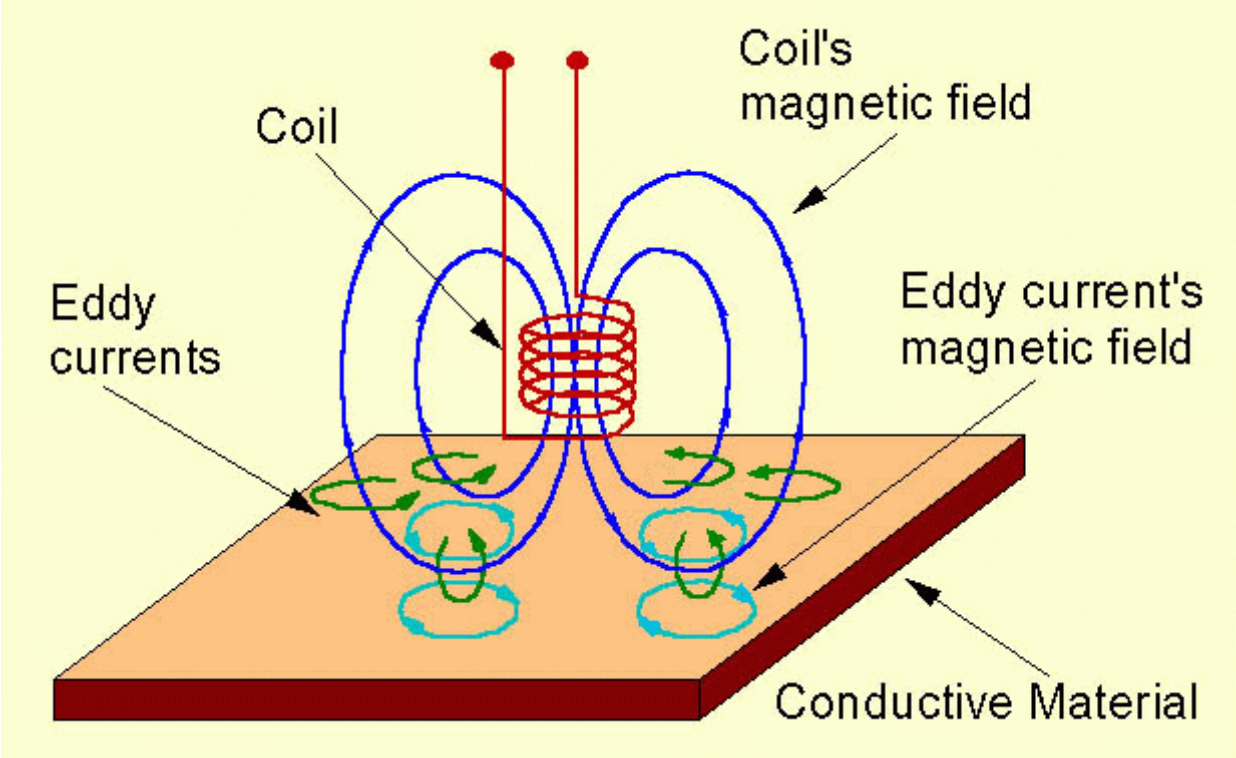

Figure 12 - Eddy currents are generated in a material during directional or intensity related magnetic field changes. [Fair Use, www.ndt-ed.org]

When magnetic waves are introduced by exciter coils in the axial direction of a pipeline, eddy current is induced along a circular pathway in the pipe on the radial plane. The flow is the detected by a detector coil and the shape of the received eddy currents can then be analyzed for material flaws. ET is an efficient method in terms of time and cost. Also, if coating or insulation is present there is no need for removal [22] [23]. ET sensors are now printed in array form using printed circuit microfabrication techniques. The sensors are highly reproducible because the windings are fabricated on a substrate that is thin, flexible, and very conformable. The detector windings used for sensing the response are usually located on the opposite sides of the primary windings on the same sensor. The simple layout of the windings generally allows for frequency ranges from 1 kHz and 40 MHz [24].

2.3.4 Laser Range Finders

Another depth measuring method is available using laser light. This technology is primarily used for surface imaging and reconstruction relative to internal inspection. However, laser distance measurement devices can also be used for object avoidance, path planning, and many other applications useful for mobile robotics. Three basic techniques exist, each of which have advantages and disadvantages. There is also a wide variety of 1D, 2D, and 3D laser measurement systems.

The more common is the time-of-flight measurement where the laser source is pulsed and a receiver measures the time it takes for the emitted signal to return. With the speed of light remaining constant, the travelled distance of the light pulse can be determined. With a relatively small form factor for the required electronics, this method is great for long distances but does have some limitations. The resolution of the travelled distance is limited by the timing circuit of the embedded electronics that are responsible for timing the return of the emitted signal. Timing circuits are currently in the range of pico-seconds and resolutions for current sensors available on the market are usually between 1 cm and 2 cm. An example of the time-of-flight laser range finder is the point-and-shoot device that many golfers use to determine the distance from the ball to the tee. This is a 1D device and returns a single value for depth. 2D line scanning time-of-flight sensors exists that are equipped with either a rotating or oscillating mirror that allow for consecutive incremental measurements on a single plane. Figure 13 shown demonstrates the use of a SICK 2D LIDAR equipped on a mobile robot. In this particular case the LIDAR is scanning on the horizontal plane parallel to the ground

Figure 13 - Shown is a mobile robot equipped with a SICK single plane laser scanner. [Public Domain]

Another technique used is the phase shift measurement where a continuous wave of laser light is emitted and the reflected signal is received. The phase shift between the two signals is then measured. Phase shift is proportional to distance but is only relative. The frequency of the emitted laser light must then be tuned in order to achieve the appropriate wave length for a given measurement range. Many devices utilize multiple modulated frequencies to achieve the desired range. Phase shift devices tend to offer high data rates and high accuracies.

The last method utilizes the triangulation principle where the emitter is placed at a known distance relative to the receiver. A laser signal of light is emitted and the reflected signal is collected. Instead of recording the time-of-flight, the angle of return of the light is measured at the receiver. Refer to Figure 14.

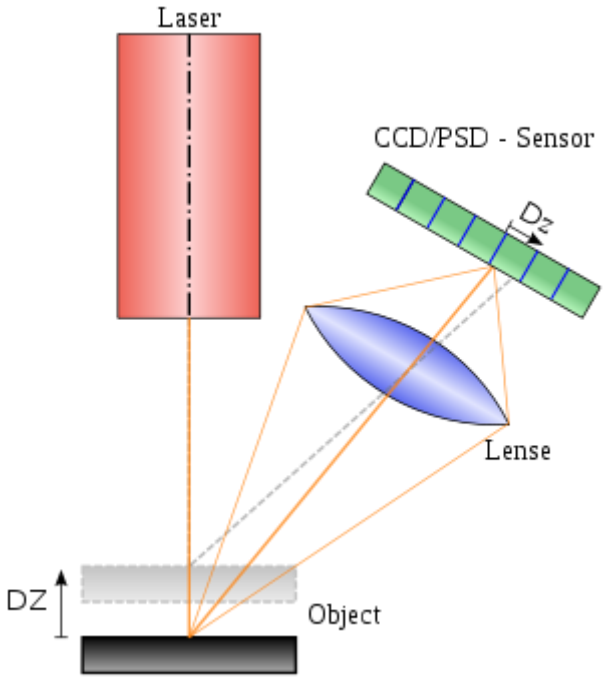

Figure 14 - Laser triangulation basic principle. [GNU Free Documentation License, drawing by Georg Wiora]

With the known relative distance between the emitter and receiver and the angle of return of light, simple geometry is used to calculate the depth. This method provides extremely accurate results and is used widely in industry for industrial inspection. However, there are some limitations similar to that of stereo vision. The device must be tuned for a specific working range. This is because the device has a working depth that is a function of the distance between the emitter and receiver. As with stereo vision, the larger that distance, the larger the initial depth (effectively a blind spot) before the start of the

working range. The method is used on 1D and 2D devices. 2D devices generally include a single row of pixels on a CDD.

3D laser measurement devices are generally an extension of 2D systems by adding some form of actuation. Many forms of actuation configurations exist such as rotation about the yaw, yaw-top, roll, or pitch axis. However, other methods do exist such as that used by the MESA Imaging flash LIDAR shown in Figure 15.

Figure 15 - MESA Imaging SR4000 Flash LIDAR.

This device is similar to a camera where an array of pixels lies on a focal plane inside the device. The reflected light is then focused onto the array of pixels. The flash LIDAR can then emit a point cloud of depth data of which the density depends on the number of pixels available [25] [26].

2.3.5 Structured Light

Structured light is another form of 3D surface imaging that consists of a visual camera and a structured light pattern projector. The pattern projector is required because traditional cameras and image sensors provide only 2D images that lack depth information. The structured light illumination is projected onto the scene and captured with the visual camera. Given a 2D planar surface, the structured light illumination seen by the camera will appear very similar to that of the projected pattern. With a 3D surface, the projected pattern is distorted and this distortion is captured by the camera. The distortion

can then be processed and accurate 3D surface profiles are extracted from the distortion of the projected structured light. This processing is done using the triangulation principle allowing for differentiation of a single projected light spot from the acquired image. For this to be possible the relative position of the camera to the structured light pattern projector must be known. The camera and pattern projector are positioned at known distances from each other and both must be calibrated for a given working range. Field of view, camera resolution, standoff distance, lens distortion, and projector intensity are all factors in the resolution and accuracy of the extracted 3D surface profile. Figure 16 demonstrates a structured light 3D imaging setup. Notice the separation between the pattern projector and the camera.

Figure 16 - Shown is a structured light sensor developed at JPL [Fair use, http://trs-new.jpl.nasa.gov/dspace/bitstream/2014/39375/1/05-3907.pdf].

3D surface imaging using the structured light approach is used for many applications. Facial imaging, dental imaging, surgical planning for plastic surgery, and reverse engineering, are all relevant applications just to name a few [27].

2.3.6 Stereo Vision

Another optical method to collect 3D information is stereo vision. 3D surface imaging using stereo vision requires two cameras. The cameras are fixed at a known distance apart. Using triangulation, two images of the same scene from different perspectives can lead to the difference in coordinates, or disparity, of features in the scene. This is similar to structured light except that rather than using a single point or matching a single pixel, stereo vision algorithms process regions instead. With known disparity maps of a scene, image processing can extract depth data and provide 3D information. This is very similar to how the human brain interprets depth information from the human eyes.

Depth resolution of a stereo imaging system is determined by the distance between the cameras and the camera focal length. Increasing the distance between the cameras will increase depth resolution but can also create blind spots up close to the stereo rig. Too much separation can also bring objects hidden behind other objects into the view of one camera but not the other. Depth resolution can also be increased by increasing the number of pixels on the imager, effectively shrinking the size of each pixel on the imaging sensor [26].

Chapter 3: System Design

This chapter focuses on the inspection platform design. This includes the mechanical design and construction of the chassis, tracks, and scissor lift assembly. The electro-mechanical design of the motors and powertrain for the tracks and scissor lift is reviewed and the pan/tilt actuators for the payload are discussed. The electrical design and component selection for the drive camera system, communications, onboard controller, and power distribution is outlined as well.

3.1 Platform Selection and Requirements

The inspection tool was designed based on the following requirements:

- Must perform internal NDE inspections

Visual camera systems and mapping hardware are likely to go on the platform as well as other sensors that may be required for a particular environment. The base platform must be capable of transporting this hardware at 2 in/sec and transmitting data though a tether in real-time via gigabit Ethernet network.

- Applicable to a wide range of possible applications

Versatility is important requirement for the inspection tool platform. It is likely that the inspection platform may encounter many different hazardous environments. The base platform must be capable of transporting a wide variety of instrumentation to accommodate the NDE inspections.

- Remain one man-portable as to simplify logistics

Logistics is important. To simplify logistics for transportation, the robotic inspection tool must remain one man-portable where one operator is required to set-up and assemble, perform NDE inspections, and disassemble without the need of further assistance. The base platform itself must weigh no more than 20 lbs.

- Provide variable height control over the instrumentation package

The instrumentation package may need to be repositioned in real-time relative to the base platform. Therefore, a method to actively position a payload in order to achieve the appropriate inspection position is required.

- Fit through a 6 inch x 20 inch x 20 inch restricted opening

The inspection tool may encounter height restriction in some environments. The variable height control method that is required from above must utilize a method that allows for collapsing of the instrumentation package below 6 inches. The base platform footprint must also be less than 20 in. x 20 in.

- Traverse unknown environments with difficult terrain

The base platform may encounter difficult terrain in some environments and must provide a means of traversing that terrain. The base platform must climb slopes greater than 30 degrees from the horizontal and provide enough power to traverse rough terrain.

- System architecture must support future autonomous implementations

Some environments that require similar inspections on a regular basis may allow for semi-autonomous or autonomous inspections where the operator is removed from the control loop. The base platform must have a system architecture that supports autonomous implementations. Active control is then required for motors, sensors, and other electronics. This means that feedback must be available from these components.

3.2 Mechanical Design

The following sections focuses on the mechanical aspect of the design process based on the requirements listed above. This includes the chassis, tracks, and scissor lift apparatus.

3.2.1 Chassis

The chassis of the inspection tool is a five piece unit that is constructed of standard stock 1/8 inch plate aluminum 6061. There is a front, back, bottom, and two identical sides as shown in Figure 17. Each panel was constructed with a series of notches, such that the entire unit fits together like a puzzle. The panels were then clamped in place and welded together.

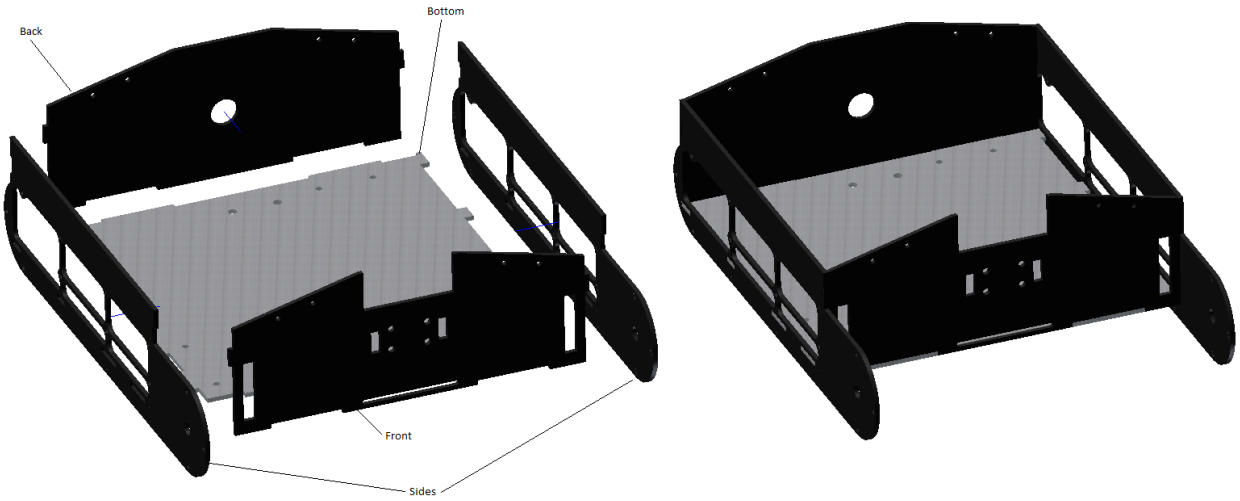

Figure 17 - Five piece chassis for inspection tool.

Stress analysis for various loading conditions was performed on the bare bone chassis to insure structural rigidity. Autodesk Inventor Stress Analysis Environment was used for the analysis which is based on a linear, static analysis with the following assumptions [28]:

- There is a linearly proportional relationship between load, deflection, and stress.
- Linear material properties exit; the stress-strain is linear and proportional to strain, therefore there is no yielding of the material.
- Static loading conditions exist.
- Dynamic loading effects are neglected.
- Temperature effects are neglected.
- Dimensions of the part are large compared to deformation.
- Buckling is neglected

An analysis utilizing these assumptions is by no means the most accurate method, but it does greatly simplify the process while still providing a great rough estimate for quick prototyping. The Autodesk Inventor Stress Analysis Environment uses the finite-element analysis (FEA) method to provide stress related results. FEA work began in the late 1940s with the work of Hrennikoff, McHenry, and Newmark. They used a lattice of beam-like elements for the solution of stresses in the field of structural mechanics. In 1943, Courant then suggested that through interpolation over triangular subregions (elements formed by connecting nodes), a piecewise polynomial method could effectively allow for a solution by solving stiffness equations in matrix form. This means a mesh must be applied to a geometry by that

contains a network of elements and nodes that discretize a region. The stress analysis shown in this section utilizes simplex triangular mesh and can be seen in Figure 18.

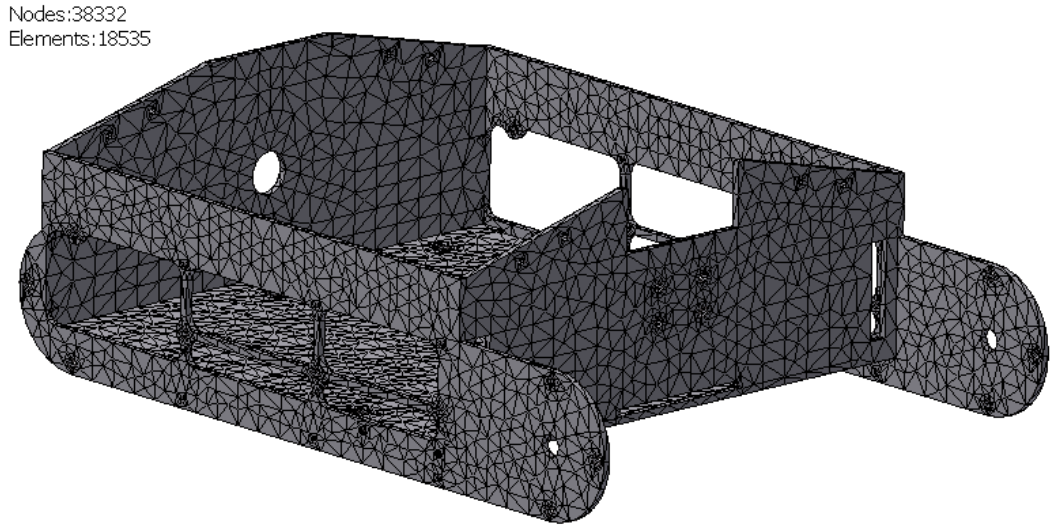

Figure 18 - Chassis with applied mesh network of nodes and elements.

There are some problems with a triangular mesh network because simple triangular elements pose two primary issues that introduce error. First, modeling of complex geometries with lots of curved surfaces is difficult because the element has sides that remain straight, resulting in poorly modeled curved surfaces. The second issue is that the average strain needed for a solution is approximated at the center of each element. These flaws create errors that are incorporated into the results. However, these sources of error can be reduced by using a higher mesh density with many more elements and nodes. As computational power has increased over the years, other geometric elements such as the 8-node quadrilateral shape have been used for specific applications and improved results. These advanced elements can model curved surfaces and provide a higher-order function for the strain distribution, but large computation power is required [29].

The first analysis done on the bare bone chassis was conducted where opposite loads of 10 lbf was applied at the front axle locations. The rear panel of the chassis was fixed such that motion in all directions of the rear panel was constrained. This applies a moment of 98.75 lb-in about the y-axis.

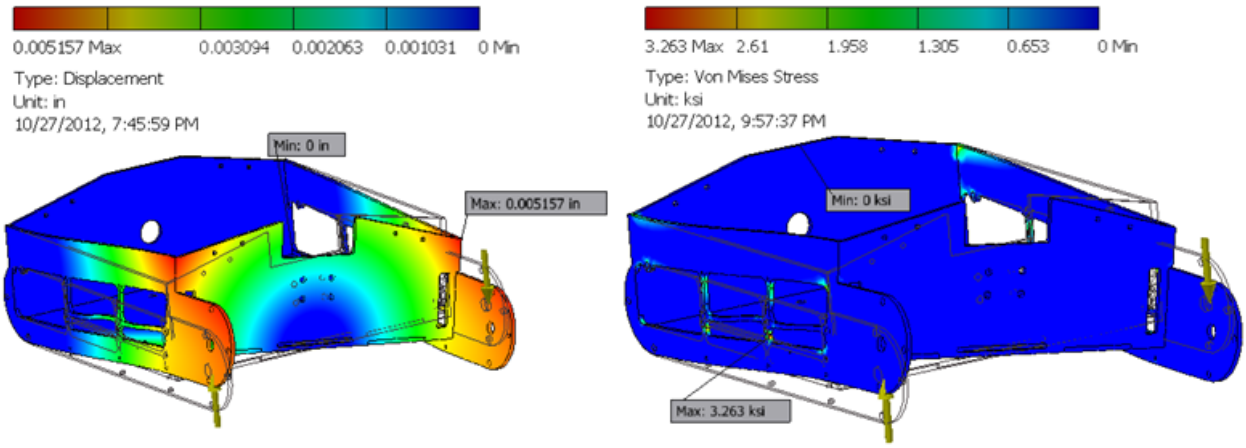

Figure 19 - Chassis deformation and stress results when equal but opposite loads of 10lbf are applied at front axle locations.

Figure 19 shows the displacement results with the applied loads. A displacement function is associated with each element in the FEA process. By using force equilibrium conditions, a stiffness matrix and relating nodal forces are calculated and the displacements are obtained. The stiffness matrix consists of all elements effectively modeled as linear springs with a spring rate. Through an iterative process, the nodal forces and displacements are calculated along with the strain and stress of each element, and a solution is converged upon.

Figure 19 also displays the von Mises stress analysis under the torsional load conditions. The von Mises stress is based on a distortion-energy theory which predicts that under simple tension or compression, yielding will occur when the distortion strain energy reaches or exceeds the material yield distortion strain energy. The von Mises stress is derived using the three principal stresses along the three principal axis and is usually thought of as a single, equivalent stress that represents the entire general state of stress [29]. Using the maximum von Mises stress located at the chassis side panel cross-member, the minimum Factor of Safety (FOS) was analyzed. The FOS can be calculated using the material ultimate tensile strength S_y, and the maximum allowable stress σ_{max}:

$$\text{FOS} = \frac{S_y}{\sigma_{max}} \tag{3.1}$$

$$\text{FOS} = \frac{45\text{ksi}}{3.263\text{ksi}} = 13.79$$

The minimum FOS for this particular loading condition was calculated using the ultimate tensile strength of aluminum 6061 and the maximum von Mises stress from Inventor's stress analysis. The minimum FOS

is 13.79 and is located at the cross member of the chassis side panel. This is the point at which failure would occur if the load for this condition was increased 13.79 times. An FOS of one would occur when maximum stress is equal to the yield stress of the material, causing plastic deformation.

3.2.2 Tracks

Tracks were selected as the primary means of propulsion. Tracks have advantages and disadvantages. Wheels are generally preferred when tracking odometry as skid-steer tends to provide inaccurate results when using sprocket rotation to calculate travelled distance. However, many environments may be dirty, have uneven surfaces, or contain serpentine paths. Utilizing tracks will help the inspection tool to distribute its weight evenly over a larger surface area while maintaining the largest contact patch possible. Uniform weight distribution is advantageous in areas of poor traction or when traversing steep inclinations and uneven surfaces. Tracks require a set of treads that provide good traction for the vehicle. An off-the-shelf solution of tracks, 9-link sprockets, and hubs was selected from Lynxmotion for the inspection tool. The treads consist of rubber with a Shore A hardness fixed to polypropylene links. These tracks, shown in Figure 20, have a fixed center-to-center distance because the maximum speed of the inspection tool is a slow 2 in/sec.

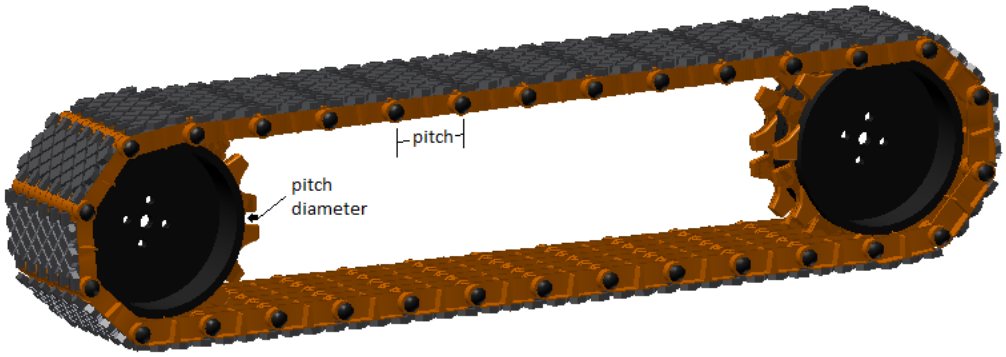

Figure 20 - Lynxmotion tracks and sprockets used on the inspection tool.

With this slow speed, an active spring loaded tensioner is not necessarily required. Although an adjustment for the center-to-center distance could be incorporated into the design, such an adjustment would also add complexity. Instead, the center-to-center distance was predetermined. To calculate the distance from the front axle to rear axle, or center-to-center distance *c* of the sprockets, the following formula can be used:

$$c = \frac{(pitch\ length)(\#\ of\ links) - \pi(pitch\ \emptyset)}{2} \tag{3.2}$$

A total of 30 track links were used for the inspection tool. Using a pitch length of 1.07 inches and pitch diameter of 3.13 inches from Lynxmotion (calculated, not measured) [30], the center-to-center distance was calculated to be 11.13 inches. This is not the true center-to-center distance from one axle to the other because there is some play between each link. This is because the links are held together at the pivot point with polypropylene rods held in place by snap rivet fasteners on the outside (these are the black fasteners you see around the outside of the track in Figure 20). These polypropylene rods have a clearance fit which slightly adds length to the track perimeter. The actual center-to-center distance was found to be approximately 11.375 inches with a cardboard mockup assembly and physically measuring the appropriate distance.

The tracks are 2 inches wide and are supported by a set of nylon rollers that ride on 1.5 inch standoffs. These standoffs are supported by an outer track cover and the chassis sides. Track spacers constructed out of 3/8 inch aluminum and machined with CNC was used to create the appropriate clearance for the tracks to ensure they do not rub on the side of the chassis. These components are displayed in Figure 21 below:

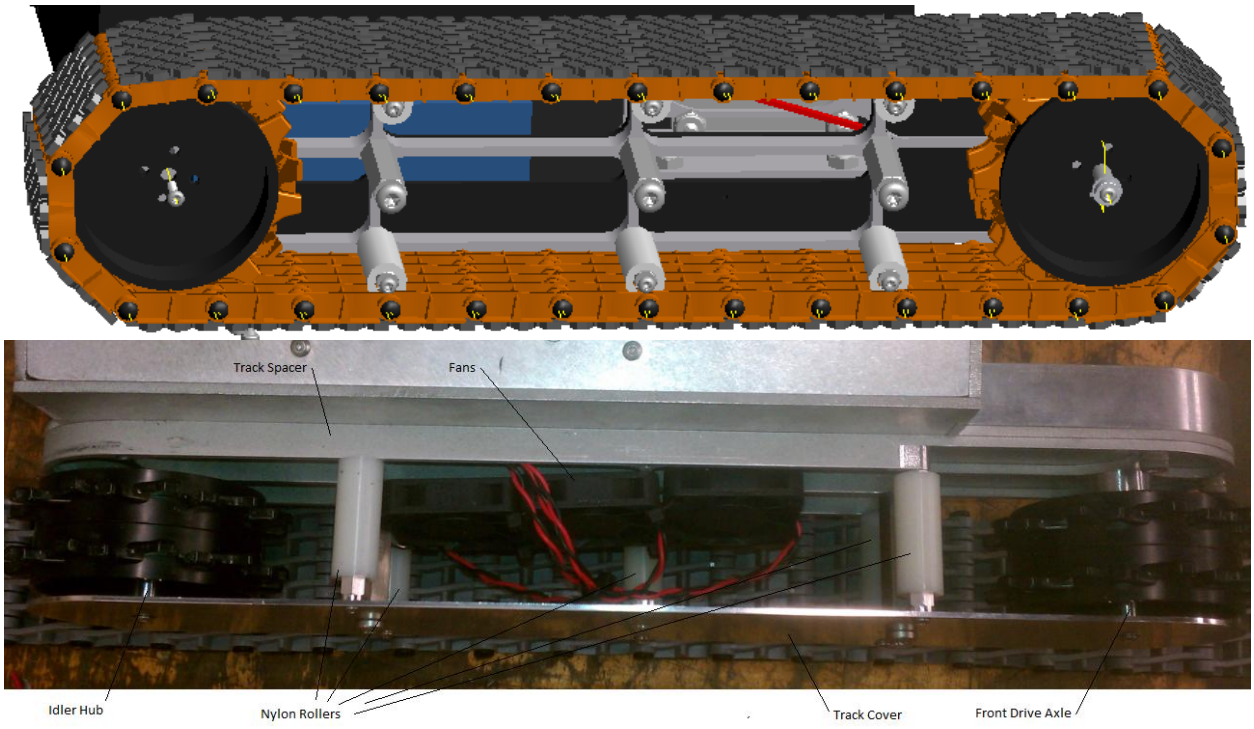

Figure 21 - Track assembly without treads

The rear axle is a passive idler hub that was also supplied from Lynxmotion and is designed for mounting of a single set of sprockets. The axle has bearings on each end that are supported by the track cover and track spacer, which are 1.5 inches apart. The front axles were custom machined to support the drivetrain required for the drive motors (Section 3.3.2). The drive shaft ends are supported by the same bearings supplied from Lynxmotion. To add extra support to the drive shaft, an oil-impregnated bronze bearing was press fit into the track spacer and chassis side.

3.2.3 Scissor Lift

A need to raise the instrumentation package during inspection in order to achieve the appropriate vantage point led to the development of the scissor lift apparatus. The payload was estimated to weigh no more than 5 lbs (1.1kg) which led to the initial requirement of a 5lb payload. To accomplish this task, a lifting mechanism was developed that consists of three primary components:

1) The scissor lift assembly
2) The linear guide rail and payload mount
3) The lead screw assembly

Figure 22 below shows the scissor lift assembly which effectively raises the instrumentation package 7.5 inches above resting position. The top of the payload mount at resting position sits approximately 5.5 inches above tarmac and with the lift fully raised, the payload is at 13 inches above tarmac.

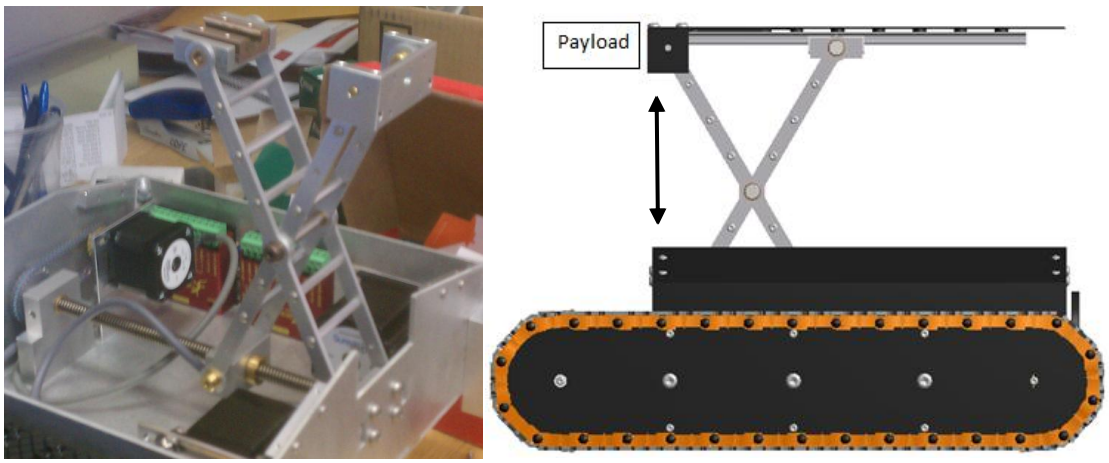

Figure 22 - Scissor lift assembly

The scissor lift itself consists of four equal length members approximately 8 inches long and pinned at the middle and ends. These members are water jetted out of 1/8 inch aluminum plate. In order to

ensure structural rigidity, the inner scissor members are fixed with 1.5 inch standoffs and the outer scissor members are fixed with 1.75 inch standoffs. The hex standoffs are standard off-the-shelf components which the majority of the major catalog companies carry in stock. As the scissor lift raises and collapses, the member ends will need to pivot as well as the pinned joint located at the center of the scissor lift. These joints are vital to proper operation of the lift. To reduce play and ensure the lift remains rigid, off-the-shelf components were selected for the joints. Bronze oil impregnated flange bearings were press-fit at each joint into countersunk, predrilled holes. Shoulder bolts were then used for the pivot axles. The use of standardized off-the-shelf bearings and shoulder bolts is critical to ensure proper tolerances, reduce play in the joints, and allow for proper operation.

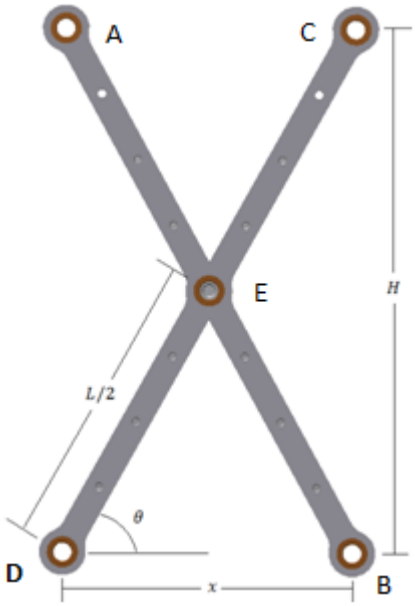

Figure 23 – Geometric relationship of scissor lift

The following equations can be formed:

$$\theta = \cos^{-1}\left(\frac{x}{L}\right) \tag{3.3}$$

$$H = L\sin\theta \tag{3.4}$$

Figure 23 demonstrates the geometric relationship of the scissor lift. Assuming that all scissor lift members are of equal length and pinned at the middle, AE, BE, CE, and DE are then equal in length. The angle θ can be solved for by modifying the length x in Equation (3.3), length x being the distance

between point B and C. Plugging Equation (3.3) into Equation (3.4), the height *H* can be solved for. This represents the height of the payload from the axis of actuation located through point B and C.

A stainless steel lead screw was selected as the method of actuation to open and close the bottom ends of the scissor lift, effectively raising and lowering the unit. Many off-the-shelf solutions exist for linear motion, however the motor is generally coupled in line with the lead screw or linear rail. Additional length would have then been required for the chassis to support an off-the-shelf solution. To prevent this, a motor was coupled parallel with a stainless-steel standard off-the-shelf "locking" ACME lead screw with 12 TPI (turns-per-inch) that was placed along the axis of actuation through point B and C. The lead screw is 3/8 inches in size and the ends have been turned to ¼ inch O.D. for fitment inside the supporting pillow blocks. ¼ inch bronze oil impregnated bearings are used to reduce friction at the pillow blocks. The lead screw is supplied with an externally threaded nut that screws into an aluminum rectangular flange. This rectangular flange travels along the lead screw when the lead screw is rotated. Node C of the scissor lift is pinned at the front pillow block. Node B is pinned at the rectangular flange, which allows for direct control over the height of the scissor lift via lead screw rotation.

In order to keep the payload mount in a fixed position relative to the inspection tool chassis, a top plate attached to both ends at the top of the scissor lift is required. However, this plate is fixed in length while the scissor ends open and close. To allow for linear motion while still fixing the ends to the top plate, a commercial linear guide rail with carriage was selected from PBC Linear Motion which mounts inverted to the top plate. The carriage is machined and coated with a frelon friction reducing coating allowing for smooth motion along the rail. One end of the scissor lift is pinned to a bracket that attaches to the carriage and the other is pinned to the payload mount. Figure 24 shows the assembly.

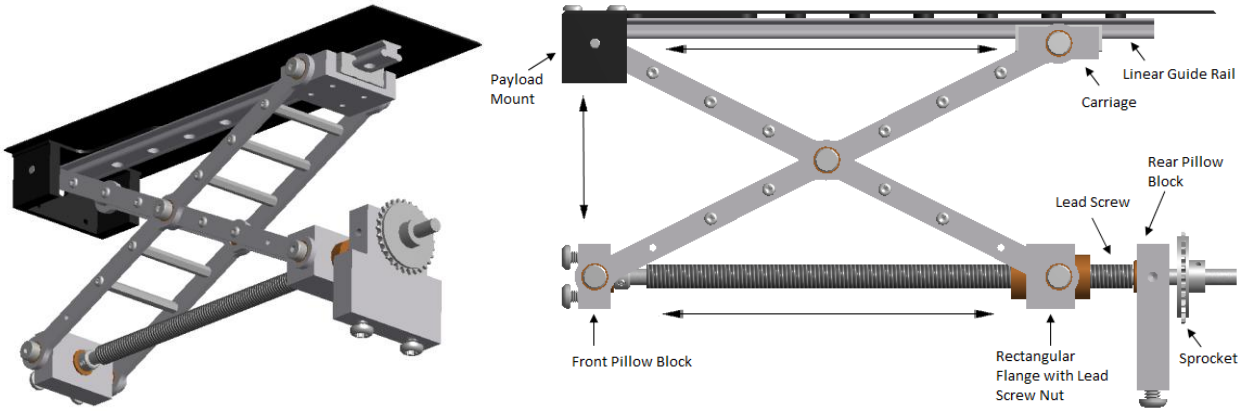

Figure 24 - Lead screw and scissor lift assembly with linear guide rail

The linear guide rail carriage supports 50 lbs hanging and 300 lbs upright at maximum speed. With a maximum payload of 5 lbs, the carriage will not to see a reaction load anywhere near its limits.

Selection of the appropriate motor for turning of the lead screw requires the knowledge of the horizontal reaction force acting at the lead screw nut. Figure 25 below shows the scissor lift structure with loads applied.

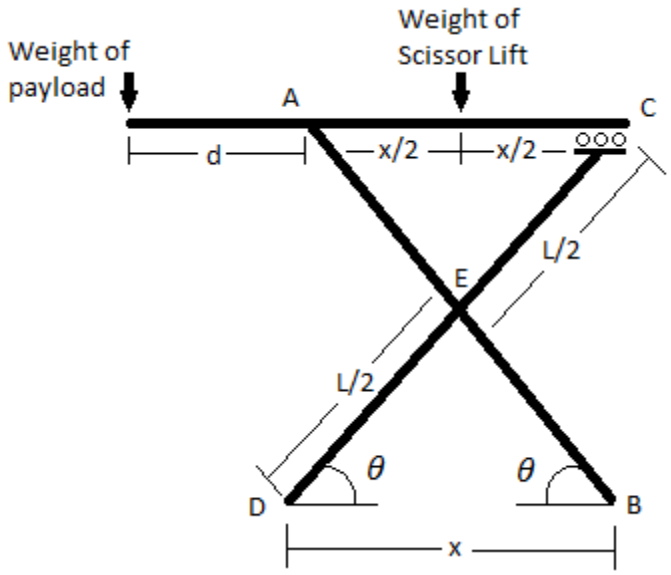

Figure 25 - Basic scissor structure with loads applied

The payload is modeled as a cantilever from point A where the scissor lift is pinned to the payload mount. To account for the weight of the scissor lift components, a load is applied equally between point A and C. When the scissor lift is fully raised and point C is closest to point A, a moment is applied about point C from the weight of Scissor lift top and linear guide rail that also acts as a cantilever. That moment is less that 6% of the payload moment about point A and therefore is neglected for simplicity and not included in the model. The inspection tool is designed for inline inspection along a serpentine pathway. Therefore it is assumed that the inspection tool will not see more than a few degrees in roll and will not experience any lateral loads. In order to determine the maximum horizontal reaction force at the lead screw nut, a 2D static model of the scissor lift assembly must be solved through an iterative process with software such as MATLAB. The loads shown in Figure 25 must be traced down through the scissor lift members, solving for the reaction forces along the way. Newton's third law states that there is always an equal and opposite reaction for every action. This means that the action and reaction forces must be distinguished between by isolating the model and identifying the force exerted on the model.

There are a total of seven reaction forces in the static model requiring seven equations for a solution. To accomplish this, the model can be broken up into three free body diagrams [31]. Starting with the scissor lift top, the first free body diagram is shown in Figure 26 below:

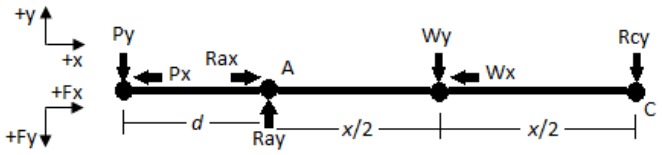

Figure 26 - Scissor lift top free body diagram

Summing the moments about point A will yield the solution of the reaction force R_{Cy} in terms of the known loads P_y and W_y.

$$\sum M_A = 0; \ -dP_y + \frac{x}{2}W_y + xR_{Cy} = 0$$

$$\therefore \quad \boxed{R_{Cy} = \frac{d}{x}P_y - \frac{1}{2}W_y} \tag{3.5}$$

Summing the moments about point C will yield the solution of the reaction force R_{Ay} in terms of the known loads P_y and W_y.

$$\sum M_C = 0; \ -\frac{x}{2}W_y + xR_{Ay} - (d+x)P_y = 0$$

$$\therefore \quad \boxed{R_{Ay} = \frac{1}{2}W_y + \left(\frac{d+x}{x}\right)P_y} \tag{3.6}$$

Summing the forces in the x direction yields the solution of R_{Ax} in terms of the known loads P_x and W_x:

$$\sum F_x = 0; \quad -P_x + R_{Ax} - W_x = 0$$

$$\therefore \quad \boxed{R_{Ax} = P_x + W_x} \tag{3.7}$$

The second free body diagram required for a complete solution is shown below in Figure 27. This diagram includes both scissor lift members. The scissor lift is modeled in static equilibrium which means that reaction forces must be reversed while transitioning from one member to another. This is why R_{Ay}, R_{Ax}, and R_{Cy} are reversed in Figure 27.

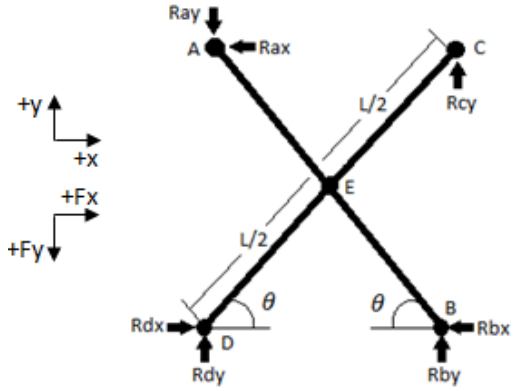

Figure 27 – Assembled scissor free body diagram

Summing the moments about point D will yield the solution forR_{By}:

$$\sum M_D = 0; \quad -L\cos(\theta)\,R_{Cy} - L\cos(\theta)\,R_{By} - L\sin(\theta)\,R_{Ax} = 0$$

$$\therefore \quad \boxed{R_{By} = -R_{Cy} - \tan(\theta) R_{Ax}} \tag{3.8}$$

Summing the forces along the x direction:

$$\sum F_x = 0; \quad R_{Dx} - R_{Ax} - R_{Bx} = 0$$

$$\therefore \quad \boxed{R_{Dx} = R_{Bx} + R_{Ax}} \tag{3.9}$$

Summing the forces along the y direction:

$$\sum F_y = 0; \quad R_{Ay} - R_{By} - R_{Cy} - R_{Dy} = 0$$

$$\therefore \quad \boxed{R_{Dy} = R_{By} + R_{Cy} - R_{Ay}} \tag{3.10}$$

Notice that the reaction forces are canceled out at the pinned joint located at point E.

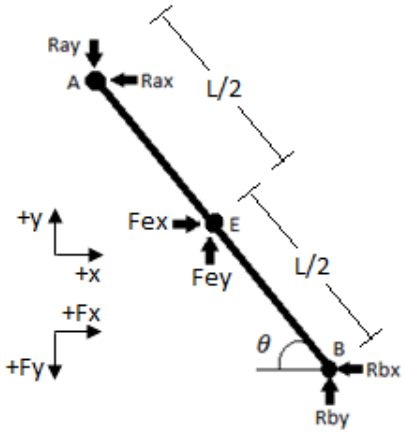

Figure 28 - Single member free body diagram

Summing the moments about point E:

$$\sum M_E = 0; \quad -\frac{L}{2}\cos(\theta)\, R_{Ay} - \frac{L}{2}\cos(\theta)\, R_{By} + \frac{L}{2}\sin(\theta)\, R_{Bx} - \frac{L}{2}\sin(\theta)\, R_{Ax} = 0$$

$$\therefore \quad \boxed{R_{Bx} = \cot(\theta)\, R_{Ay} + \cot(\theta)\, R_{By} + R_{Ax}} \tag{3.11}$$

A requirement for the inspection tool is to climb slopes up to 30 degrees. As mentioned earlier, an iterative process is required to find the maximum load at the lead screw nut by solving the static model at all angles at different scissor lift heights. To accomplish this repetitive task, a scissor lift static solver was written in MATLAB and is included in Appendix II – MATLAB Code for Scissor Lift Static Solver. The static solver takes the loads P, W, payload height range, and slope range as inputs. The solver then iteratively determines the solution to the previous equations. The following set of graphs show the relevant results.

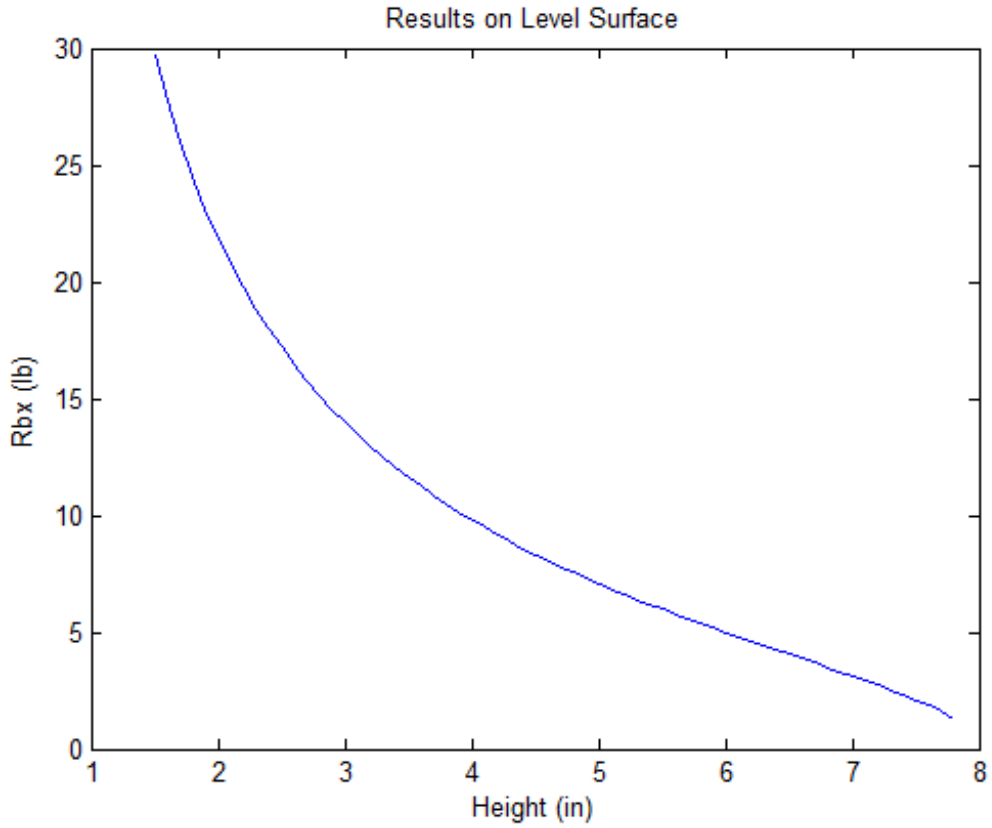

Figure 29 - Horizontal load on lead screw nut on level ground.

The results of the static solver shows that on level ground the horizontal load R_{Bx} on the lead screw is reduced as the scissor lift is raised. This is as expected because as the lift raises and the scissor members become more closely aligned with the vertical plane, more load is absorbed by R_{By} and less by R_{Bx}. This can be seen in Figure 29.

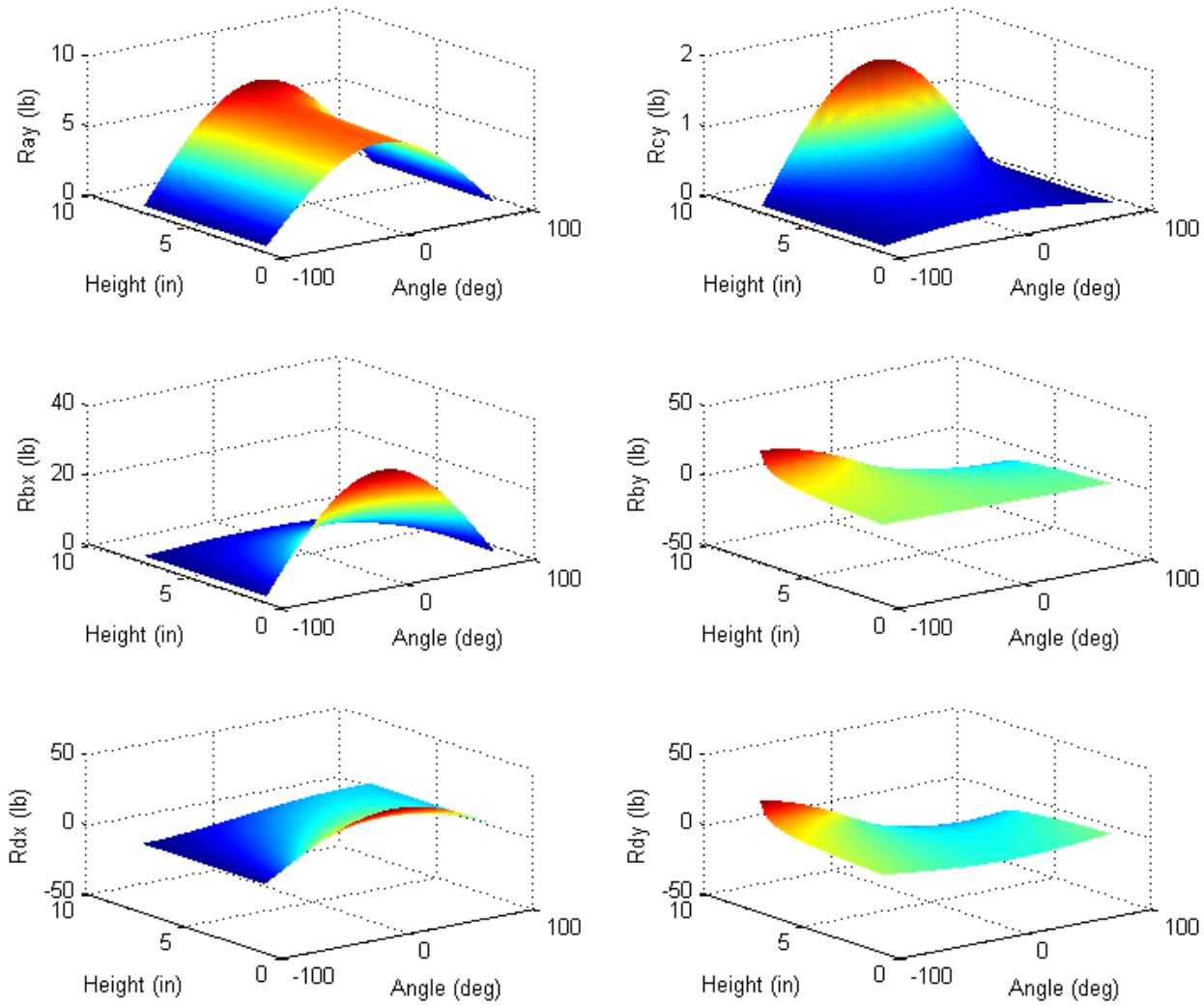

Figure 30 - Reaction loads as a function of scissor lift height and slope angle.

As you can see from Figure 30, R_{Ay} increases with scissor lift height yet decreases with slope angle in either direction. This is expected because as the lift rises, there is more of a vertical load transmitted down through the member. It is also expected that R_{Ay} decrease with slope angle because P_x and W_x have larger values which is absorbed by R_{Ax}. R_{Cy} is similar to R_{Ay} in that it experiences the same trends but with a far less drastic change. R_{By} and R_{Dy} both experience very similar trends where these reaction loads stay relatively the same when the scissor lift is fully collapsed. However, these reaction forces increase when the scissor lift is raised on a decline and decrease when the scissor lift is raised on an incline. R_{Dx} is equivalent to R_{Bx} except that it includes the R_{Ax} term which increases the load on an incline and decreases the load on a decline.

R_{Bx} is the term of most interest because this is the load experienced by the lead screw nut which directly influences the power requirements of the lead screw drive motor. R_{Bx} experiences its maximum load when the inspection tool sits on level ground. As the scissor lift is raised, that load is removed and instead absorbed by R_{By}. As you can see in Figure 31, the maximum load occurs at the scissor lift closed position and decreases with the angle of inclination or declination. The maximum load on the lead screw nut is just under 30 lbf.

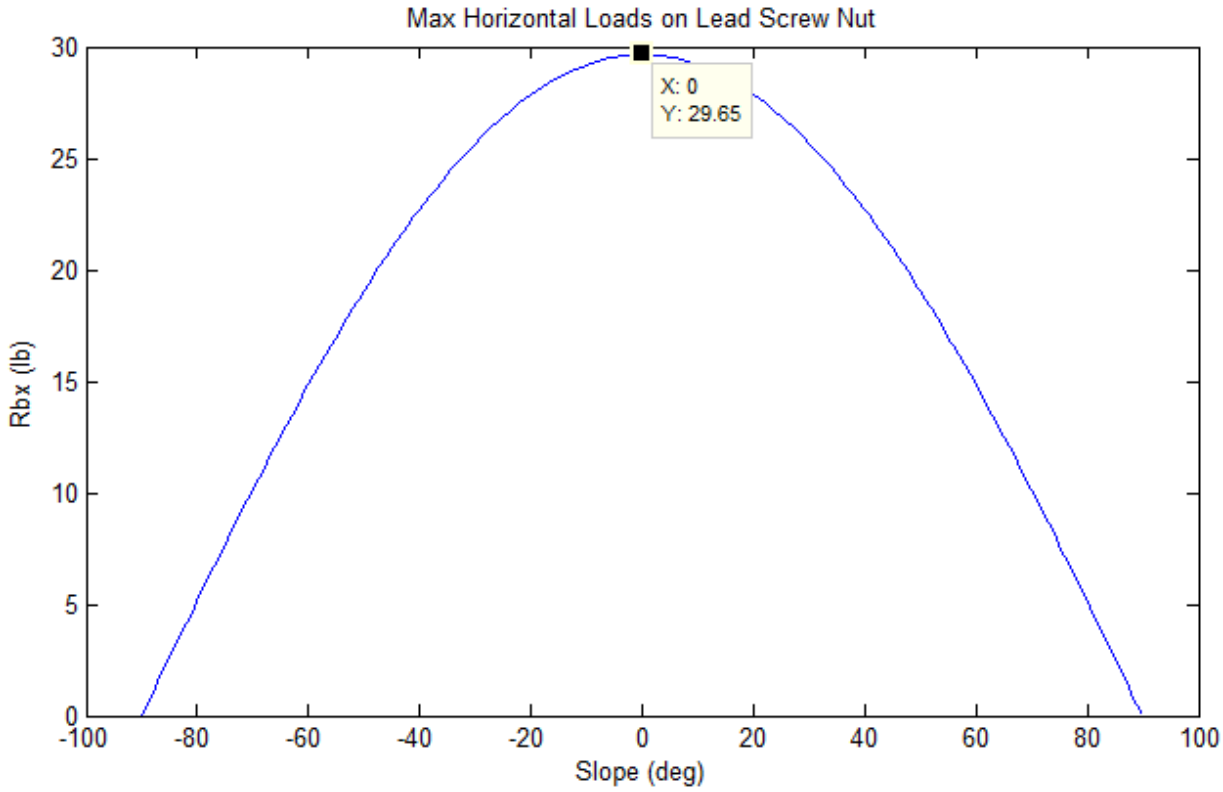

Figure 31 – Maximum horizontal load on lead screw nut.

3.3 Electro-Mechanical Design and Powertrain

This section focuses on electro-mechanical design of the powertrain for the scissor lift actuator and platform locomotion. This includes motor and powertrain component selection and load design.

3.3.1 Overview of DC Motor Technology

A wide variety of motors are available that may work to propel the inspection tool. The cost varies by manufacturer and type of motor. Manufacturers such as Maxon Motors and Faulhaber make reliable, robust motors that are found in many industrial and surgical robotic applications. Recently, DC brushless motors have taken the lead as the most technologically advanced motors for robotic applications. They use a permanent magnet external rotor with multiple phases of driving coils and Hall Effect sensors for positioning of the rotor. Electronic commutation based on Hall position sensors removes the need for direct contact with brushes. The absence of brushes allows for low electrical noise generation which is advantageous when sensitive electronics are nearby. With no voltage drop across the brushes, there is high efficiency as well as a flat speed to torque ratio which enables operation at all speeds with a rated load. Higher operating speeds are also achieved without brushes imposing mechanical limitations. Finally, electronic signals from the Hall Effect sensors can be used as feedback information just as you would expect from an encoder. The resolution is poor, but may be sufficient for a slow moving robot when the motor is geared with a large enough gear ratio. Brushless DC motors do, however, have a much higher cost of construction. Mechanical tolerances are tighter and the control is complex and expensive. Electronic controllers are required for operation and can sometimes run double the cost of the motor [32].

The classical brushed DC is less expensive alternative to brushless motors. The brushed DC motor has an armature which consists of a set of wire coils. When current is supplied, the armature acts as a bipolar electromagnet. Brushed DC motors use mechanical rather than electrical commutation and on the outside of the motor is a set of permanent magnets. The mechanical rotary switch, or commutator, reverses the direction of current when the rotor is turning to ensure the armature always pushes or pulls against the permanent magnets. Brushed DC motors are simple because only a simple two wire control is required. No controller is required for fixed speeds and when variable speeds are required, controllers are inexpensive. Brushed motors have a much lower cost of construction and due to the lack of electronics, are capable of operating in extreme environments. They have a moderately flat speed to torque ratio at low speed, but at higher speeds torque begins to fall off due to the friction of the brushes. EMI noise is common with brushed motors due to brush arcing effectively raising the noise floor of nearby sensitive electronics. Brushed DC motors also have higher rotor inertia and poor heat dissipation due to the internal rotor construction [32].

The stepper motor is another DC motor technology that is used in robotic applications. Stepper motors are actually brushless motors as well. Rather than rotating continuously when voltage is applied, stepper

motors have many electromagnets arranged around a gear-shaped rotor on the outside of the motor body. The electromagnets are consecutively energized, which effectively "steps" or turns the rotor. The number electromagnets and number of teeth on the rotor determine the angular resolution of each step. Stepper motors pack a lot of torque into a small volume and are designed for positioning capabilities without the feedback required by other motors. A motor that does not require feedback for position control is very advantageous for many robotic applications. Although stepper motors are brushless, there is a large difference in inertia between brushless DC and stepper motors. Stepper motors generally have 7-10 times the rotor inertia of brushless DC motors. Acceleration is much slower because of this and the torque generated drops off at higher speeds. They are also roughly double the weight [33].

3.3.2 Drive Motors and Powertrain

In order to select the motors for propulsion of the inspection tool, the amount of torque required to drive the tracks must be known. The exact amount of torque needed to drive skid-steer tracks is difficult to determine without physically measuring the amount required because all tracks are different and the amount of friction available for propulsion may vary from surface to surface. However, a very rough estimate can found with some simple calculations. Figure 32 below demonstrates the forces acting on the inspection tool when climbing up an incline.

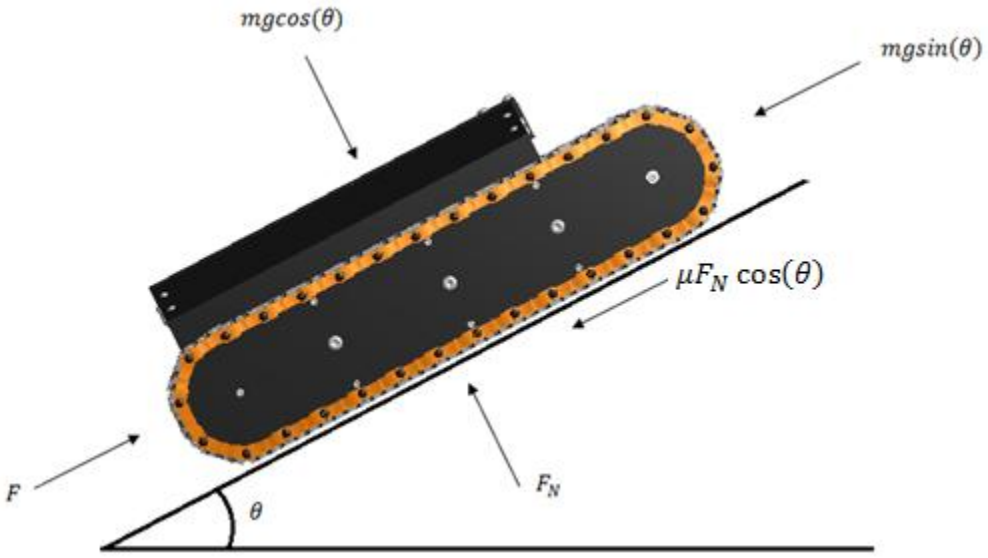

Figure 32 – Shown are the forces acting on the inspection tool when climbing an incline.

The inspection tool must have a method of propulsion capable of overcoming the force of gravity, friction, and track inefficiencies. The friction between the surface and treads is not known. Friction is represented by the term μ. Assuming a value of .8 for μ, an overall mass m of 9kg, and a 30° maximum angle of inclination, the force *F* required to propel the inspection tool up the incline is calculated as follows,

$$F = mg(\sin(\theta) + \mu\cos(\theta)) \tag{3.12}$$

$$F = (9kg)(9.81\,m/s^2)(\sin(30) + .8\cos(30))$$

$$F \approx 105.31N$$

The inspection tool was designed to operate at a maximum speed of *V = 2 in/sec.* Using the results from Equation (3.12), the power P required to provide that load at the given velocity is then calculated:

$$P = F * V \tag{3.13}$$

$$P = 105.31N * 0.0508m/s$$

$$P \approx 5.35W$$

The overall diameter of the tracks is used for the required torque calculation rather than pitch diameter because power is delivered at the outer rubber part of the tread that makes contact with the surface. This diameter is approximately 3.85 inches. The frequency of drive sprocket rotation at maximum speed must then be determined:

$$f = \frac{V}{D\pi} \tag{3.14}$$

$$f = (2\,in/sec)/(3.85in * \pi) = .1654hz$$

With two tracks, the torque required per track can be calculated using the result from Equation (3.13) and the angular frequency (ω) of the drive sprockets at maximum speed. Note that consistent units must be used and angular frequency must be in radians/sec:

$$2T = P/\omega \tag{3.15}$$

$$2T = 5.35W/(2\pi * .1654hz)$$

$$T \approx 2.58\ Nm \ldots \approx 365.36\ oz - in$$

The torque calculated with Equation (3.15) is a rough estimate of the amount of torque that is required at each drive axle in order to climb a 30° slope.

Instead of a direct drive system where the motor is coupled directly to the drive axle, a set of chain and sprockets were used transmit power from the motor located inside the chassis to the tracks. There is a slit on the front panel of the chassis for each chain to allow passage. The Flex-E-Pitch series cable chain and sprockets were selected from WM Berg. A wide variety of cable chains that consist of single or double stainless steel core are manufactured by WM Berg, These stainless steel cores are overmolded with a polyurethane plastic which is self-lubricating. The Flex-E-Pitch cable chains are zero backlash chains that are silent, positive drive chains [34].

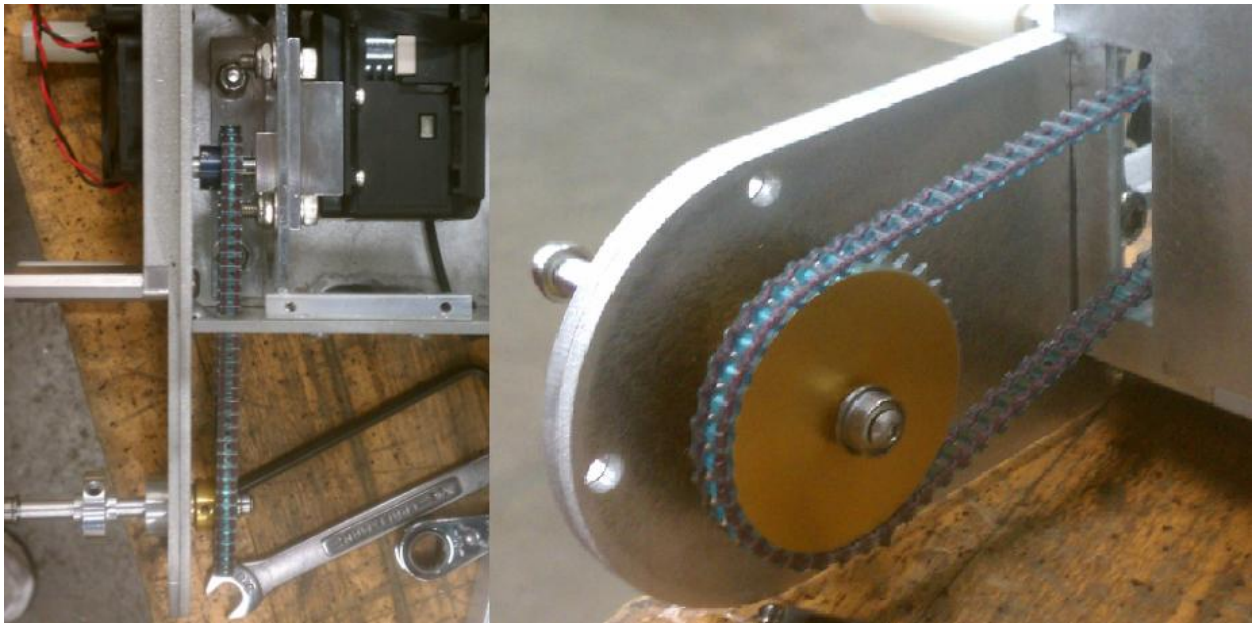

Figure 33 - Shown is the cable chain assembly from WM Berg used for the powertrain.

Utilizing a chain drive powertrain allows multiplication of the output torque from the motor through sprocket sizing. This is done by selecting a sprocket with fewer teeth on the motor output shaft, and a sprocket with more teeth at the drive axle shaft. The chain sprocket assembly is shown in Figure 33. A sprocket cover was machined with CNC in order to cover the driven sprocket which would otherwise be exposed outside the robot. The cover helps to protect the inspection tool operator's hands and fingers from injury that could occur while working with the inspection tool. This cover is shown in Figure 34.

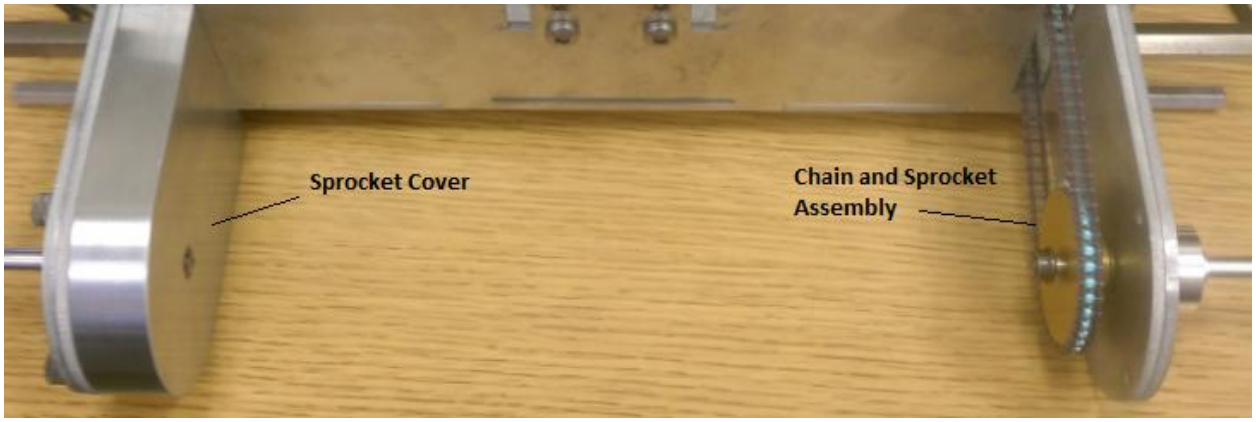

Figure 34 - Shown is the cover used to prevent exposure of the chain and sprocket assembly.

The cable chain efficiencies are not published by WM Berg but are likely high just as with roller chains. Even so, the drive motor is oversized as to assure there will be enough power on hand. WM Berg offers standard sprockets with as little as 13 up to 44 teeth, however any sprocket under 16 teeth is designated for idler use only. The 34 tooth driven sprocket located on the drive axle was the largest sprocket in stock at the time of purchase that would fit inside the sprocket cover. An 18 tooth sprocket was selected for the drive motor shaft and was the smallest sprocket in stock at the time of purchase. The gear ratio n is simply the ratio of the number of teeth on each sprocket:

$$n = \frac{drive\ sprocket\ teeth}{driven\ sprocket\ teeth} \tag{3.16}$$

$$n = \frac{34}{18} \approx 1.8\bar{8}$$

The torque required can then be calculated:

$$T_{motor} = \frac{Treq}{n} \tag{3.17}$$

Plugging in the torque requirement acquired from Equation (3.15):

$$T_{motor} = \frac{365.36\ oz - in}{1.8\bar{8}} \approx 193.5\ oz - in$$

The output torque needed of each drive motor is then 193.4 oz-in. An FOS of 3 is used to be sure that sufficient torque is available for proper operation. This puts the required torque output from each drive motor at three times the result from Equation (3.17), or 580.5 oz-in. Again, this is a very conservative

estimate which accounts for unknowns such as the tether weight, track and chain/sprocket assemblies, surface friction, and the actual skid steer power requirements on that surface.

A high end digital servo was selected for the drive motors. The MX-106T Dynamixel Robot Servo from Robotis was selected because of its incredible torque inside a lightweight package. This line of servos utilizes Maxon RE-MAX motors which are very powerful brushless permanent magnet DC motors. The MX-106T has an incredible 1189 oz-in holding torque at 12VDC. The Dynamixel robot servos maintain a small and lightweight form factor and yet accomplish a high output torque through a 225:1 internal metal gear reduction. The continuous running torque is not published by Robotis, however a good rule of thumb is to halve the holding torque. That means the MX-106T has a running torque of roughly 594 oz-in. This running torque meets the previously established requirement of 580.5 oz-in (with a FOS of 3). Figure 35 shows the MX-106T.

Figure 35 - Dynamixel MX-106T

The MX Dynamixel series of robot servos are equipped with an onboard 32bit 72Mhz Cortex M3 processor. The processor accepts feedback from a contactless magnetic encoder that provides position information of the output shaft location at a resolution of 0.088°. This closes the control loop and allows for PID control of output shaft position, speed, or torque. The controller also provides feedback on voltage and temperature. The MX series servos operate at a 12VDC nominal voltage and draw a maximum of 5.2 amps. Through the use of a TTL bus, the MX-106T can communicate with standard 5V digital logic at a rate up to 3 mbps. This means that multiple motors (up to 254), each configured with a

unique ID, can be daisy chained together on the same TTL communications bus. This very much simplifies things from a control aspect and allows for quick integration into robotic systems [35].

The MX-106 series servos are approximately 40.2mm x 65.1mm x 46mm and fit great inside the chassis. The Dynamixel servos come equipped with a servo horn and do not have an output shaft. An output shaft was machined with a mating surface with holes that align with the servo horn tapped holes. The output shaft is .25 inches in diameter and is shown mounted to the MX-106T servo in Figure 36.

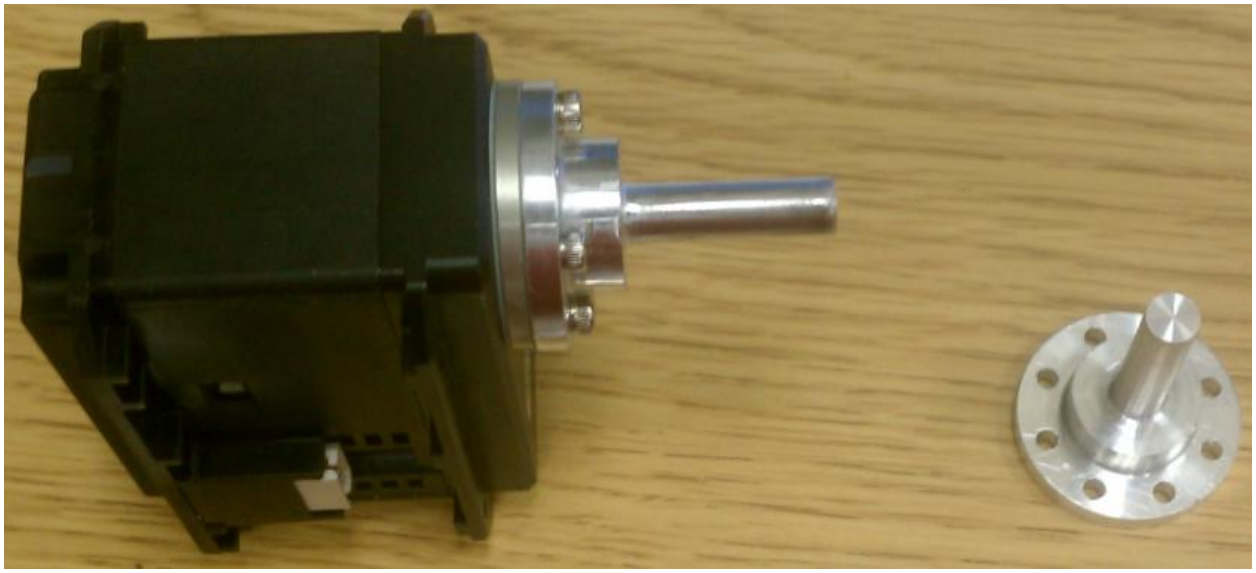

Figure 36 - Shown is the Dynamixel MX-106T with output shaft attached to the servo horn.

Another bracket was machined with CNC to provide extra support for the output shaft. This bracket has the same .25 inch bronze oil impregnated bearing press-fit into the bracket as used with the scissor lift members. When wear occurs, the bearing releases a film of oil to lubricate the shaft while still providing the lateral support to insure stable operation. This bracket mounts directly to the frame of the servo. Figure 37 shows the servo assembled with shaft and supporting bracket.

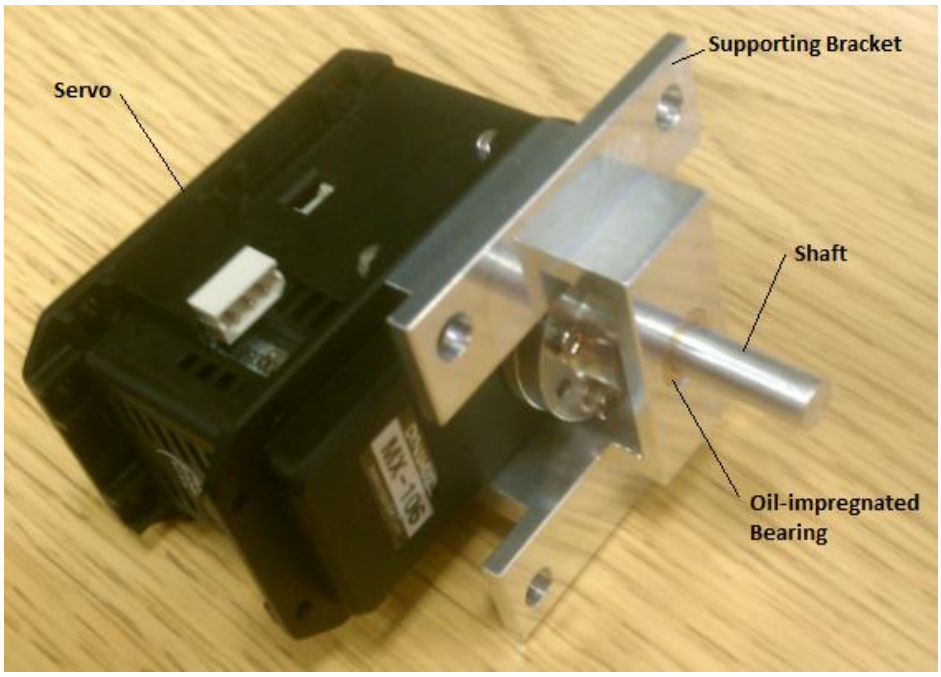

Figure 37 - Shown is the drive servo assembled with shaft and supporting bracket.

Finally, a second bracket is required to align and secure the motor inside the chassis. This bracket mounts to the chassis bottom plate. The supporting bracket (of which the servo mounts to) previously described has four holes for screws that mate with slots in the motor mount bracket. These slots allow for adjustment of the servo position which allows for the correct tension of the chain and sprocket assembly. Figure 38 below shows the motor mount bracket.

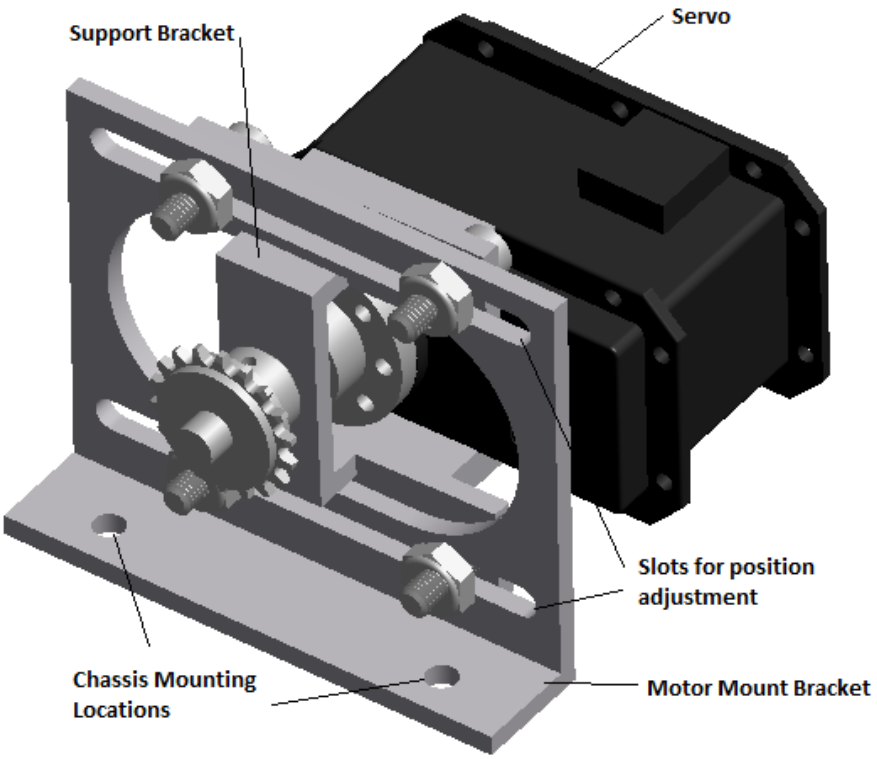

Figure 38 – Shown is the complete drive motor assembly.

In order to select the appropriate chain length from WM Berg, The center-to-center distance C must be known from the motor shaft to the drive axle where each sprocket is mounted. The chain length L can then be calculated,

$$L = 2C + 1.57(D + d) + \frac{(D - d)^2}{4C} \tag{3.18}$$

where D is the pitch diameter of the large sprocket and d is the pitch diameter of the small sprocket [34]. The center-to-center C distance is roughly 4 inches, D is 1.6061 inches, and d is .8503 inches. Using Equation (3.18) the length is:

$$L = 2(4in) + 1.57(1.6061\text{in} + .8503\text{in}) + \frac{(1.6061\text{in} - .8503\text{in})^2}{4(4in)} = 11.892\ in$$

WM Berg stocks chain lengths in 10 pitch length increments. The closest stock chain is 80 pitches, or 11.8 inches in length.

Lastly, the load on the chain must be determined for proper chain sizing within the Flex-E-Pitch series. The load on the chain can be calculated with by dividing the known torque at either sprocket with the pitch radius of the sprocket. Torque is simply the moment occurring about the axle (refer to Figure 39).

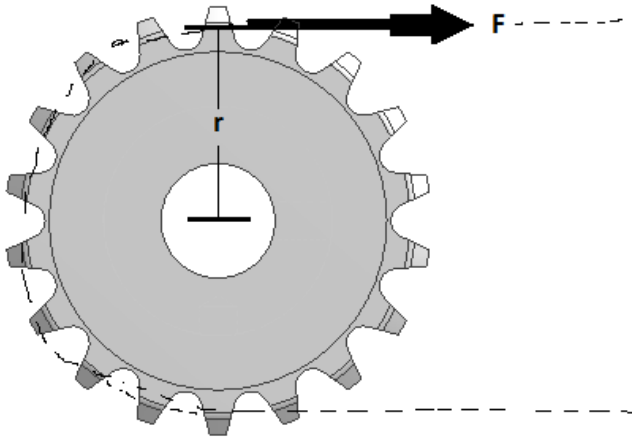

Figure 39 - Supporting diagram for chain load calculation.

Summing the moments about the axis of rotation yields the solution for the load acting on the chain,

$$F = T/r \tag{3.19}$$

Where F is chain load, T is torque at the sprocket, and r is the pitch radius of the sprocket. Using the maximum torque of the drive motor of 36.3lb-in (580.5 oz-in):

$$F = \frac{36.3lb - in}{(.8503\text{in}/2)} \approx 85.38\ lbf$$

The maximum load on the chain is just over 85 lbs. It is likely, however, that under normal operation conditions this load will be much lower. The Flex-E-Pitch series chain used is the smallest in its series with a .1475 inch circular pitch and an ultimate tensile load of 100 lbs.

3.3.3 Scissor Lift Motor and Powertrain

The maximum load of 30 lbs acting on the lead screw nut was previously determined in Section 3.2.3. The lead screw utilizes a bronze nut that that requires .576 oz-in of torque to raise approximately 1 lb [34]. This means that to in order to raise a load of 30 lbs a total of 17.28 oz-in of torque is required. As mentioned earlier, the motor is positioned next to the lead screw rather than in line with the axis of rotation. This saves length by allowing for a shortened chassis.

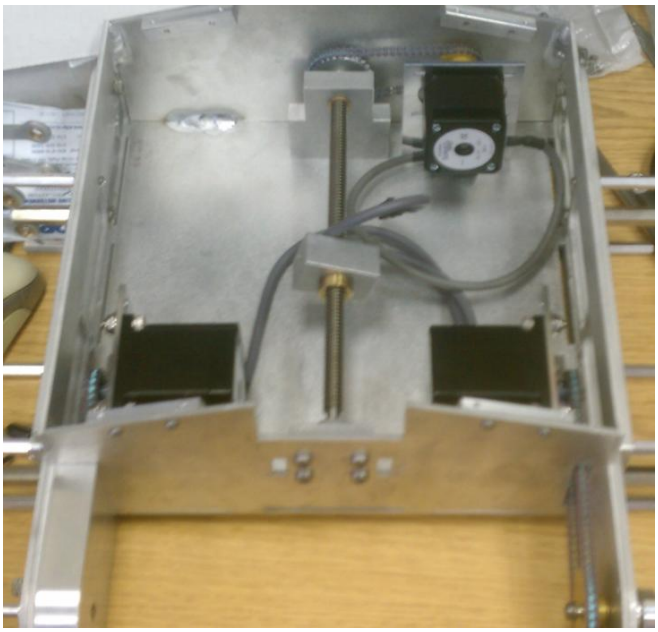

Figure 40 - Scissor lift powertrain assembly.

The same Flex-E-Pitch series of chain and sprockets from WM Berg as used with the drive motors were used to transmit power from the motor to the lead screw. As with the powertrain for the drive motors, this provides an opportunity to multiply the torque output from the motor. Based on availability and size constraints, a 20 tooth sprocket was chosen for the motor drive shaft and a 29 tooth sprocket for the lead screw shaft. Using Equation (3.16), the gear ratio is:

$$n = \frac{29}{20} = 1.45$$

The torque output required from the scissor lift motor is then calculated with Equation (3.17):

$$T_{motor} = \frac{11.28\ oz - in}{1.45} \approx 7.78\ oz - in$$

A bipolar NEMA 17 stepper motor was selected from the SureStep line of stepper motors. This is the smallest frame size in the series. A stepper motor was chosen because it is very easy to track position by simply counting steps. The STP-MTR-17040 motor is a single stack NEMA 17 motor that provides a maximum holding torque of 61.4 oz-in. As before the holding torque is halved which provides a very conservative estimate of 30.7 oz-in of running torque. With this running torque, an FOS of almost 4 is achieved. The stepper motor is paired with a G203V Gecko Drive digital step drive. This drive was selected because it accepts a 5VDC pulse and will increment the stepper motor one step for each pulse.

A digital input of 5V selects the direction. The G203V accepts 18 to 80VDC input and has short-circuit protection on motor outputs, reverse polarity protection for input power, and over/under voltage protection with an internal fuse. The G203V is shown in Figure 41.

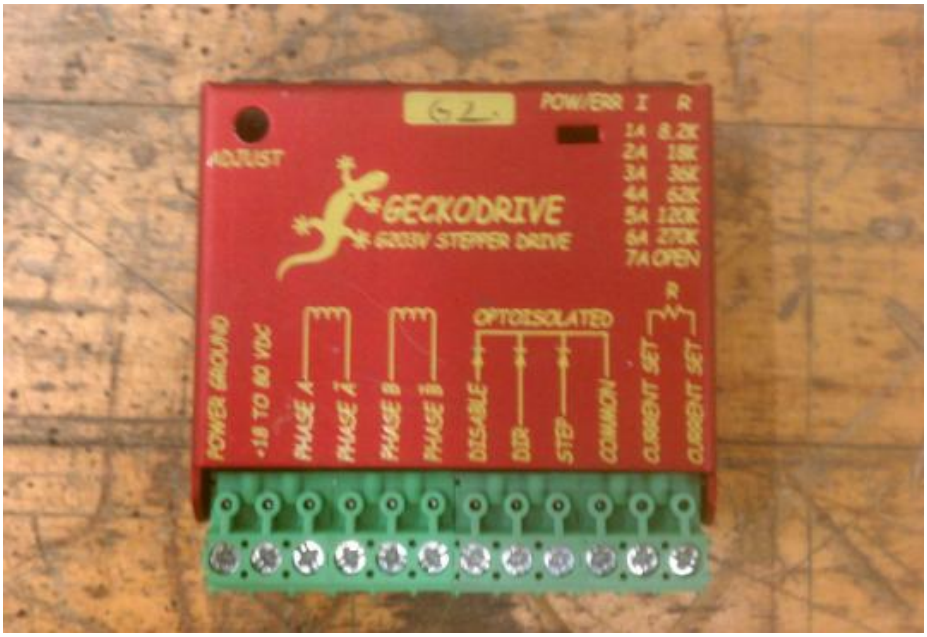

Figure 41 - Geckodrive G203V Stepper Motor Drive.

The lead screw requires 12 turns to move the lead screw nut 1 inch and with a gear ratio of 1.45 the motor must rotate 17.4 times to accomplish the same distance. The STP-MTR-17040 stepper motor has 200 steps per revolution which means 17.4 revolutions requires 3400 steps. The relationship between step size and lead screw nut travel can be found by the following formula,

$$s = \ x * 12steps/in * n * 200steps/in \tag{3.20}$$

where s is step size, x is lead screw nut travel distance, and n is the gear ratio. Equation (3.20) is needed by the controller in order to control position of the scissor lift.

As with the drive motors, a bracket is required to align and secure the scissor lift motor inside the chassis. The same style bracket as with the drive motors is used to accomplish this by mounting to the bottom plate of the chassis. Refer to Figure 42:

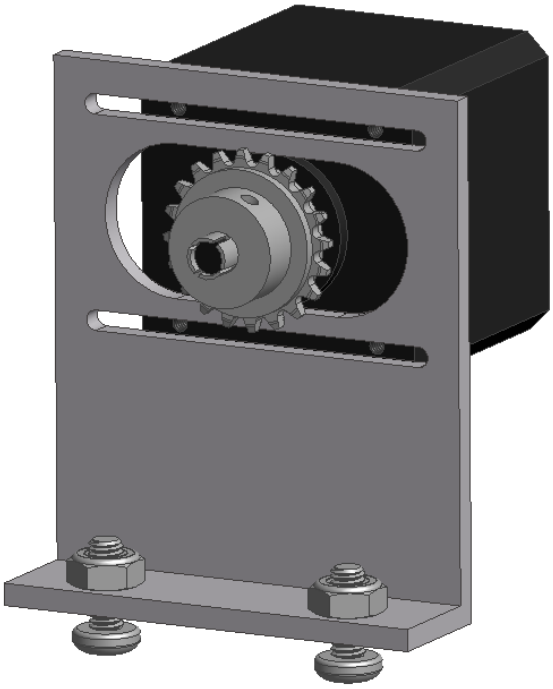

Figure 42 - Scissor lift motor mount assembly.

The scissor lift motor mount bracket has slots which fit the screws that thread into the NEMA 17 motor chassis. These slots allow for adjustment of the stepper motor position and allow for the correct tension of the chain and sprocket assembly.

A magnetic reed switch paired with a magnet was utilized to prevent locking of the lead screw and powertrain as well as provide a method of payload height calibration. The reed switch is much like those used for security systems on windows or doors. Figure 43 shows the configuration of the reed switch and magnet on the scissor lift assembly:

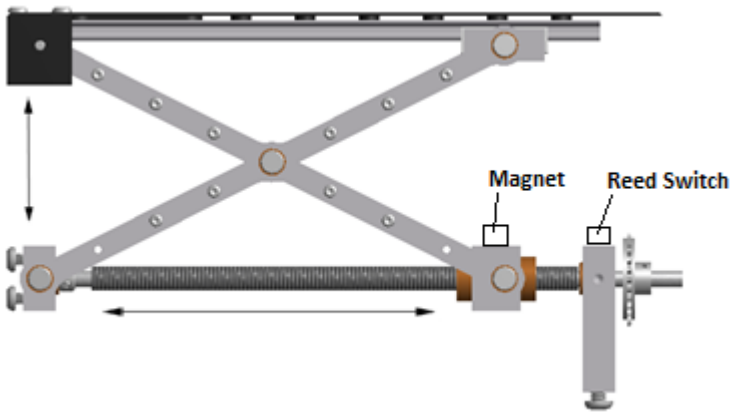

Figure 43 - Lead screw reed switch configuration.

The reed switch itself has one electrical input and one output and continuity is determined based on the proximity of an external magnet. The magnetic field of the magnet increases as the magnet approaches the reed switch until it reaches a threshold causing the switch to latch. The input and output are then connected. When the magnetic field is removed, the switch is released. This allows an onboard controller to calibrate the position of the lead screw nut upon power up of the inspection tool because the latching point and release point of the reed switch is relatively constant. To accomplish this, a 5V signal can be applied to the switch's input and the output can be connected to the digital input on a controller. At system startup the scissor lift motor can raise or lower the scissor lift until it reaches the reed switch latch or release point. Once it reaches either of these points, the position of the scissor lift is then known and the controller can count motor steps to achieve a specific scissor lift position.

3.3.4 Payload Gimbal

A pan and tilt gimbal was created using two Dynamixel MX-28T servo actuators. These are the same series of actuators that are used for the drive motors except smaller. They provide 354 oz-in of holding torque after 1/193 gear reduction from the motor. With no information published on the running torque, halving the holding torque provides a good approximation. As with the MX-106 actuator, the MX-28T contains the same 32bit 72Mhz Cortex M3 microprocessor that accepts feedback from a contactless magnetic encoder for position of the output shaft. This allows for PID control of position and velocity. Control over torque is available as well. The 5V TTL bus allows for the gimbal actuators to communicate on the same bus as the drive motors. This helps to simplify onboard communications and control with the onboard controller. The mounting configuration is shown in Figure 44.

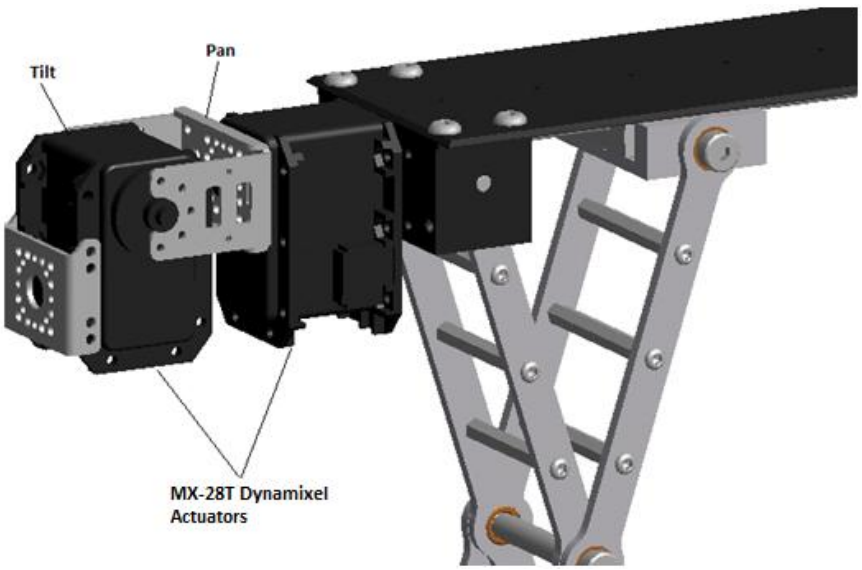

Figure 44 - Shown is the pan/tilt payload gimbal.

The actuator used for panning (rotation) of the payload is attached directly to the payload mount on the scissor lift with the servo horn facing in the forward direction. This configuration provides rotation about the lateral-vertical plane. The tilt actuator has a bracket supplied by Robotis with one end that mounts to the servo horn and the other supported by a bearing on the rear side of the actuator. The center of this bracket is then attached to the servo horn of the panning actuator. Figure 45 demonstrates the gimbal equipped with a payload:

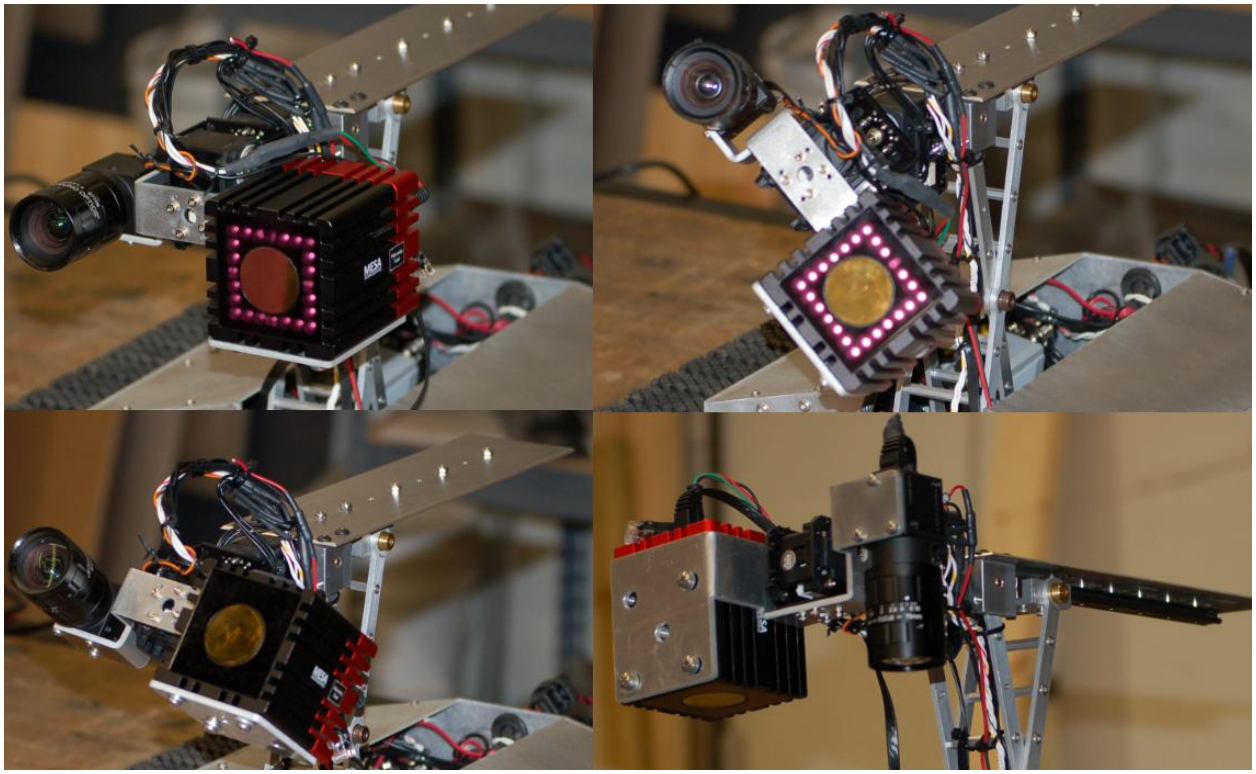

Figure 45 - Shown is the gimbal actuators equipped with a payload.

3.4 Electrical Design

The focus of this section is on the electrical design and component selection. This includes the electronics for drive cameras, onboard controller, and communications. The power conversion and distribution is discussed as well.

3.4.1 Drive Cameras

Two EverFocus EM-500 series cameras were selected to serve as forward and rear facing drive cameras. The EM-500 series camera contains a 1/3 inch Sony ICX638 CCD sensor and has a low light sensitivity of 0.2 lux. The camera outputs a high resolution 75 Ohm 1Vp-p analog video feed of 550 tv lines. This is all packaged in a 1 inch by 1 inch metal case. These cameras were primarily chosen because of their excellent form factor.

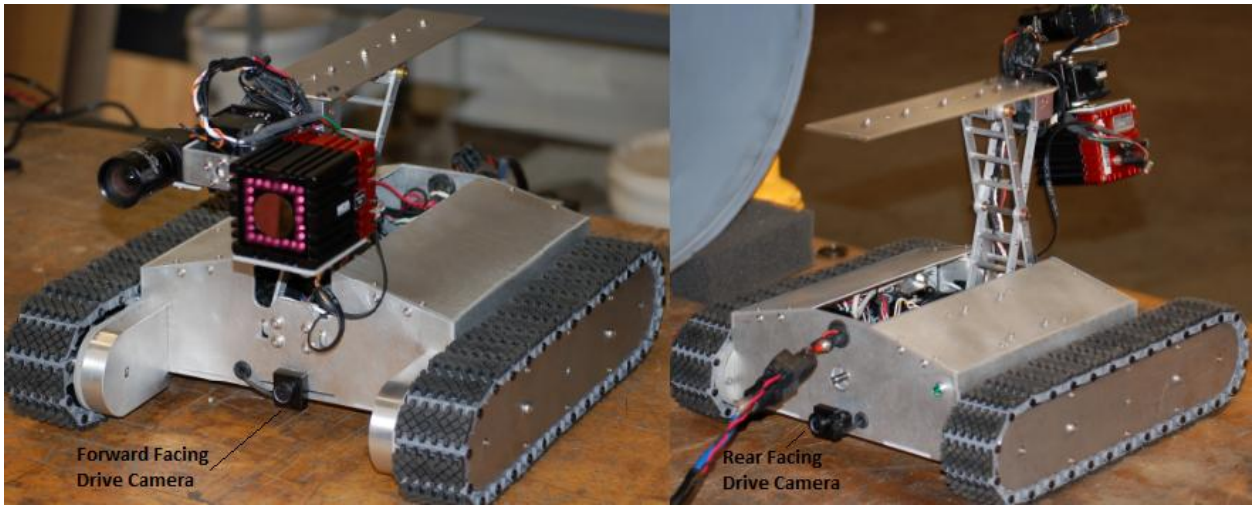

Figure 46 - Shown is the inspection tool equipped with drive cameras.

There are two analog video feeds from the drive cameras described above that require a composite video cable for transmission. The analog feeds are required to be digitized so they can be viewed on the host controller. To reduce overall tether diameter, a video encoder was needed for transmission of the analog video signals. An AXIS M7001 video encoder was selected primarily because of its great form factor and ease of use. The encoder, shown in Figure 47**,** was attached at the back end of the tether inside the inspection tool chassis. H.264 video compression format is supported, which drastically reduces bandwidth and storage requirements. The AXIS M7001 can also stream in Motion JPEG. A maximum resolution of 720x480 NTSC is available at 30 frames per second which is sufficient for the drive cameras. The M7001 also has an rs-422/rs-485 communications port which adds flexibility to the inspection tool incase future peripheral electronics or sensors are added that may require that form of communication.

Figure 47 - Displayed is the AXIS video encoder used to encode the drive camera video feeds.

The M7001 is powered over Ethernet (PoE) and accepts power over the same Ethernet cable as used for data transmission. In other words, data and power transmission are performed simultaneously along the same wires. A PoE injector from GE Security was selected to supply power to the AXIS unit because the unit accepts a 48VDC input.

The AXIS M7001 accepts only one video feed. A Teledyne Video Relay was selected to switch the video feed from one drive camera to the other, effectively preventing the need for an extra encoder. Incorporating a single video encoder removes the need to run composite video cables along the tether that would be required to access the drive camera video feeds. The Teledyne relay matches the 75 ohm impedance of the analog video feed from the drive cameras. Impedance matching is required as to minimize signal loss and prevent video feed degradation. The circuit required for operation is shown below in Figure 48.

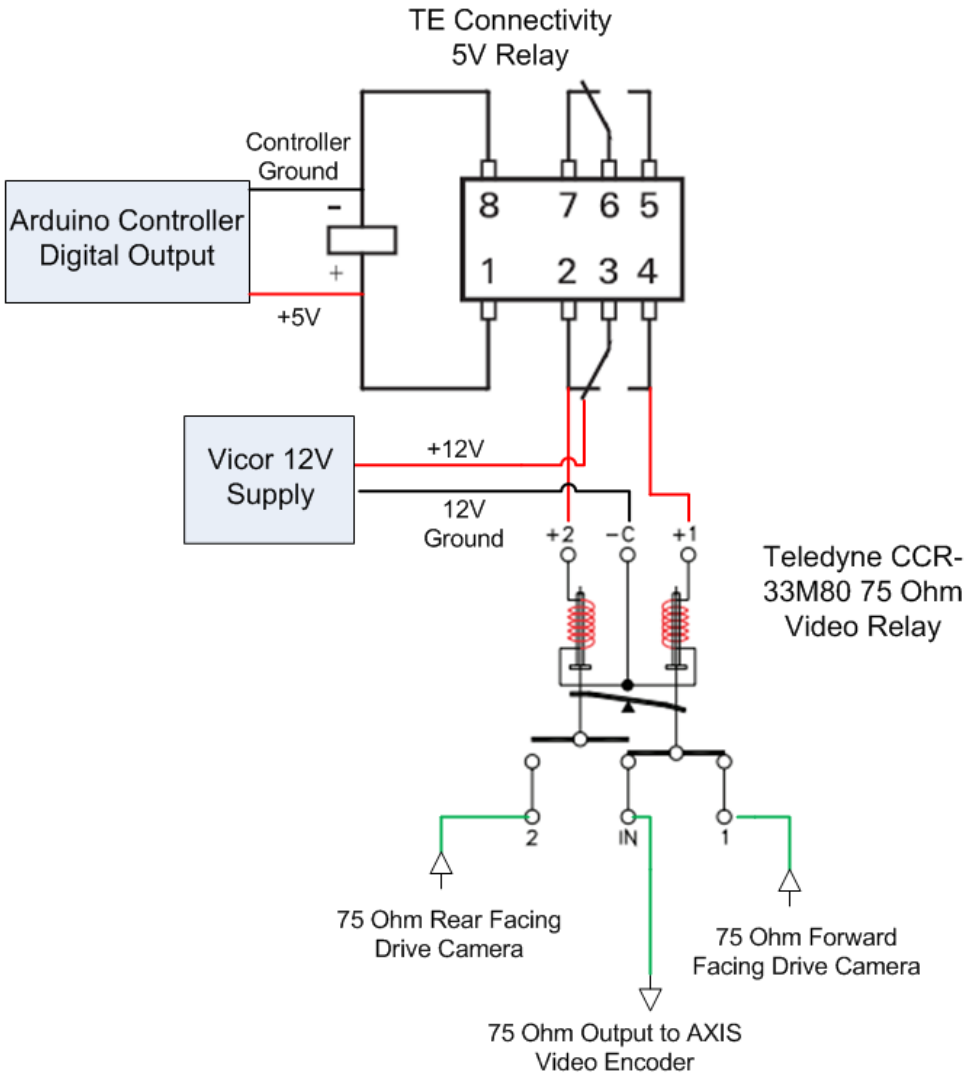

Figure 48 - Displayed is the video relay circuit for the drive cameras.

The Teledyne relay has three control pins on the top of the relay. If 12V is supplied to Pin 1, then the forward facing drive camera video feed is connected with the AXIS unit. If 12V is supplied to Pin 2, the rear facing drive camera is connected with the AXIS unit. The third pin is for ground.

3.4.2 Controller

The Arduino Mega 2560 was chosen for the onboard controller inside the inspection tool. This controller, shown in Figure 49 is an off-the-shelf solution for the rapid development of the embedded control system located inside the inspection tool. Arduino was a project that was originally developed at the Interaction Design Institute Ivrea in 2005 [36]. Arduino controllers have been developed as open-source hardware, which is very similar to open-source software in that all of the original design files are

available to the public for free. This means that there is a giant user base supporting and contributing to these platforms, and this user base is growing indefinitely. The Arduino open-source physical computing platforms were originally developed as an interface for interactive objects and peripherals. Arduino projects commonly involve a variety of switches, sensors, motors, lights, etc. Arduino hardware also works well as an interface for communications with software running at other locations. This is advantageous for the inspection tool where there is a need for an interface for the primary controller, or computer located at the front end of the tether. Arduinos utilize a programmable microprocessor that contains a variety of both analog and digital input/output pins as well as communication lines such as SPI, I^2C, and serial. Most Arduino platforms utilize Atmel's ATMEGA8, ATMEGA168, and ATMEGA2560 as the workhorses for computing.

The Arduino development environment is free open-source software that connects to the Arduino hardware to upload programs as well as communicate with them. The development environment is similar to that of others and includes a code text editor, message area, text console and toolbars with common functions, all of which are all packaged within. Software written with the development environment is called "sketches". Sketches consist of the code that is written in the text editor. When sketches are executed, relevant messages or errors are displayed in the message area and text console. Sketches are uploaded via USB connection with the Arduino hardware after verifying the code for errors. The sketch is then compiled and sent to an onboard bootloader that flashes the microcontroller with the new code. Open-source libraries are available for use in sketches and provide extra functionality for manipulating data or working with hardware. Standard libraries exist for vast variety of functionalities: reading and writing to permanent storage, Ethernet communication, serial communication, controlling LCDs, controlling motors, SPI communications, keyboards, mice, game controllers, XBee, Bluetooth, sensing, timing, etc. Many other third-party libraries exist as well that provide further functionalities [37].

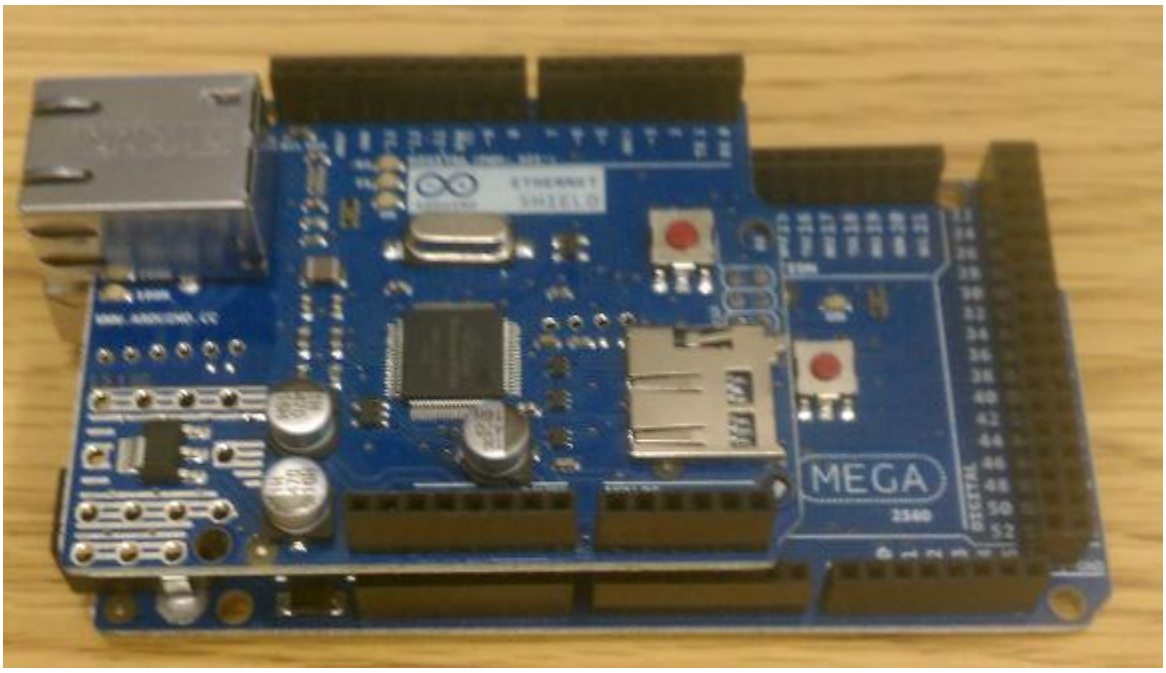

Figure 49 - Arduino Mega 2560 with Ethernet shield.

The Arduino Mega 2560 utilized the ATMEGA25600 as the onboard microprocessor which is paired with a 16 MHz crystal oscillator. There are a total of 54 digital pins with input/output capability. The digital pins are used to detect the scissor lift limit switch, communicate via TTL with the Dynamixel digital servos (used for drive motors and pan/tilt actuators for the payload gimbal), send the step/direction commands to the stepper motor drivers, and control the drive camera feed via Teledyne video relay. The Mega 2560 also contains 16 analog inputs, 4 UART serial ports, and dual power inputs and 256 KB of flash memory. Power can be supplied through a dedicated barrel jack or supplied through USB. Six external timers are available that can be used to control timing for things like the step command to the scissor lift motor driver (which controls the speed of the stepper motor). There are also four 8-bit PWM outputs that can be used to control things such as lighting, or DC motor controllers [38].

In order to communicate with the Arduino controller, an Ethernet module is required. Figure 49 shows the Arduino Mega 2560 paired with the Arduino Ethernet Shield. The Ethernet shield simply plugs into the Mega with long wire-wrap headers that extend through the shield and provides an RJ45 interface for communications. The Ethernet shield is based on the Wiznet W5100 Ethernet chip which provides a network stack capable of TCP and UDP. A connection speed of 10/100Mb/sec is available. As mentioned, an Ethernet library is available through the open-source software development environment that allows for quick implementation of the communications protocol.

3.4.3 Communications

The communications for the inspection tool is set up such that a host controller, or PC, can simply connect and have complete control of the inspection tool via a single connection point. This connection point is at the front end of the system. Onboard the inspection tool is a Gigabit switch that provides connectivity to all peripherals. Refer to Figure 50.

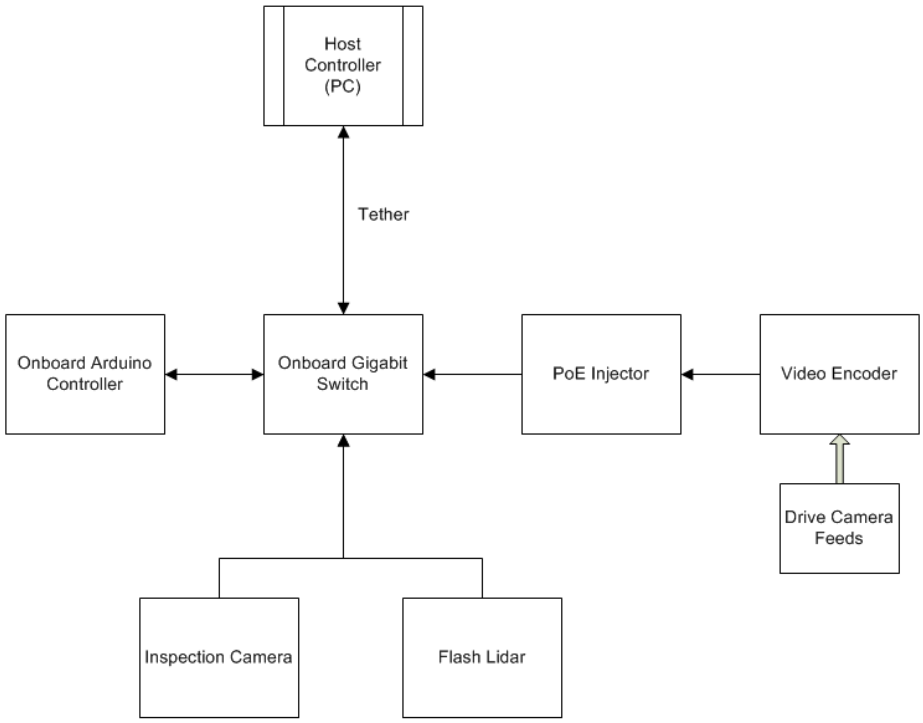

Figure 50 - Flow diagram of the communications network on the inspection tool.

A NETGEAR GS108 Gigabit Ethernet switch was selected because of its 10/100/1000 Mbps autosensing ports. There are a total of eight ports that allow for simple connectivity of devices on the network. These devices include the onboard Arduino controller which has the capability to parse the data coming from the host controller and perform a given task, such as raise the scissor lift, communicate with the drive motors, or switch the drive motor video feed. The switch connects to the PoE module which simultaneously communicates with and powers the AXIS video encoder. This allows the host controller to acquire the analog video feed from the drive cameras in digital form. The inspection tool is currently equipped with a Point Grey Flea3 gigabit Ethernet inspection camera as well as a MESA Imaging SR4000 Flash LIDAR that sends depth data in the form of point clouds over gigabit Ethernet. All of the data is

routed through the NETGEAR switch and supplied to the host controller via a single connection point. The switch is mounted inside the chassis below the scissor lift and lead screw assembly as shown below in Figure 51:

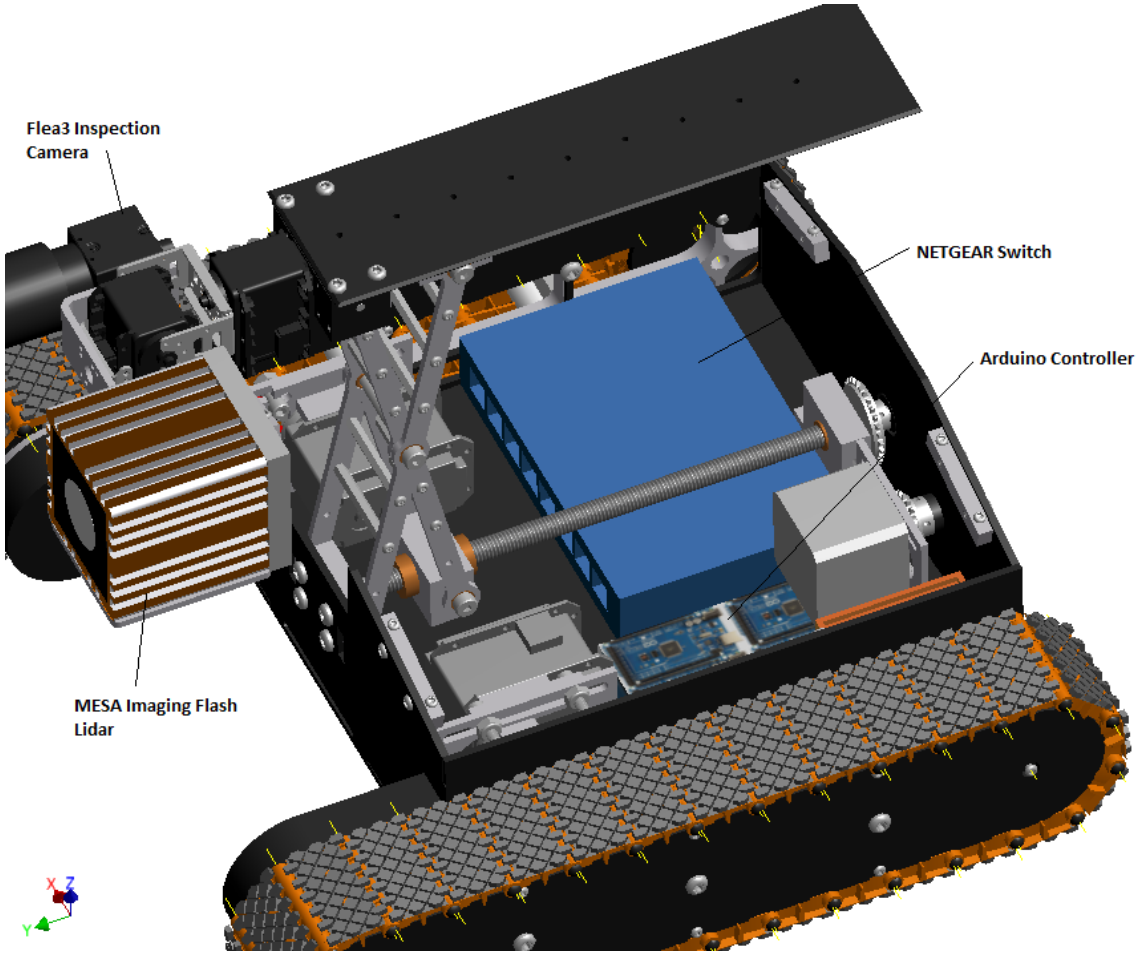

Figure 51 - Network switch mounting location.

3.4.4 Power Distribution

The inspection tool is configured with a wide variety of electronic devices and peripherals. These devices have different power needs and require a power distribution configuration that supports those needs. Figure 52 displays the power distribution configuration of the inspection tool.

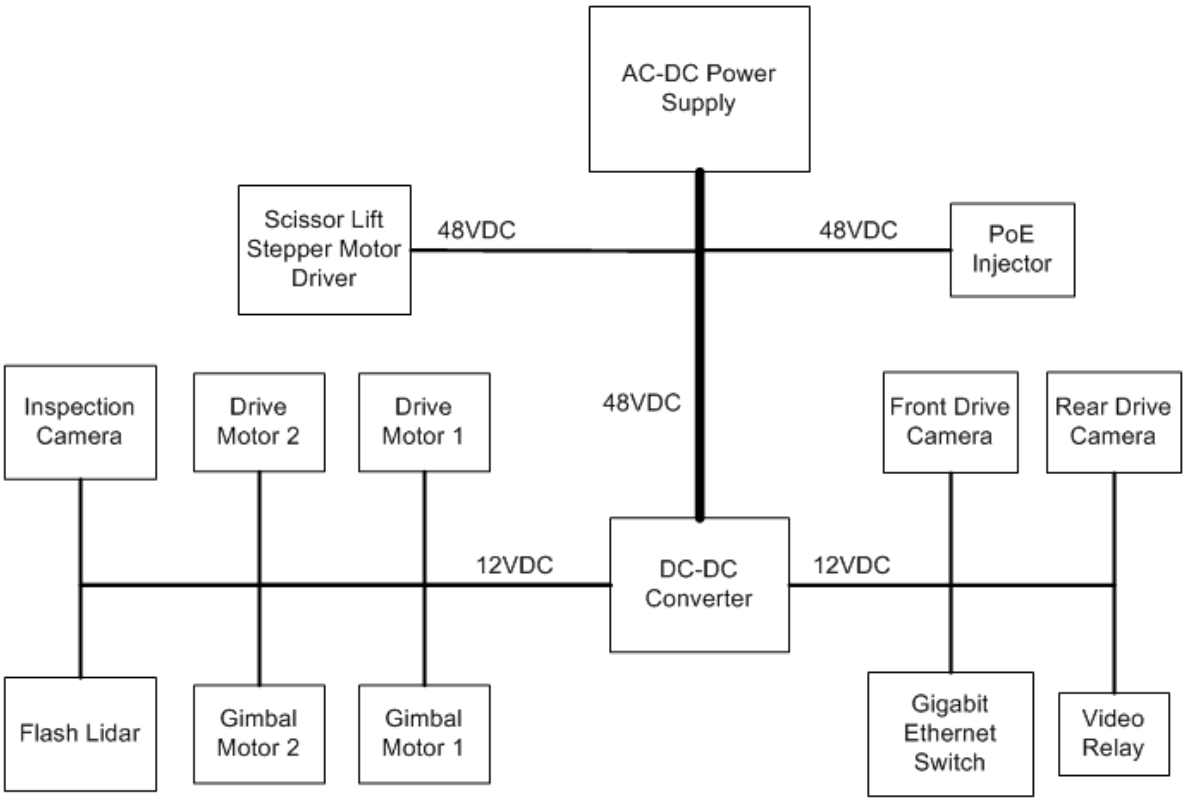

Figure 52 - Power distribution configuration for the inspection tool.

The inspection tool is designed as a tethered platform where power is supplied at the front end of the system and delivered along the tether to the inspection tool. An AC-DC power supply is required that accepts a facility source of AC power and converts it to DC power as to supply the onboard electronics of the inspection tool. First, the overall power requirements must be known. The following fundamental relationships must be understood when developing power requirements for a system [39],

$$V = I * R \tag{3.21}$$

where V is voltage, I is current, and R is resistance. Equation (3.21) is essential because current draw can be for devices, or a cable for example, with a known resistance and an applied voltage. Once the current and voltage is known, the power draw (P) can be found by the following equation:

$$P = V * I \tag{3.22}$$

Power, which is the rate of which energy is consumed, is simply the voltage supplied at the device multiplied by the current draw of the device. Most devices clearly specify an operating voltage or range

and a maximum current draw. Many devices explicitly state the power consumption as well. Table 1 summarizes the power requirements of the 12VDC electronics in the inspection tool:

Table 1 – Power requirements for 12VDC electronics within inspection tool.

	Quantity	Voltage	Max Current per device (A)	Max Power per device (W)	Total Power	Total Current	
GigE Switch (8 Port)	1	12	1	12	12	1	
Flea3 Inspection Camera	1	12	0.21	2.52	2.52	0.21	
Arduino	1	12	1	12	12	1	
Flash LIDAR	1	12	1	12	12	1	
Video Relay	1	12	0.2	2.4	2.4	0.2	
Drive Cameras	2	12	0.3	3.6	7.2	0.6	
Dynamixel MX-28T Servo	2	12	1.4	16.8	33.6	2.8	
Dynamixel MX-106T Servo	2	12	5.2	62.4	124.8	10.4	
					12V Current (amps):	17.21	
					12V Power (watts):	237.50	**this includes .85 efficiency for DC-DC conversion*

Based on the maximum current draw of 17.21 amps from the 12VDC circuit, there was a need to reduce the current along the tether. Equation (3.21) shows that voltage is proportional with current and resistance. If the resistance stays constant and the voltage is raised, the current is effectively reduced. With less current, larger gauge power cables may be used along the tether which will reduce tether weight and overall diameter. A 48VDC supply would drop a 12VDC current down by a factor of four. A DC-DC converter is then required to perform this conversion. A Vicor V48B12E250BL DC-DC converter module was selected that accepts a 48V input and provides a 12V output. This module is shown mounted on the inner side wall of the chassis in Figure 53 below:

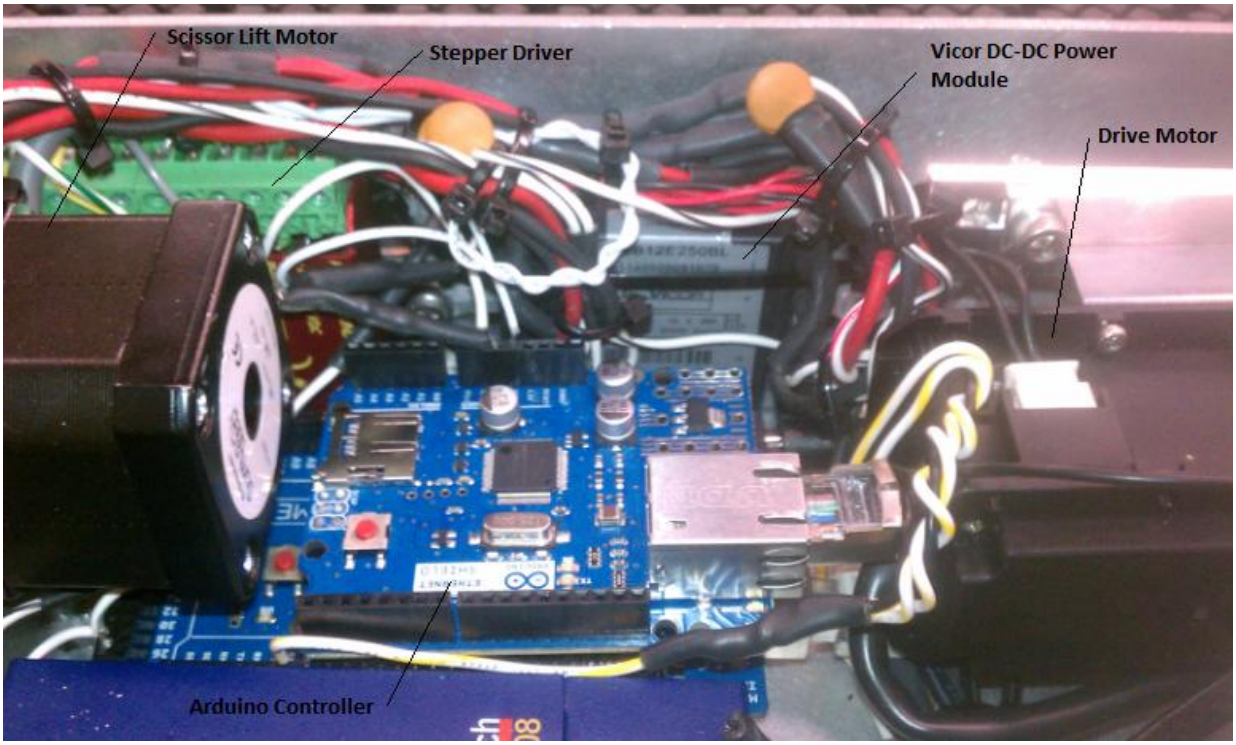

Figure 53 - Mounting configuration of Vicor DC-DC converter.

The V48B12E250BL DC-DC converter module is part of the Vicor Mini Family and has advanced power processing with high frequency switching. This module has an output of 250 Watts after conversion. The 237.5 Watt power consumption shown in Table 1 from the 12VDC circuit includes an efficiency of 85%. This is because there is a 15% power loss when converting from 48V to 12V on this particular module. The actual power drawn from the converter (on the 12V side) is 85% of that listed or about 202 watts. That leaves just under 50W of available power on the 12V circuit for other peripheral devices or sensors that may be added at a later time. If more power is required, multiple Vicor converter modules may be connected in parallel. As long as the input, output voltage, and power level is the same on each module, a parallel bus can be run to the PR pin on each module. Each module will then effectively current share the same portion of the load.

As was mentioned earlier, a power supply is required that accepts AC power and converts it to 48VDC power. The requirements must first be known for the 48V circuit before the appropriate power supply is selected. The 48V power consumption is reviewed below in Table 2:

Table 2 - Power consumption of the 48VDC circuit.

DC-DC 12V Circuit (from above)	1	48	4.95	237.50		4.95
PoE Injector (includes video encoder)	1	48	0.38	18.24		0.38
Scissor Lift Motor	1	48	2.3	110.4		2.3
					48V Tether Current (amps):	7.63
					48V Power (watts):	366.14

Aside from the DC-DC converter load that was just described, there are two other devices that draw power on the 48V circuit. First is the PoE injector that supplies power to the video encoder. The other is the scissor lift motor driver. The total power draw from these devices and the converter module is 366.14 watts. Using Equation (3.21), the current draw at 48V is 7.63 amps.

The RSP-1000-48 Mean Well single output power supply was chosen as the front end AC-DC power supply. This unit is capable of supplying 1000W of power at up to 21 amps. The unit has an efficiency of 90% and has a built in 5V/.5A auxiliary power output. The unit draws up to 12A at 115VAC and has overload, over voltage, and over temperature protection. As with the Vicor DC-DC converter, the voltage output has a trimming adjustment. The output voltage of the Mean Well supply can be trimmed from 40% to 110% of the rated output. With a 1000W available output and only 366.14W of power draw, this power supply provides over 633W of extra power for the addition of other motors, electrical devices, or sensors. The Mean Well power supply also has a built-in remote on-off control. This control is wired to a safety e-stop button where power can be cut immediately when necessary. Figure 54 shows the Mean Well power supply:

Figure 54 - AC-DC 48V Mean Well power supply.

3.5 Inspection Test Environment

A test environment was set up that consists of two 55-gallon drums attached in series. The setup is roughly 23 inches in diameter and 70 inches in length. The test environment contains various dings, dents, and other imperfections. The drums are supported with foam pads that hold them in place while still allowing for disassembly. Lighting is supplied with an external 0.5 Watt LED that runs at 28V and provides ambient light for inspection. The LED is hung at the entrance of the test environment and a separate power supply is used for power. Figure 55 shows the test environment.

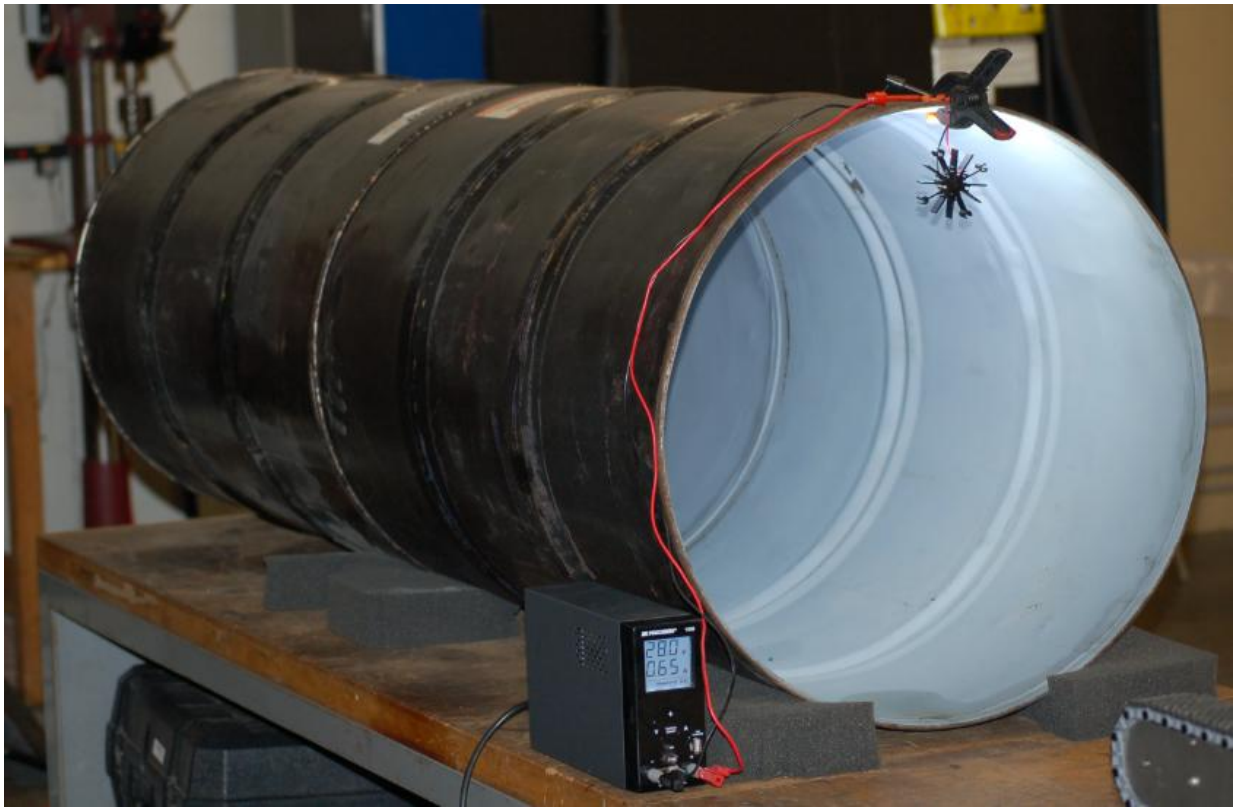

Figure 55 - Inspection tool test environment.

Chapter 4: Results

This chapter demonstrates the successful inspection of the test environment described in Section 3.5. A vibrational analysis was performed as to characterize the vibration loads seen by the instrumentation package. The analysis was performed on the scissor lift and the vibration levels and frequencies that were excited from forward movement are displayed in a power spectrum. Characterization of the inspection tool is described and the performance is outlined.

4.1 Simulated Environment Inspection

The inspection tool successfully transported an instrumentation package consisting of LIDAR and an inspection camera for inspection of the 55-gal drum test environment. Figure 56 shows the operator performing a non-destructive visual inspection with the inspection tool.

Figure 56 - Operator successfully inspects the test environment.

The scissor lift worked exceptionally well, allowing for instrumentation package positioning in order to maintain the most appropriate birds-eye-view. Figure 57 and Figure 58 demonstrate the inspection tool's capability of conducting a radial inspection of the drums.

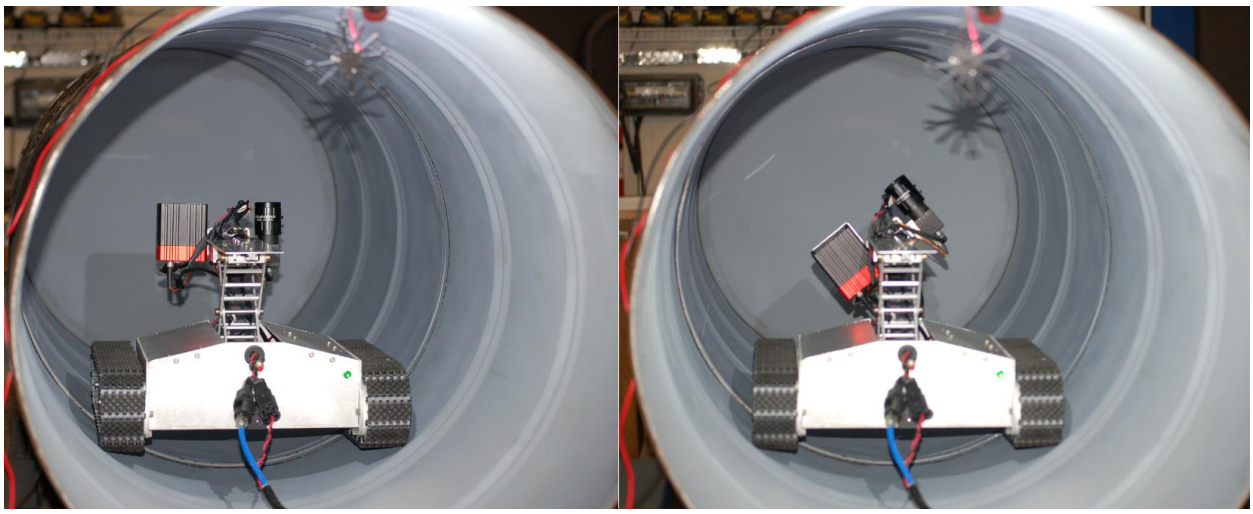

Figure 57 - Inspection tool is conducting a radial drum inspection.

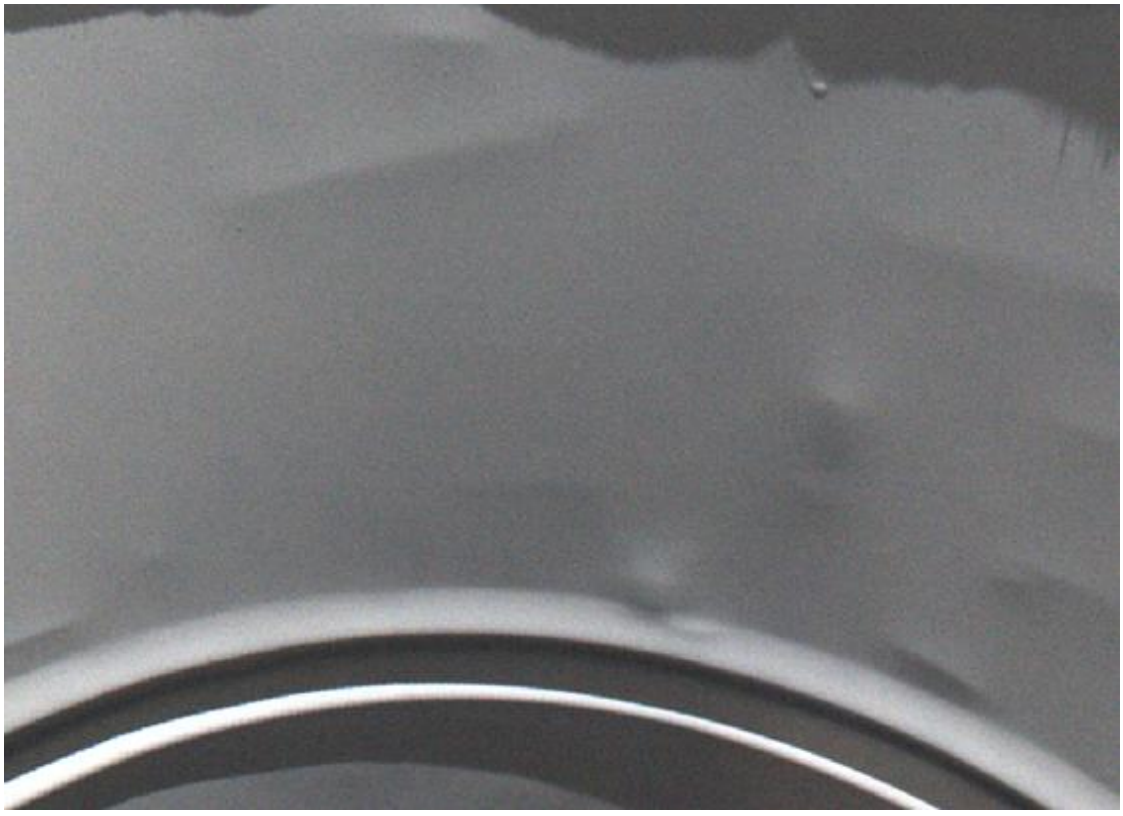

Figure 58 – Shown is a sample of the photographic documentation collected from inspection of the test environment.

4.2 Vibration Analysis

A simple vibration analysis was performed on the scissor lift in order to characterize the vibrational loads that the instrumentation package may experience. To accomplish this task, a MMA7331L 3-axis accelerometer produced by Freescale Semiconductor was selected because it was available on hand. This device operates as a fully calibrated linear accelerometer as long as the power supply is within the range of 2.2 to 3.6V and supplies a separate analog output signal for each axis. The range selected was ±4g and the typical sensitivity of the MMA7331L is 308mV/G. To acquire these signals, a National Instruments USB-6008 data acquisition device was used to interface with the accelerometer. The USB-6008 has both analog input and analog output channels which make for easy connection. The device was configured to supply 3.3V to the accelerometer while collecting the three analog signals. Figure 59 below shows the setup on the inspection tool:

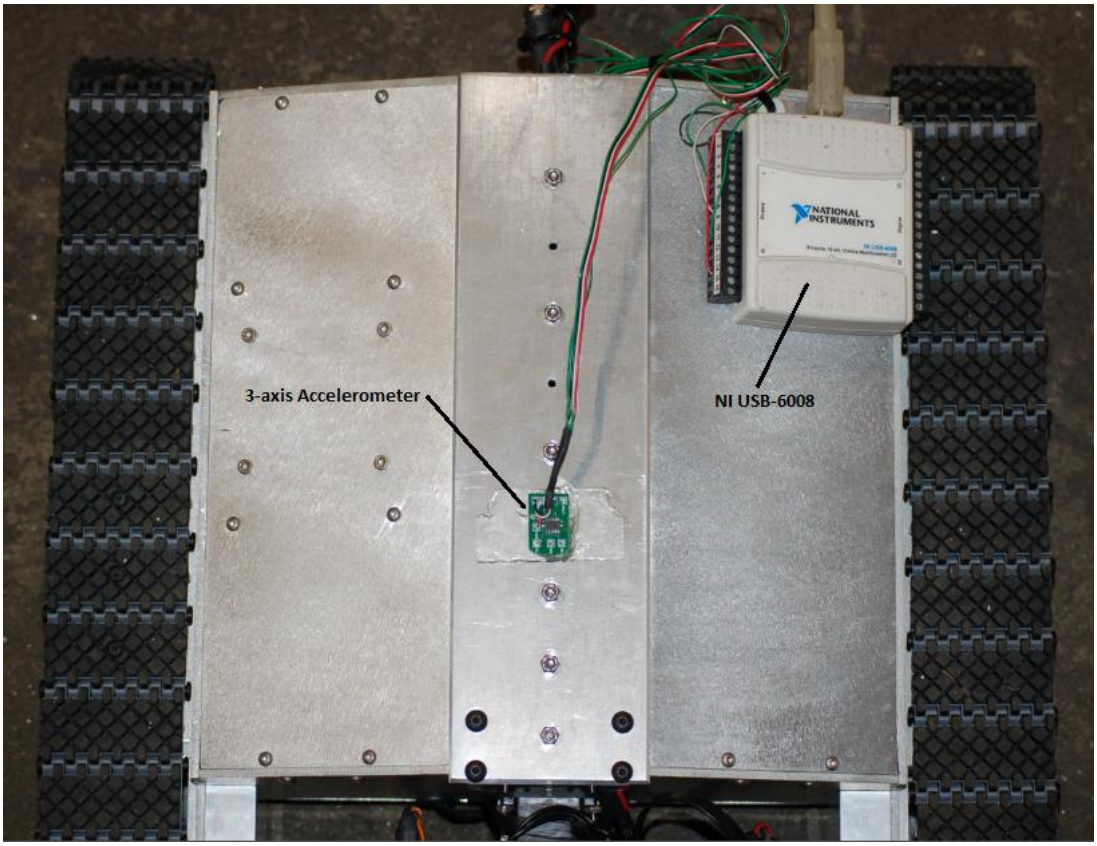

Figure 59 - Shown is the inspection tool equipped with electronics for vibration analysis.

The accelerometer was attached to the top of the scissor lift using removable adhesive strips. Multiple experiments were performed. Data was collected with the system powered completely off and with the system powered on but stationary. Data was collected with the chassis suspended on rigid foam blocks while the tracks rotated freely at full operational speed. Data was also collected while the inspection tool traveled at full speed with the scissor lift at full, middle, and lowered heights. The accelerometer data was sampled at 100 Hz and data was recorded for 25 to 30 seconds for each experiment. With a 100 Hz sampling rate, a Nyquist frequency of 50 Hz was achieved. Spectral density estimation was performed using Welch's method to process the data. Each sample record was broken into 8 segmented sections of equal length, each with 50% overlap. Each segment was windowed with a Hamming window of equivalent segment length. A periodogram was then calculated using a fast Fourier transform (FFT) for each segment. The individual periodograms for each segment are then averaged to provide the Power Spectral Density (PSD) for the entire sample record. The PSDs for the previous said experiments are attached in Appendix III – Scissor Lift Vibration Analysis. The excitation from the treads while suspended at full operational speed transmits little energy up through the scissor lift. However, the scissor lift was excited in the longitudinal direction at all scissor lift heights while driving at full speed. Figure 60 shows the PSD for each trial.

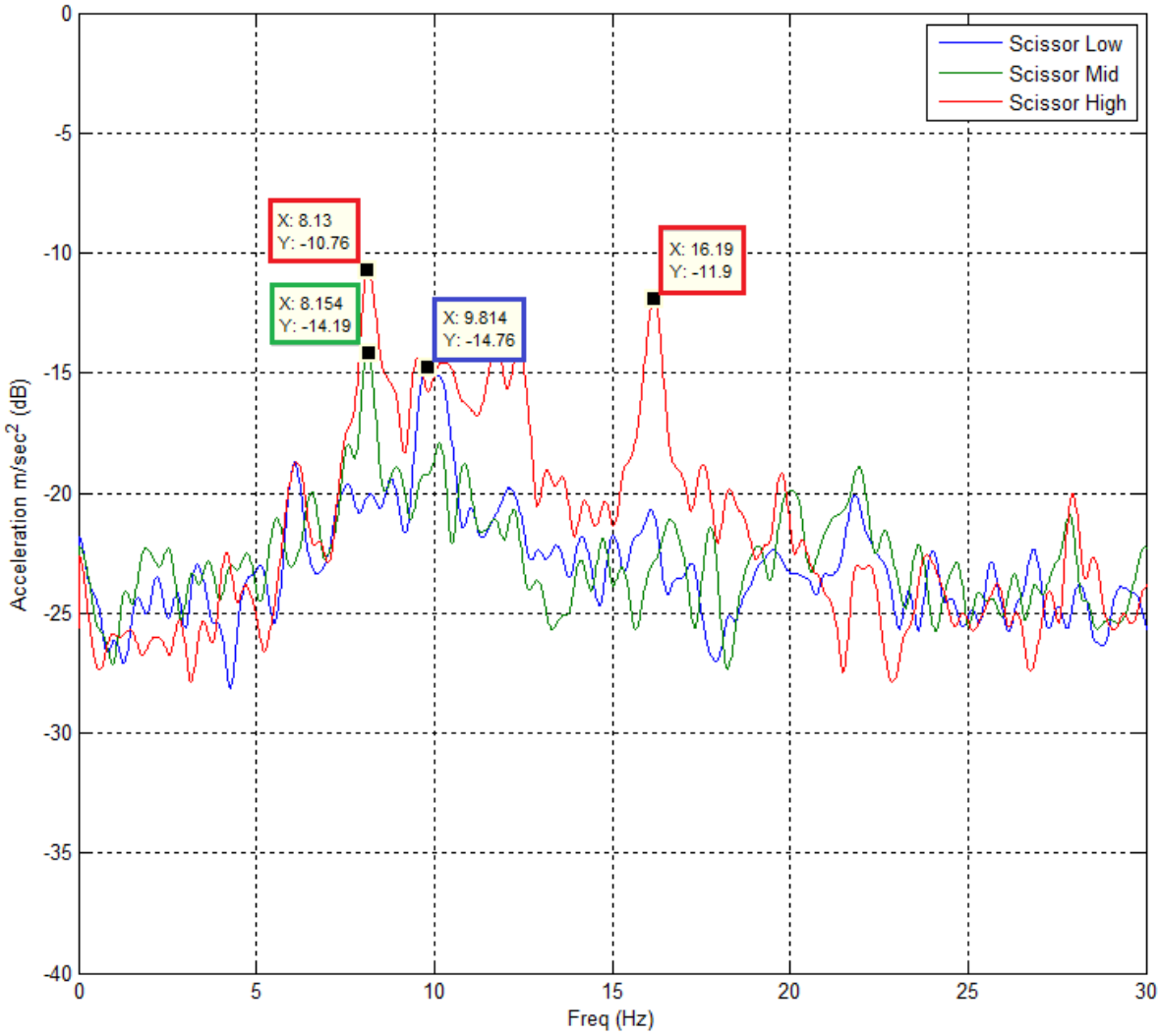

Figure 60 – Vibrational analysis of scissor lift while driving.

The PSD demonstrates that the excitation from the tracks or powertrain is resulting in higher energy levels between 5 and 20 Hz in the longitudinal direction while driving. It is likely that backlash in the lead screw is allowing for scissor lift play in the longitudinal direction. Energy is reduced and the resonance frequency is shifted higher as the scissor lift is lowered. This could be due to the fact that more force from the payload is transmitted horizontally to the lead screw nut as the scissor is lowered, effectively resulting in a more rigid system. Therefore the frequency would shift higher as the system becomes more rigid.

With this data, it is concluded that the payload will experience a higher magnitude of lower frequency vibration while driving at full operational speed when the scissor lift is up. With the scissor lift down, the payload will experience higher frequency vibration of lower magnitude.

4.3 Performance

This section focuses on the overall performance of the inspection platform. This includes maximum operation speed, payload, and angle of inclination.

4.3.1 Maximum Operational Velocity

The maximum speed requirement of the inspection tool was 2 in/sec. This maximum operational speed was calibrated using a Celesco SP2-25 linear string pot. The device contains a spring-loaded spool with 25 inches of travel and a potentiometer that outputs a voltage divided potentiometric output that varies based on the input voltage supplied.

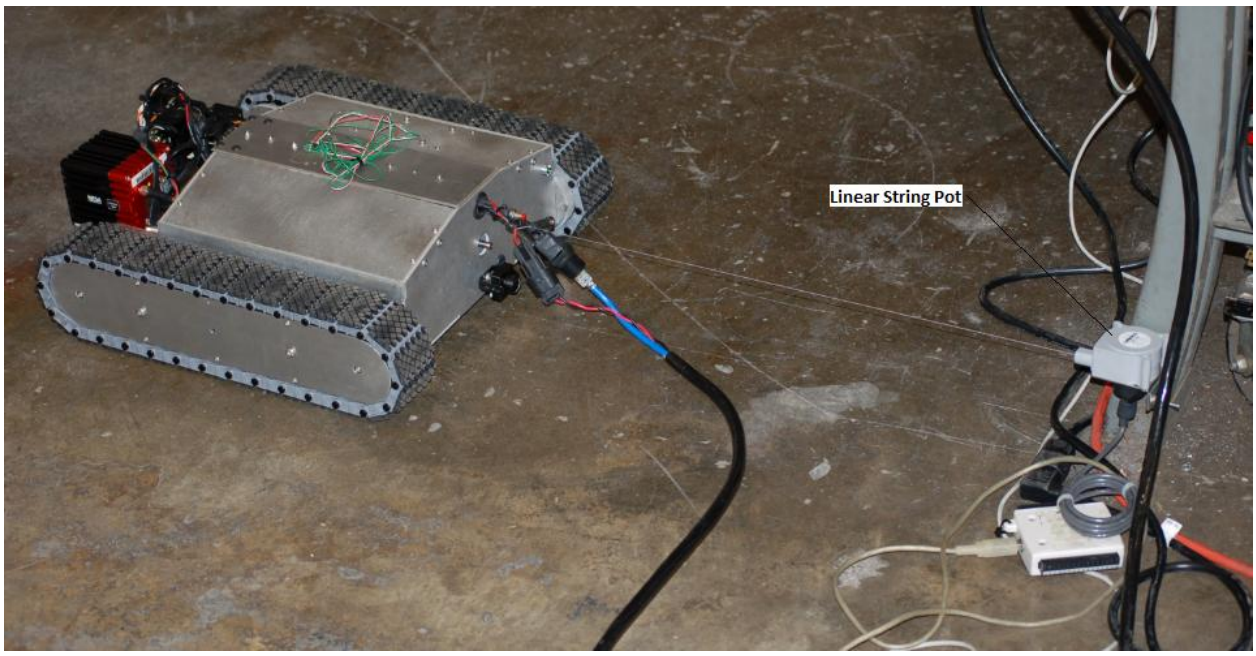

Figure 61 - Inspection tool configured with linear string pot.

Figure 61 shows the inspection tool attached to the linear string pot. Voltage was supplied using the same NI USB-6008 data acquisition device and the potentiometric output was sampled. Data was collected at 100 Hz and then converted to inches using the ratio of full stroke (25 inches) to input voltage. With a software limited speed setting of 28.8 rpm output from the drive motors, a maximum operational drive speed of 2.022 in/sec is successfully achieved.

4.3.2 Maximum Scissor Lift Payload

The scissor lift successfully lifted the required payload of 5 pounds. Scissor lift maximum operational load was tested while the scissor lift was equipped with the payload gimbal (Section 3.3.4) and instrumentation package consisting of the MESA Imaging Flash LIDAR and Flea3 inspection camera. The combined payload weight of these components and mounting hardware is just less than 1.5 pounds. Weight was then added incrementally until internal slippage occurred with the stepper motor used for raising and lowering of the scissor lift. Weight was added on top of the scissor lift as shown in Figure 62.

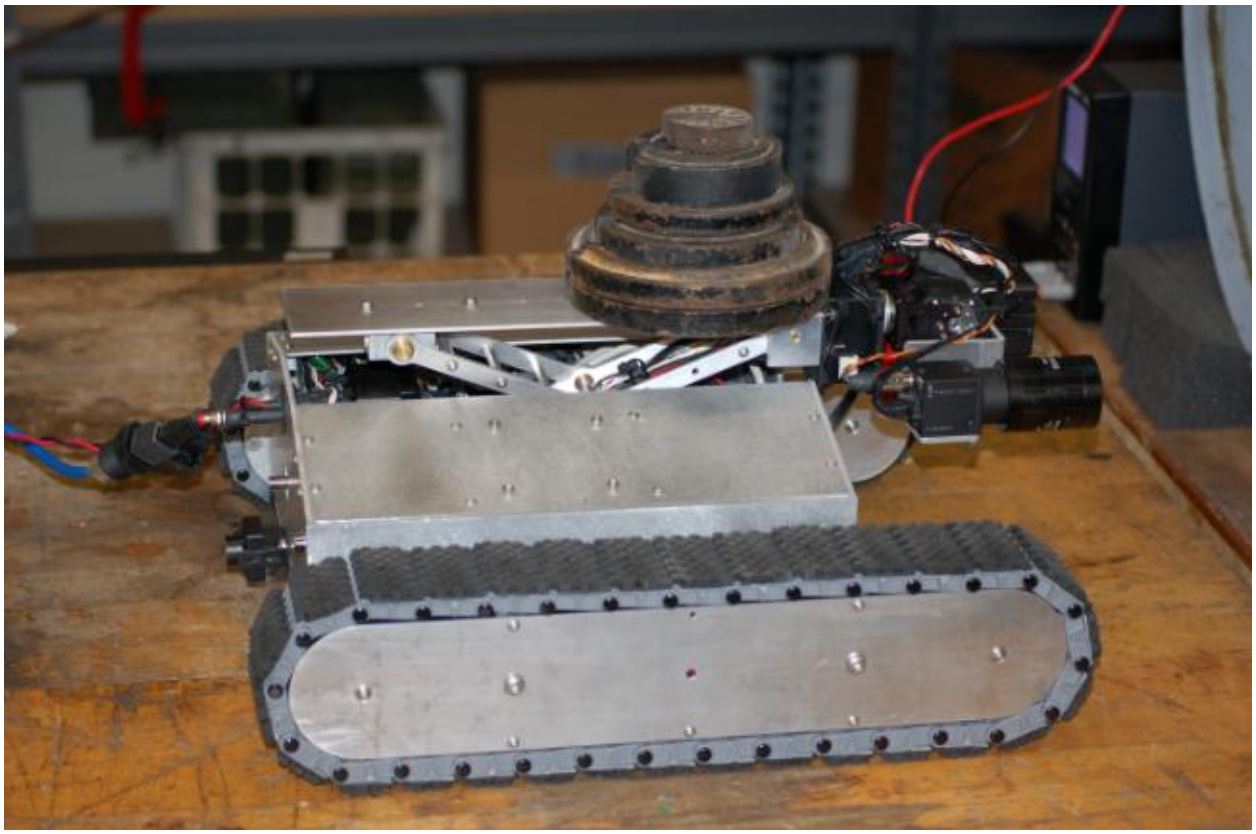

Figure 62 - Weight was added for testing of maximum scissor lifting capability.

The scissor lift was capable of lifting an additional 7 pounds before internal slipping occurred inside the stepper motor. On level ground the scissor lift is capable of lifting 8.5 pounds of additional weight added to the assembly. The lift was actually capable of raising more weight with only a few steps slipping before the motor eventually caught. However, slippage is not acceptable because the controller is calibrated at power-on using the magnetic reed switch (Section 3.3.3) and keeps track of the lift position by counting steps.

4.3.3 Maximum Angle of Inclination

The maximum angle of inclination was tested using a board covered with 150-grit sandpaper. The board was raised until slippage occurred on the tracks and the angle was measured. The inspection tool was driven at maximum operation speed and the maximum angle of inclination was measured at 40 degrees from the horizontal. gure 64 shows the test setup.

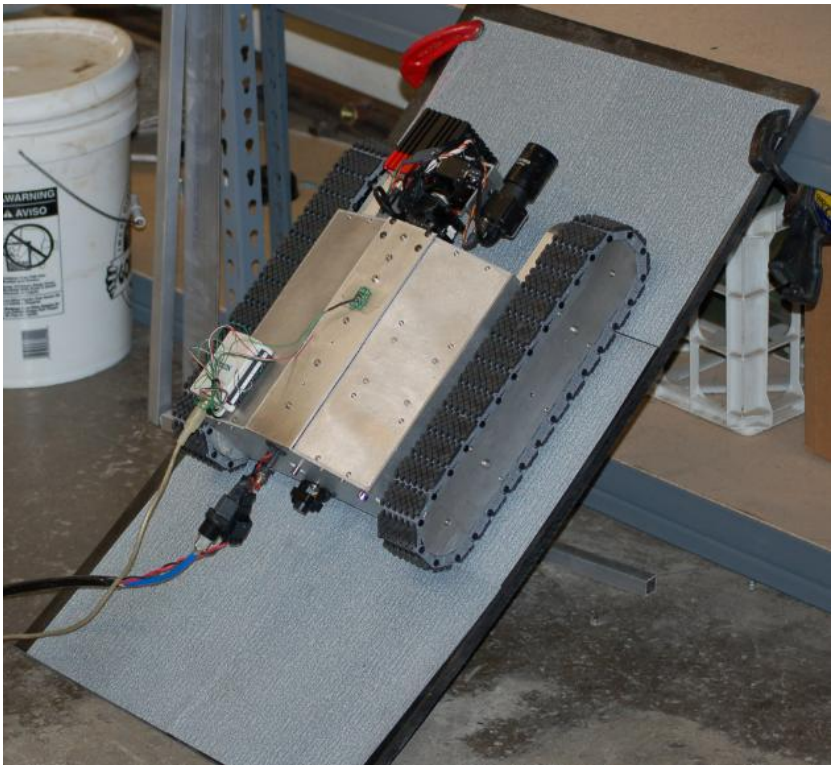

Figure 63 - Inspection tool angle of inclination testing.gure 64 - Inspection tool angle of inclination testing.

Chapter 5: Conclusion

With the field of unmanned systems showing exceptional growth, more and more mobile robots are developing the capabilities to perform various inspection tasks in environments that have not been previously breached. The continued development of new technology to support NDE inspections is needed for the advancement of internal inspection capabilities as well as mobile robotic systems such as robot vision, perception, sensing and instrumentation.

5.1 Conclusion

A robotic inspection platform was developed based on a differential-drive locomotion concept. This robotic inspection tool can climb slopes over 30 degrees while carrying a payload of well over 5 pounds. A pan/tilt gimbal was developed to allow for positioning of a payload or instrumentation package. The platform provides variable height control for the payload with a range of 7.5 inches and a maximum height of 13 inches from the ground. This was accomplished with a custom designed scissor lift apparatus. The mechanical design of the inspection platform chassis, scissor lift, and locomotion was discussed. The electro-mechanical design of the powertrain for locomotion and scissor lift was reviewed. The electrical design of the associated electronics and devices as well as communications, control, and power distribution was discussed. Finally, the performance was outlined and a test environment was successfully inspected.

5.2 Future Work

There is lots of room for future work on this project. A camber adjustment for the tracks would allow for the tracks to be adjusted for better traction with inspection environments that have curved surfaces such as pipelines.

There is a need for drive camera lighting for environments where ambient lighting is not available. LEDs would be the most appropriate form of lighting and the light output would need to be tuned to the drive cameras.

Although the effects of backlash from the scissor lift on the payload height may be removed with software, the vibrational analysis shown in Section 4.2 demonstrates that backlash may be a cause of unnecessary vibration of the payload. Future work may include removal of this backlash via a redesign of

the scissor lift powertrain. Perhaps a zero-backlash lead screw nut could be developed where springs apply a preload to keep the lead screw nut in contact with the lead screw threads at all times. This could effectively remove any play with lead screw nut and prevent unnecessary resonant vibrations experienced by the instrumentation package.

Bibliography

1. NASA. *Types of Robots*. 2003 [cited 2012 Nov. 10]; Available from: http://prime.jsc.nasa.gov/ROV/types.html.
2. Teale, E., *The Marvels of Underground Oil Railroads*, in *Popular Science* 1937, Popular Science Publishing Co.: 355 Fourth Avenue, New York, NY.
3. Harris, C., *Enhanced Pipeline Seam Assessment.* Pipeline & Gas Journal, 2011.
4. Okamoto Jr, J., et al., *Autonomous system for oil pipelines inspection.* Mechatronics, 1999. **9**(7): p. 731-743.
5. Moraleda, J., A. Ollero, and M. Orte, *A robotic system for internal inspection of water pipelines.* Robotics & Automation Magazine, IEEE, 1999. **6**(3): p. 30-41.
6. Ben-Tzvi, P., A.A. Goldenberg, and J.W. Zu, *Articulated hybrid mobile robot mechanism with compounded mobility and manipulation and on-board wireless sensor/actuator control interfaces.* Mechatronics, 2010. **20**(6): p. 627-639.
7. Mirats Tur, J.M. and W. Garthwaite, *Robotic devices for water main in-pipe inspection: A survey.* Journal of Field Robotics, 2010. **27**(4): p. 491-508.
8. Oya, T. and T. Okada, *Development of a steerable, wheel-type, in-pipe robot and its path planning.* Advanced Robotics, 2005. **19**(6): p. 635-650.
9. Bradbeer, R., et al. *An underwater robot for pipe inspection*. in *Mechatronics and Machine Vision in Practice, 1997. Proceedings., Fourth Annual Conference on*. 1997.
10. Changhwan, C., P. Byungsuk, and J. Seungho, *The Design and Analysis of a Feeder Pipe Inspection Robot With an Automatic Pipe Tracking System.* Mechatronics, IEEE/ASME Transactions on, 2010. **15**(5): p. 736-745.
11. Anthierens, C., A. Ciftci, and M. Betemps. *Design of an electro pneumatic micro robot for in-pipe inspection*. in *Industrial Electronics, 1999. ISIE '99. Proceedings of the IEEE International Symposium on*. 1999.
12. Rome, E., et al., *Towards autonomous sewer robots: the MAKRO project.* Urban Water, 1999. **1**(1): p. 57-70.

13. Nassiraei, A.A.F., et al. *Concept and Design of A Fully Autonomous Sewer Pipe Inspection Mobile Robot "KANTARO"*. in *Robotics and Automation, 2007 IEEE International Conference on*. 2007.
14. Ltd, I.S. *Inuktun - World-class Remotely Controlled Camera Robotic Pipe Inspection Systems and Robotic Crawlers*. [cited 2012 November 12]; Available from: http://www.inuktunusa.com.
15. Technologies, P. *Pure Technologies | Pipeline Inspection | Condition Assessment*. [cited 2012 November 15]; Available from: http://www.puretechltd.com/.
16. LLC, E. *Pipeline Inspection, CCTV & Drain Inspection Cameras, Sewer Crawler Camera*. [cited 2012 November 15]; Available from: http://www.envirosight.com/.
17. Yamauchi, B.M., *PackBot: a versatile platform for military robotics.* 2004: p. 228-237.
18. Wang, Z.D., Y. Gu, and Y.S. Wang, *A review of three magnetic NDT technologies.* Journal of Magnetism and Magnetic Materials, 2012. **324**(4): p. 382-388.
19. Bickerstaff, R., et al., *Review of sensor technologies for in-line inspection of natural gas pipelines.* Sandia National Laboratories, Albuquerque, NM, 2002.
20. Kishawy, H.A. and H.A. Gabbar, *Review of pipeline integrity management practices.* International Journal of Pressure Vessels and Piping, 2010. **87**(7): p. 373-380.
21. Guo, Y., et al., *Development of ultrasonic phased array systems for applications in tube and pipe inspection.* AIP Conference Proceedings, 2012. **1430**(1): p. 1897-1904.
22. Sonyok, D., B. Zhang, and J. Zhang. *Applications of Non-Destructive Evaluation (NDE) in Pipeline Inspection*. in *Pipelines 2008—Pipeline Asset Management@ sMaximizing Performance of our Pipeline Infrastructure*. 2008. ASCE.
23. Safizadeh, M. and M. Hasanian, *Gas Pipeline Corrosion Mapping Using Pulsed Eddy Current Technique.* International Journal of Advanced Design and Manufacturing Technology, 2012. **5**(1): p. 11-18.
24. Washabaugh, A., et al. *Eddy Current Sensor Arrays for Pipeline Inspection With and Without Coatings*. 2010. ASME.
25. Amann, M.C., et al., *Laser ranging: a critical review of usual techniques for distance measurement.* Optical Engineering, 2001. **40**(1): p. 10-19.
26. Nüchter, A., *3D robotic mapping: the simultaneous localization and mapping problem with six degrees of freedom*. Vol. 52. 2009: Springer.

27. Geng, J., *Structured-light 3D surface imaging: a tutorial.* Advances in Optics and Photonics, 2011. **3**(2): p. 128-160.
28. Autodesk. *Autodesk - Autodesk Inventor Services & Support - Stress analysis assumptions*. 2012 [cited 2012 November 20]; Available from: http://usa.autodesk.com/adsk/servlet/ps/dl/item?siteID=123112&id=7263238&linkID=9242018.
29. Budynas, R.G. and J.K. Nisbett, *Shigley's mechanical engineering design*. Vol. 10. 2008: McGraw-Hill.
30. Lynxmotion. *Lynxmotion Robot Kits*. 2012 [cited 2012 August 5]; Available from: http://www.lynxmotion.com/.
31. Spackman, H., *Mathematical Analysis of Scissor Lifts*, 1989, NAVAL OCEAN SYSTEMS CENTER SAN DIEGO CA.
32. Dynetic. *Brushless vs Brushed Motors*. [cited 2012 November 19]; Available from: http://www.dynetic.com/brushless%20vs%20brushed.htm.
33. Inc., M.D. *The "Stepper Versus Brushless Servo" myth*. Design Trends, 2007.
34. Berg, W.M., *Master Inch/Metric Catalog*.
35. INC, R.*:::ROBOTIS:::*. [cited 2012 September 10]; Available from: http://www.robotis.com/xe/dynamixel_en.
36. Kushner, D. *The Making of Arduino*. IEEE Spectrum, 2011. October.
37. Arduino. *Arduino - Environment*. [cited 2012 November 15]; Available from: http://arduino.cc/en/Guide/Environment.
38. Arduino. *Arduino - ArduinoBoardMega2560*. [cited 2012 November 15]; Available from: http://arduino.cc/en/Main/ArduinoBoardMega2560.
39. Hambley, A.R., *Electrical engineering: principles and applications*. 2008: Pearson Prentice Hall.

Appendix I – Associated CAD Drawings

The following drawings support the build of the inspection tool base platform. All parts were machined out of aluminum using either CNC or Waterjetting. Not all dimensions are listed due to the complexity of some parts. Those dimensions were instead referenced on the 3D CAD file that was included with the drawing when submitted to the machine shop.

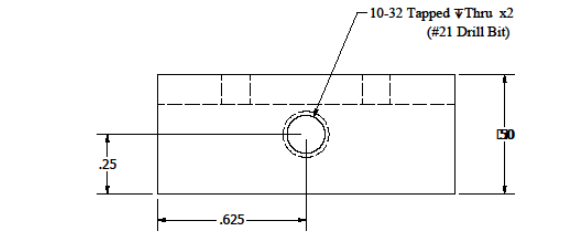

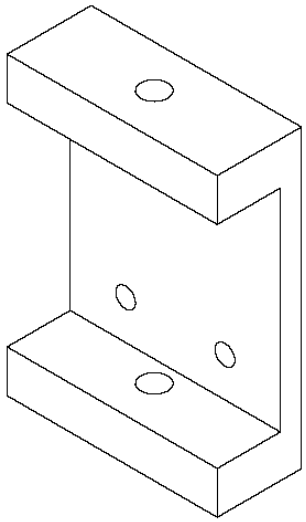

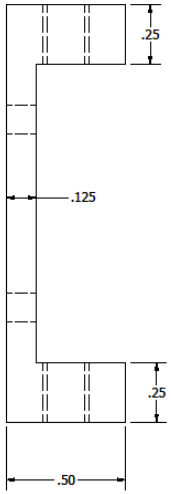

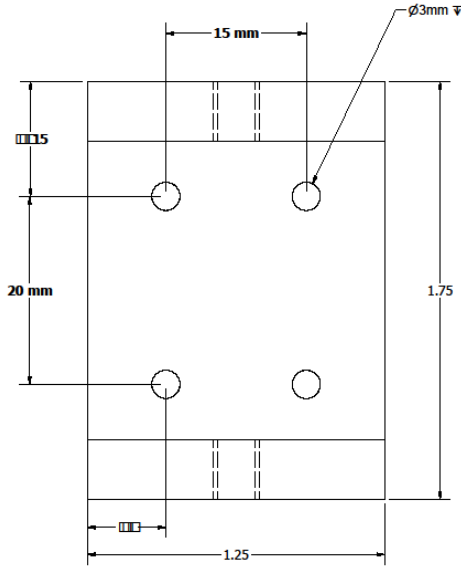

-All dimensions English Units unless otherwise noted
-Standard tolerances

Contact:
Alex Cope
bcope@vt.ed
434-806-8178

Quantity: 1

DRAWN Alex Cope	8/23/2012	
CHECKED		TITLE: Carriage Bracket
QA		
MFG		
APPROVED		SIZE C / DWG NO Carriage Bracket / REV / SCALE / SHEET 1 OF 1

PRODUCED BY AN AUTODESK EDUCATIONAL PRODUCT

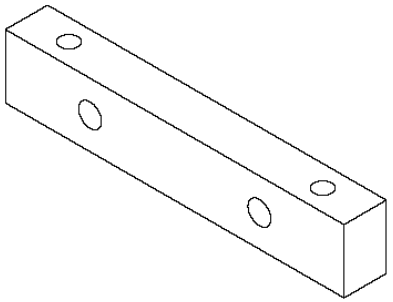

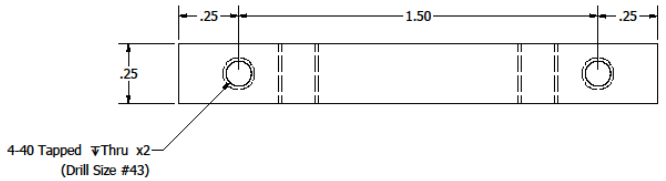

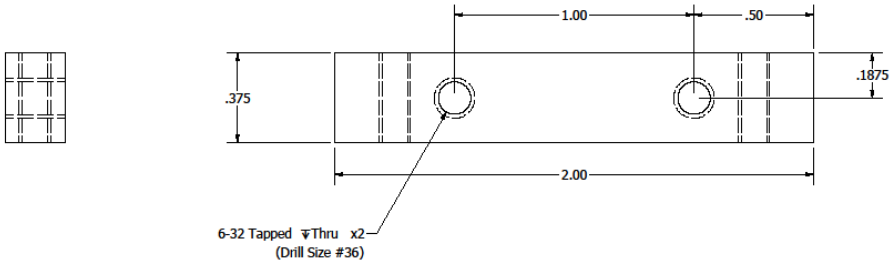

-All dimensions English Units unless otherwise noted
-Standard tolerances

Contact:
Alex Cope
bcope@vt.edu
434-806-8178

Quantity: 4

DRAWN Alex Cope	8/29/2012	VT Mechanical Engineering
CHECKED		TITLE: Chassis Top Mounting Tab
QA		
MFG		
APPROVED		
SIZE C	DWG NO Chassis Top Mounting Tab	REV
SCALE	SHEET 1 OF 1	

PRODUCED BY AN AUTODESK EDUCATIONAL PRODUCT

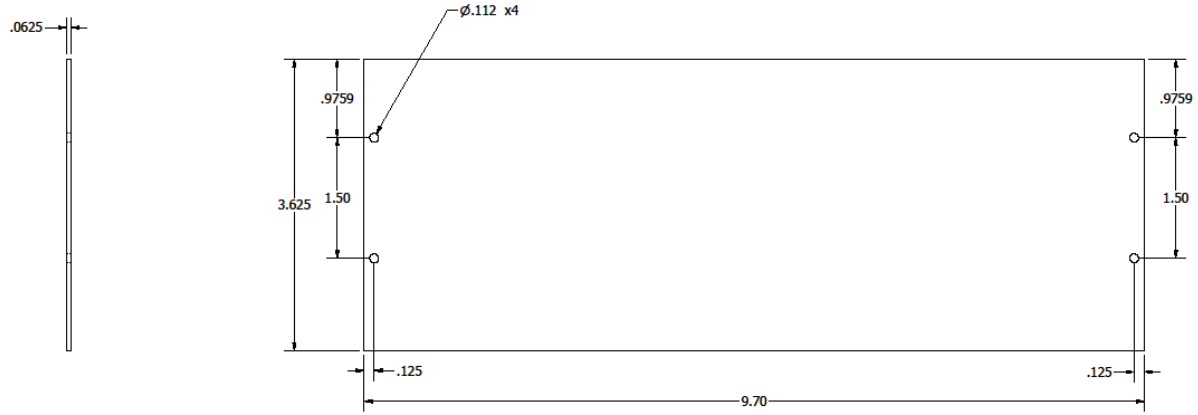

-All dimensions English Units unless otherwise noted
-Standard tolerances

Contact:
Alex Cope
bcope@vt.edu
434-806-8178

Quantity: 2

DRAWN Alex Cope	8/29/2012	VT Mechanical Engineering
CHECKED		TITLE: Chassis Top
QA		
MFG		
APPROVED		SIZE C / DWG NO Chassis Top / REV
		SCALE / SHEET 1 OF 1

PRODUCED BY AN AUTODESK EDUCATIONAL PRODUCT

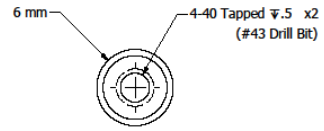

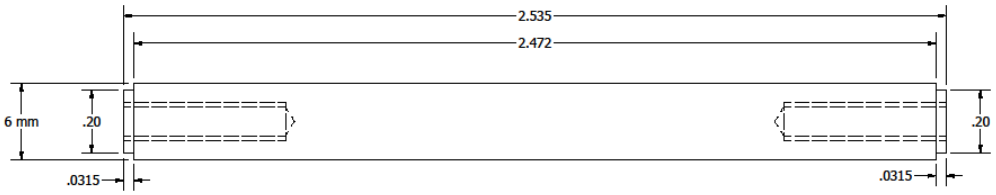

Shaft tolerances:
-Straight within .0003 in/in
-⌀ (+.0000
-.0002)

-All dimensions English Units unless otherwise noted

Contact:
Alex Cope
bcope@vt.ed
434-806-8178

Quantity: 2
Material: Aluminum

DRAWN Alex Cope	8/23/2012	VT Mechanical Engineering
CHECKED		TITLE: Drive Shaft
QA		
MFG		
APPROVED		SIZE C · DWG NO Drive Shaft · REV
		SCALE · SHEET 1 OF 1

PRODUCED BY AN AUTODESK EDUCATIONAL PRODUCT

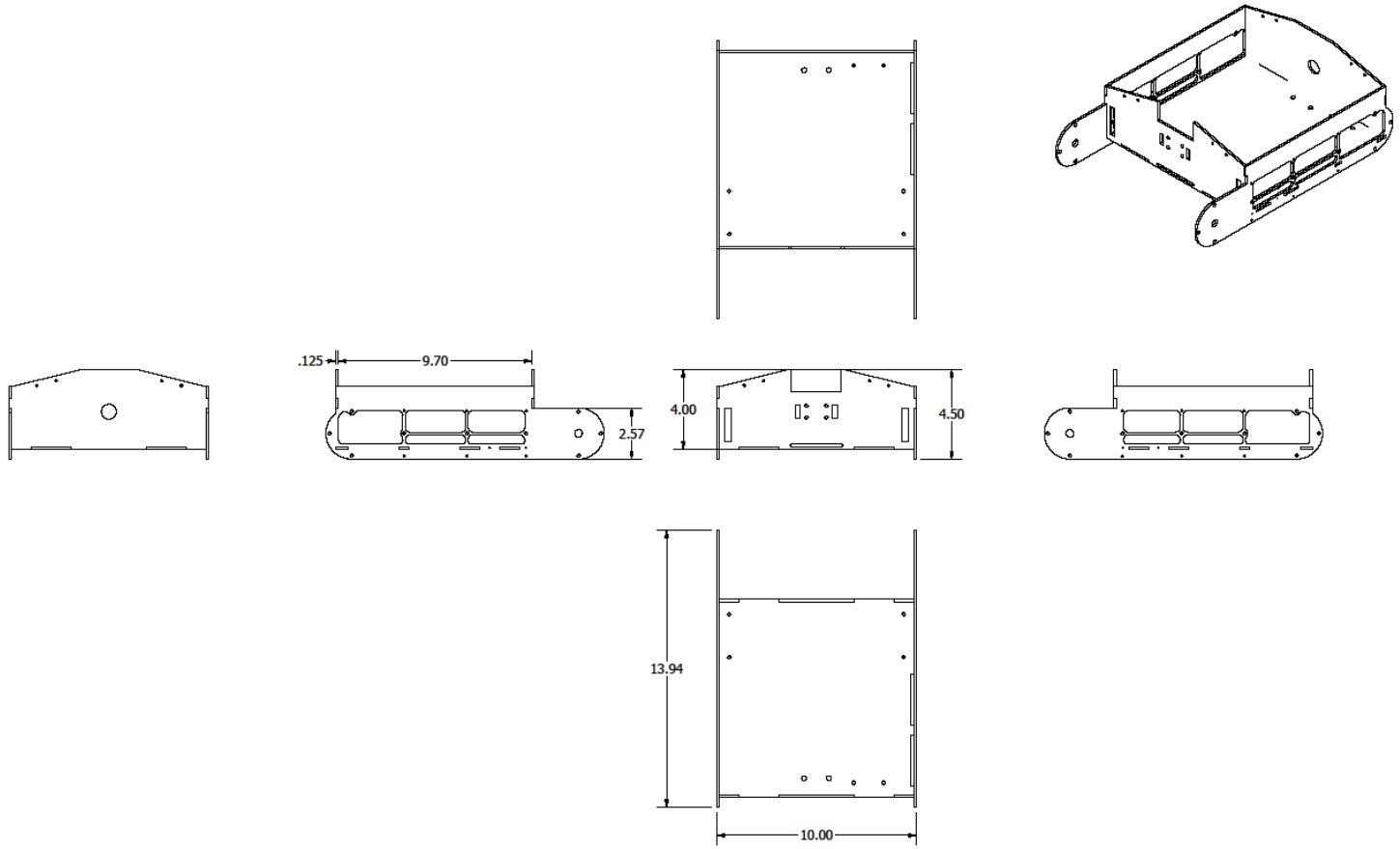

DRAWN Alex Cope	12/23/2012	
CHECKED		TITLE Chassis
QA		
MFG		
APPROVED		SIZE C / DWG NO / REV
		SCALE / SHEET 1 OF 1

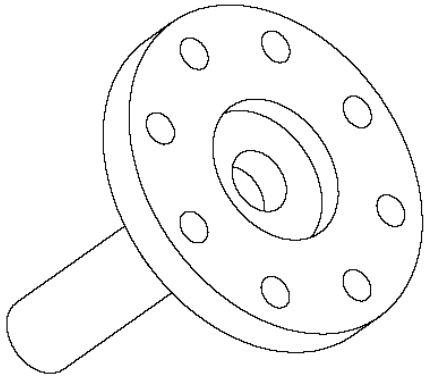

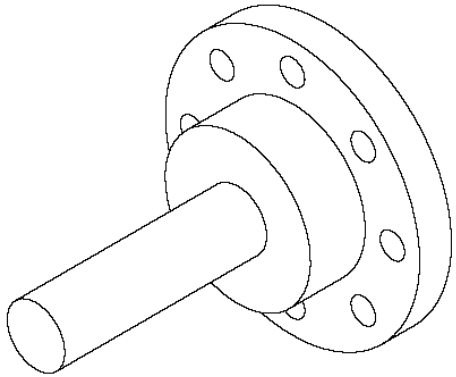

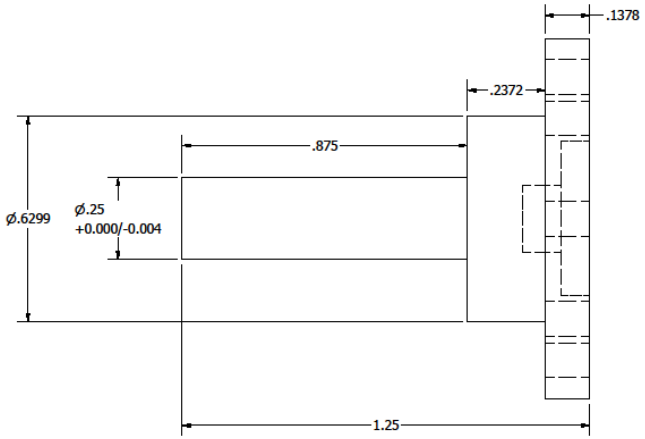

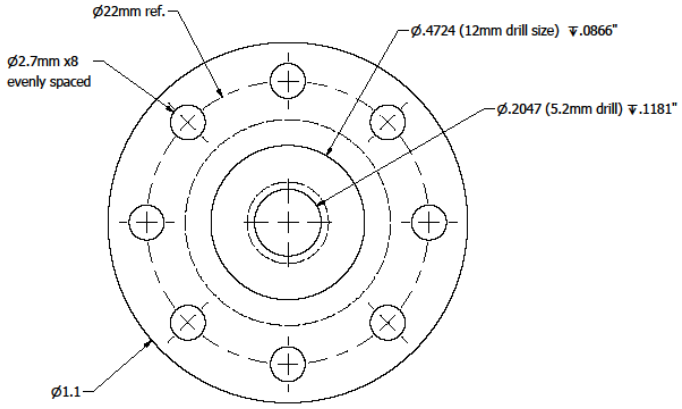

-All dimensions English Units unless otherwise noted
-Standard tolerances
-Refer to STEP file for all other dimensions

Contact:
Alex Cope
bcope@vt.edu
434-806-8178

Quantity: 2
Material: Aluminum

DRAWN Alex Cope	10/18/2012	VT Mechanical Engineering
CHECKED		TITLE: Dynamixel Motor Shaft
QA		
MFG		
APPROVED		SIZE C / DWG NO Dynamixel Motor Shaft / REV
		SCALE / SHEET 1 OF 1

PRODUCED BY AN AUTODESK EDUCATIONAL PRODUCT

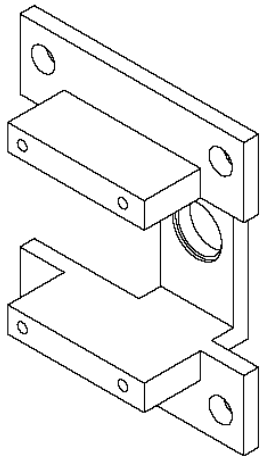

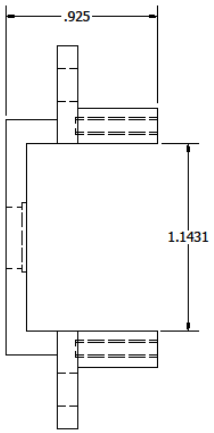

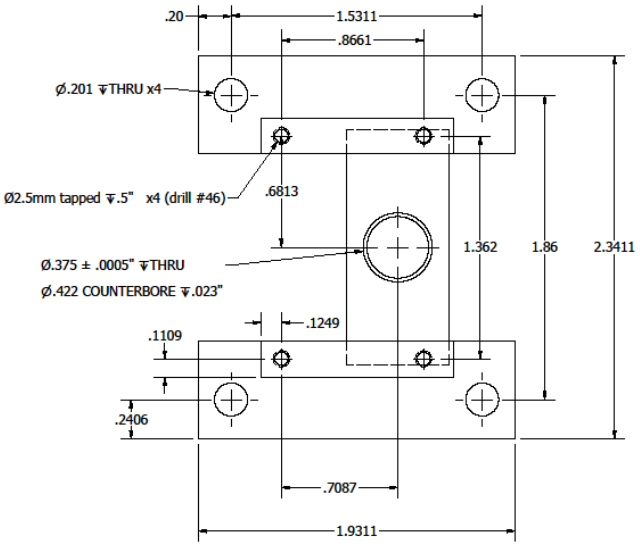

-All dimensions English Units unless otherwise noted
-Standard tolerances
-Refer to STEP file for all other dimensions

Contact:
Alex Cope
bcope@vt.edu
434-806-8178

Quantity: 2
Material: Aluminum

DRAWN Alex Cope	10/18/2012	VT Mechanical Engineering
CHECKED		TITLE: Dynamixel Mount
QA		
MFG		
APPROVED		SIZE C / DWG NO Dynamixel Mount / REV
		SCALE / SHEET 1 OF 1

PRODUCED BY AN AUTODESK EDUCATIONAL PRODUCT

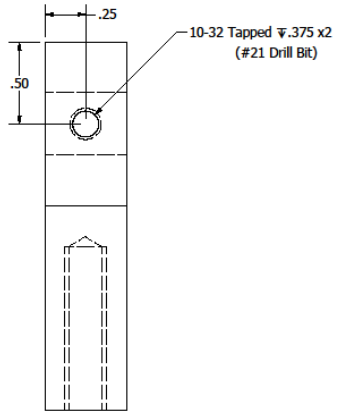

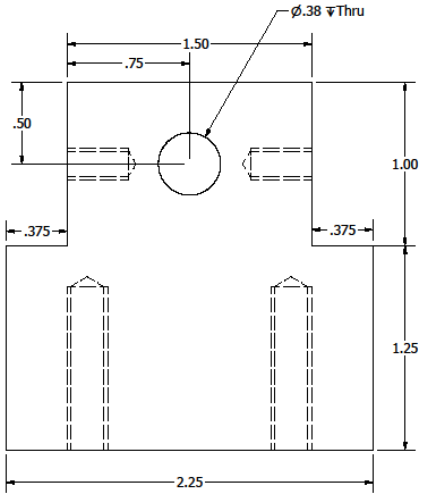

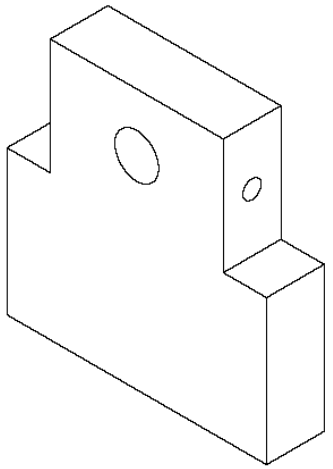

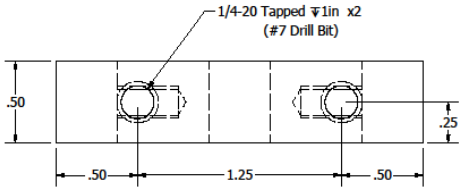

-All dimensions English Units unless otherwise noted
-Standard tolerances

Contact:
Alex Cope
bcope@vt.ed
434-806-8178

Quantity: 1

DRAWN Alex Cope	8/23/2012	VT Mechanical Engineering	
CHECKED		TITLE: Front Pillow Block	
QA			
MFG			
APPROVED		SIZE C	DWG NO Front Pillow Block / REV
		SCALE	SHEET 1 OF 1

PRODUCED BY AN AUTODESK EDUCATIONAL PRODUCT

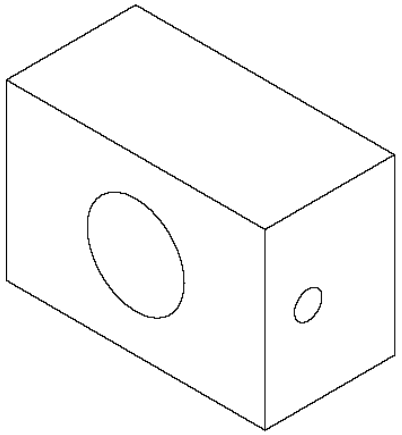

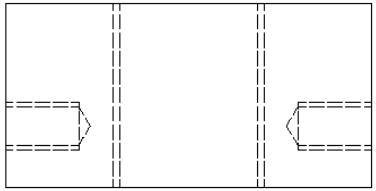

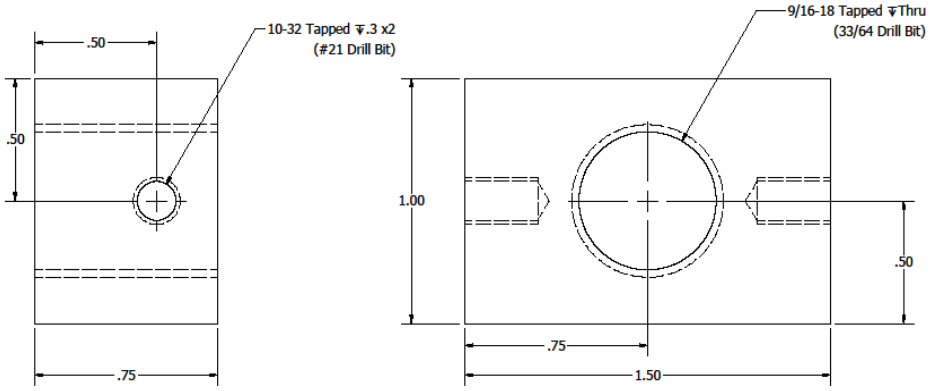

-All dimensions English Units unless otherwise noted
-Standard tolerances

Contact:
Alex Cope
bcope@vt.ed
434-806-8178

Quantity: 1

DRAWN Alex Cope	8/23/2012	VT Mechanical Engineering
CHECKED		TITLE: Lead Screw Rectangular Flange
QA		
MFG		
APPROVED		SIZE C / DWG NO Lead Screw Rectangular Flange / REV
		SCALE / SHEET 1 OF 1

PRODUCED BY AN AUTODESK EDUCATIONAL PRODUCT

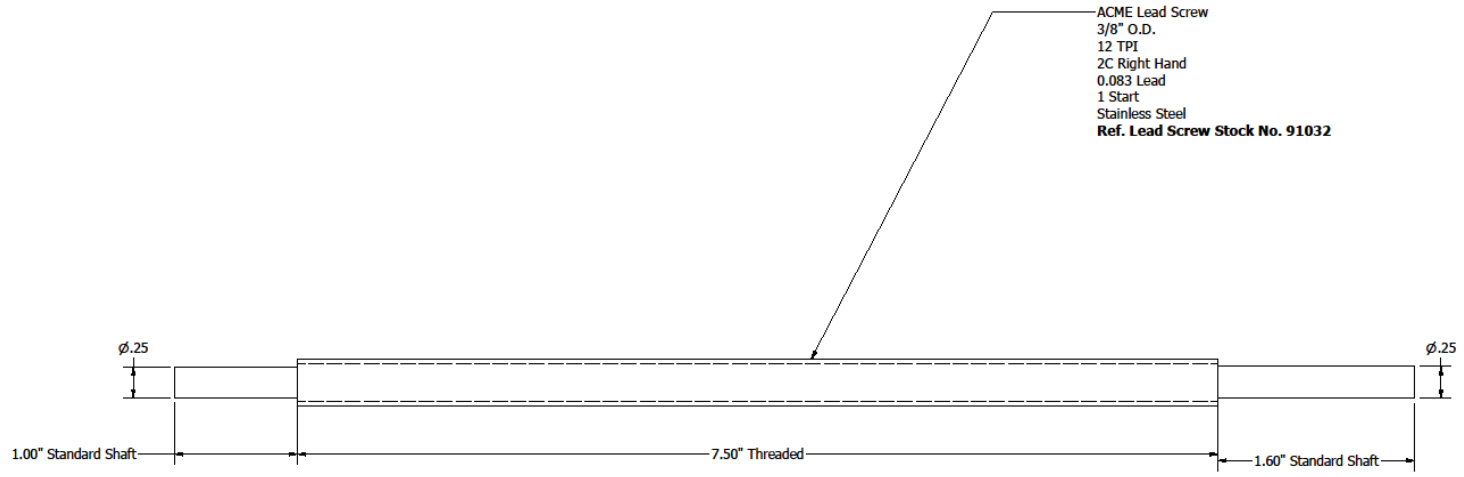

-Use standard 1/4" shaft tolerances for ends

DRAWN Alex Cope	8/6/2012	Virginia Tech Mechanical Engineering
CHECKED		TITLE: LEAD SCREW
QA		
MFG		
APPROVED		
SIZE C	DWG NO Lead Screw	REV 0
SCALE	SHEET 1 OF 1	

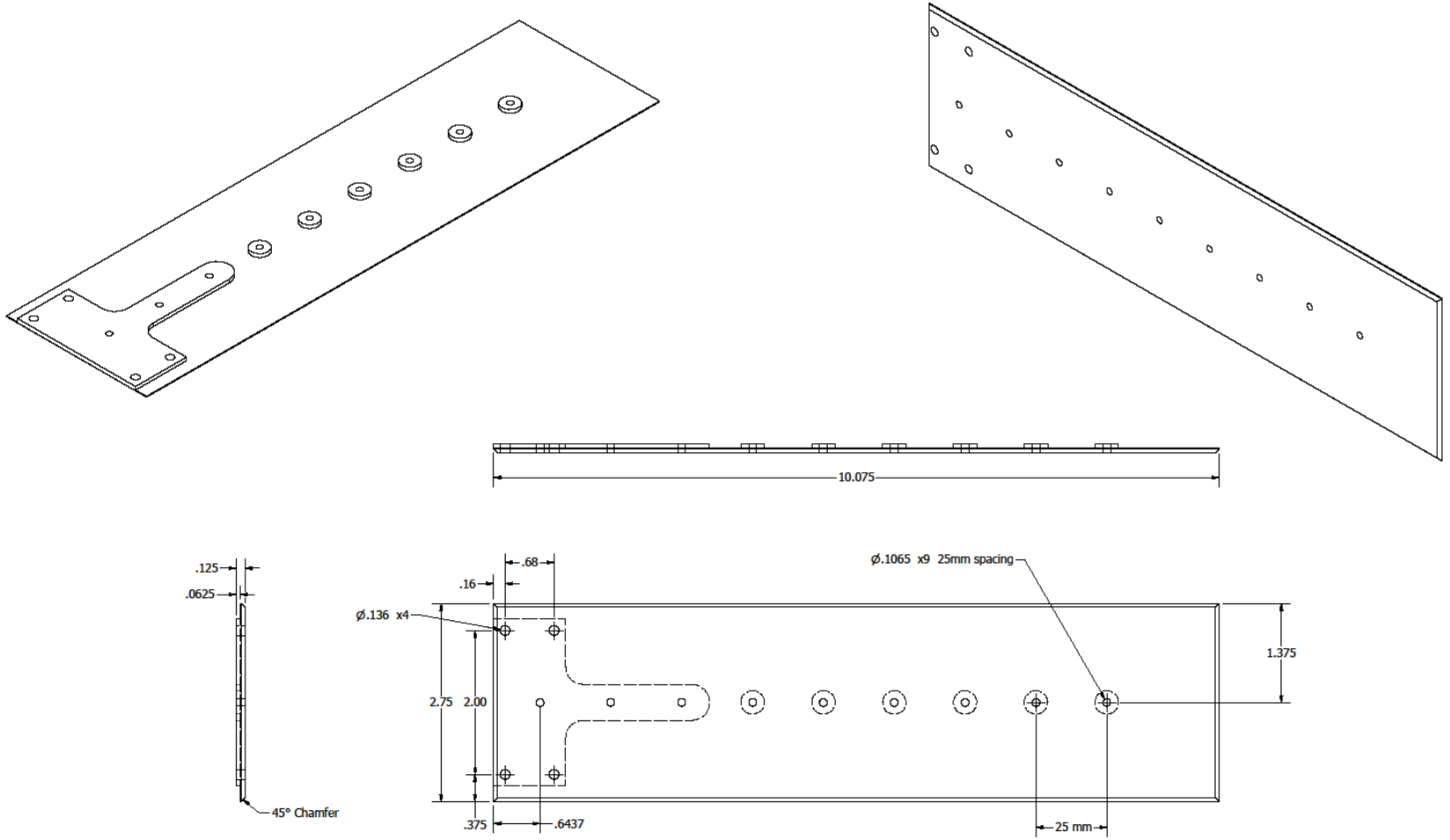

Quantity: 1
Material: Aluminum

-All holes ↧THRU
-Refer to STEP file for other dimensions
-All dimensions English Units unless otherwise noted
-Standard tolerances

Contact:
Alex Cope
bcope@vt.edu
434-806-8178

DRAWN Alex Cope	9/11/2012	VT Mechanical Engineering
CHECKED		TITLE: Payload Mount - Top
QA		
MFG		
APPROVED		
SIZE C	DWG NO Payload Mount - Top	REV
SCALE	SHEET 1 OF 1	

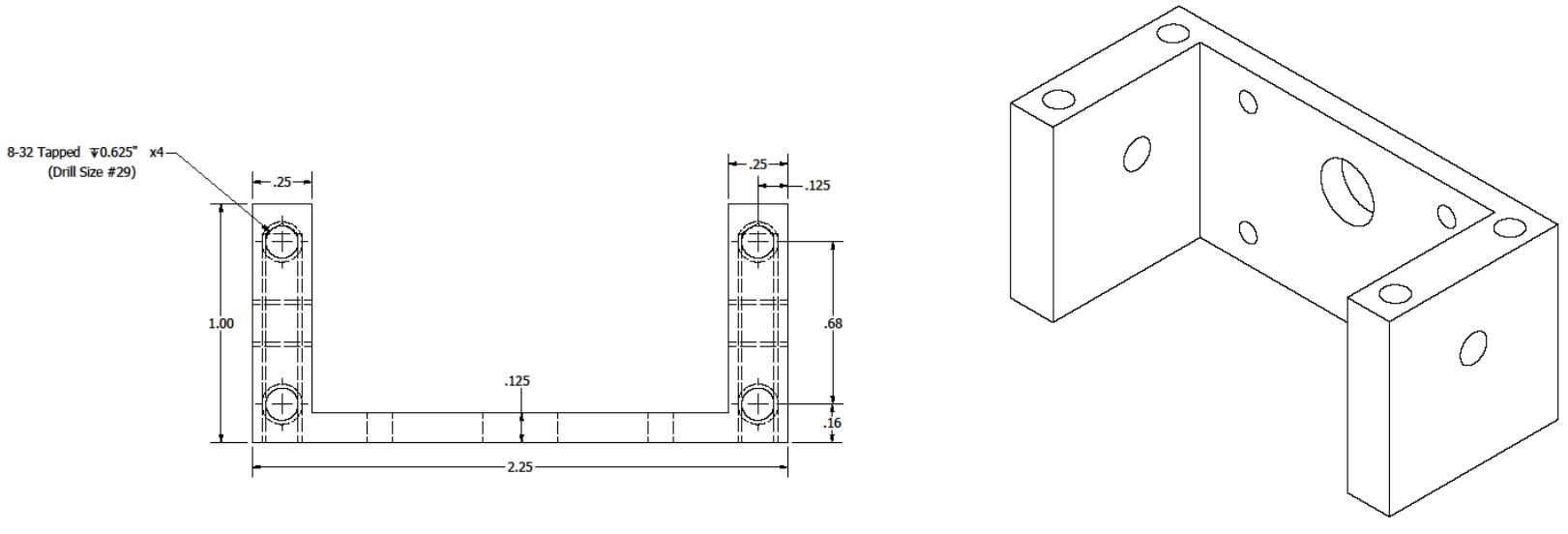

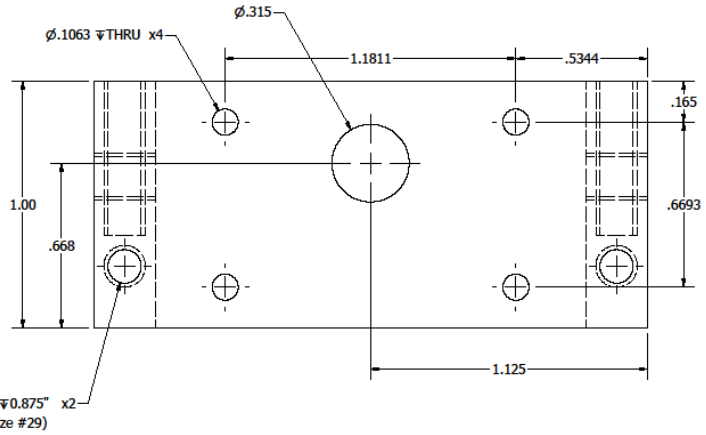

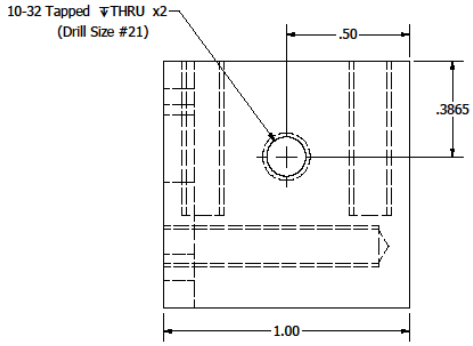

Quantity: 1

-Refer to STEP file for other dimensions
-All dimensions English Units unless otherwise noted
-Standard tolerances

Contact:
Alex Cope
bcope@vt.edu
434-806-8178

DRAWN Alex Cope	9/4/2012	VT Mechanical Engineering
CHECKED		TITLE: Payload Mount
QA		
MFG		
APPROVED		
		SIZE C / DWG NO Payload Mount / REV
		SCALE / SHEET 1 OF 1

PRODUCED BY AN AUTODESK EDUCATIONAL PRODUCT

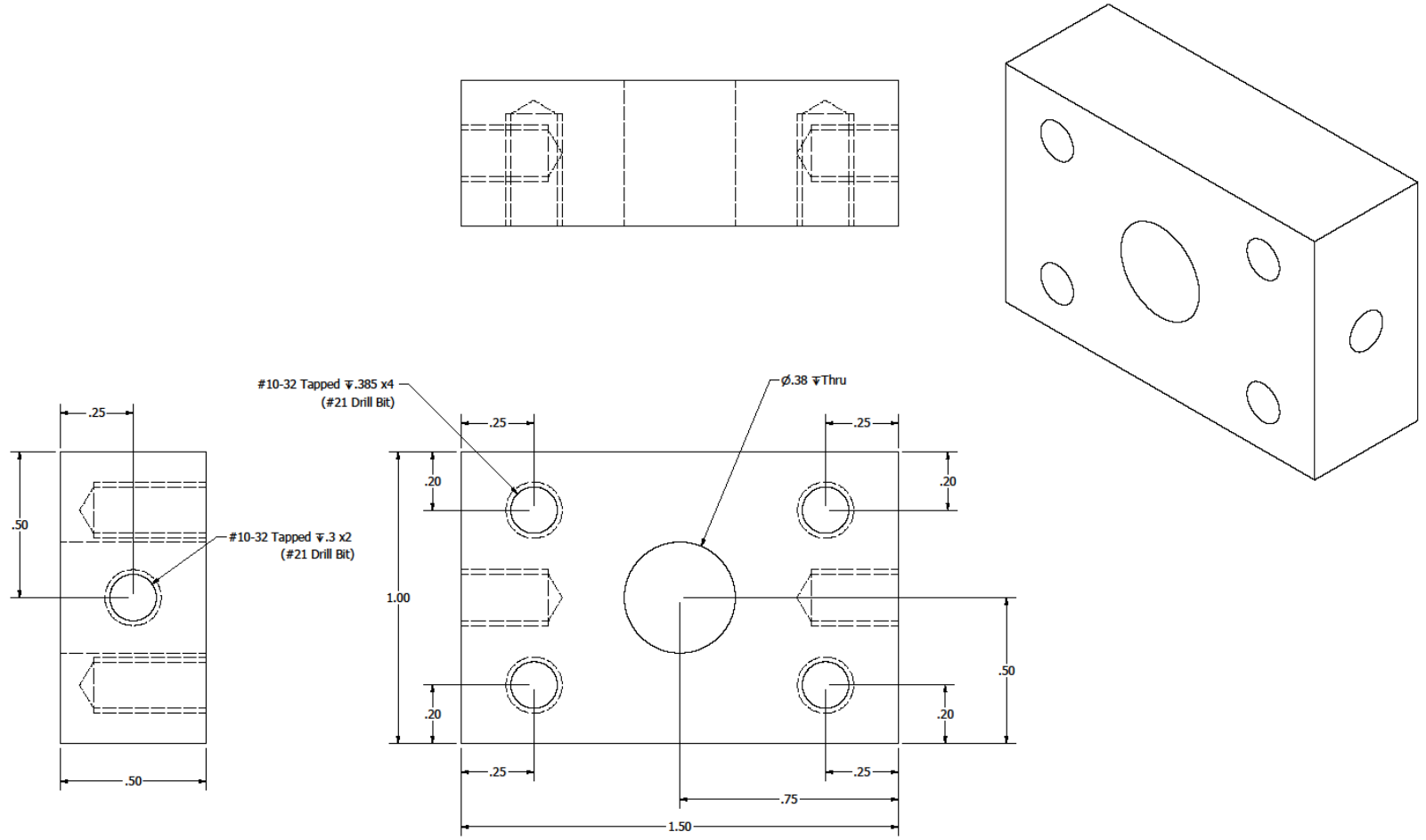

-All dimensions English Units unless otherwise noted
-Standard tolerances

Contact:
Alex Cope
bcope@vt.ed
434-806-8178

DRAWN Alex Cope	8/23/2012	VT Mechanical Engineering
CHECKED		TITLE: Rear Pillow Block
QA		
MFG		
APPROVED		SIZE C / DWG NO Rear Pillow Block / REV
		SCALE / SHEET 1 OF 1

PRODUCED BY AN AUTODESK EDUCATIONAL PRODUCT

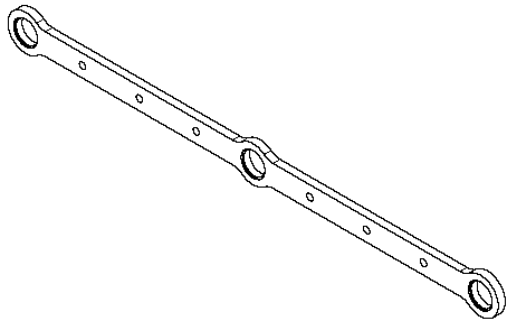

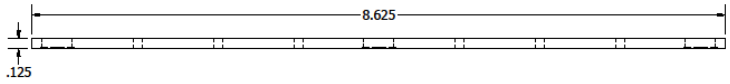

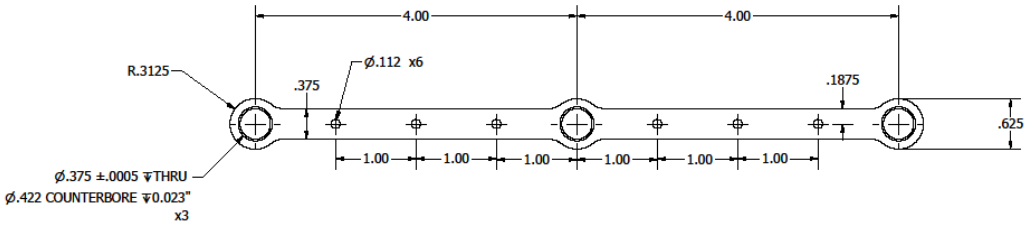

-Refer to STEP file for other dimensions
-All dimensions English Units unless otherwise noted
-Standard tolerances

Contact:
Alex Cope
bcope@vt.edu
434-806-8178

Quantity: 4

DRAWN Alex Cope	9/5/2012	VT Mechanical Engineering
CHECKED		TITLE: Scissor Lift Member
QA		
MFG		
APPROVED		
		SIZE C / DWG NO Scissor Lift Member / REV
		SCALE / SHEET 1 OF 1

PRODUCED BY AN AUTODESK EDUCATIONAL PRODUCT

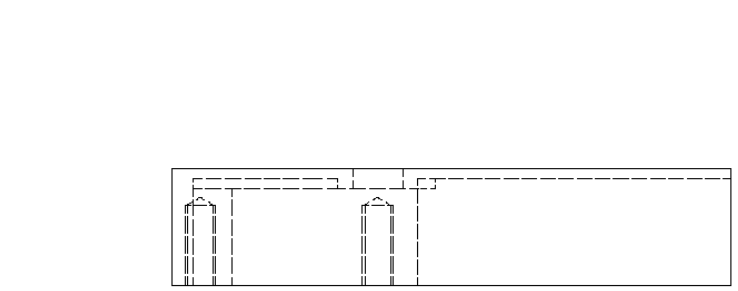

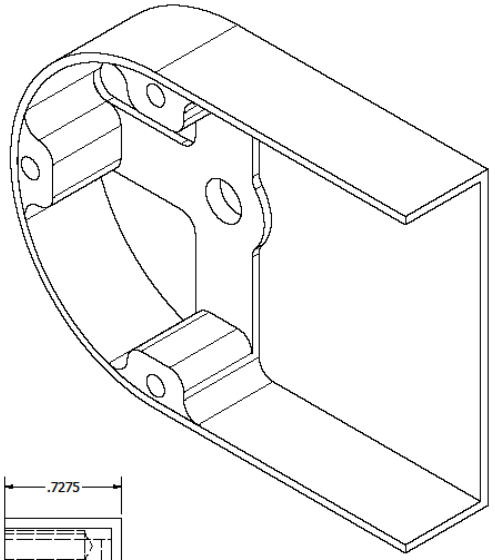

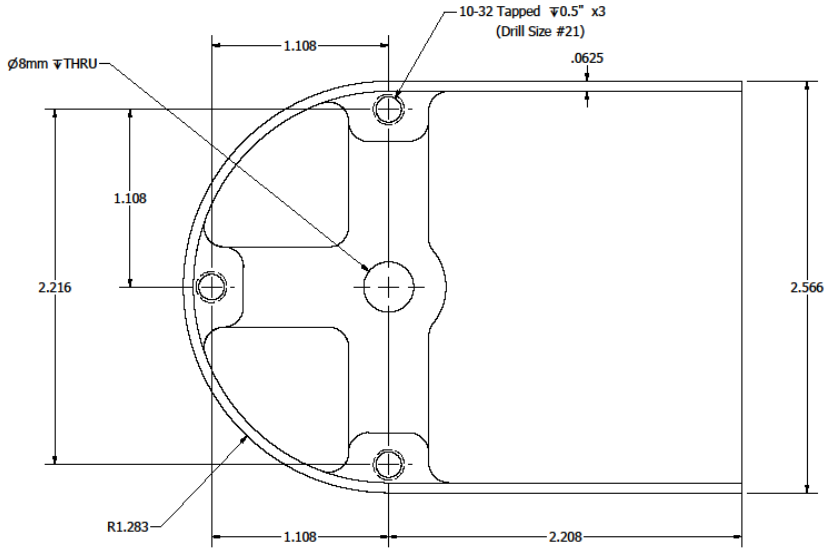

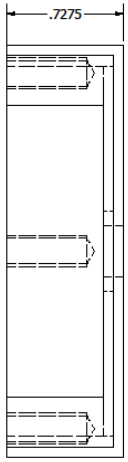

Quantity: 2

-Refer to STEP file for other dimensions
-All dimensions English Units unless otherwise noted
-Standard tolerances

Contact:
Alex Cope
bcope@vt.edu
434-806-8178

DRAWN Alex Cope	9/4/2012	VT Mechanical Engineering	
CHECKED		TITLE Sprocket Cover	
QA			
MFG			
APPROVED		SIZE C	DWG NO Sprocket Cover REV
		SCALE	SHEET 1 OF 1

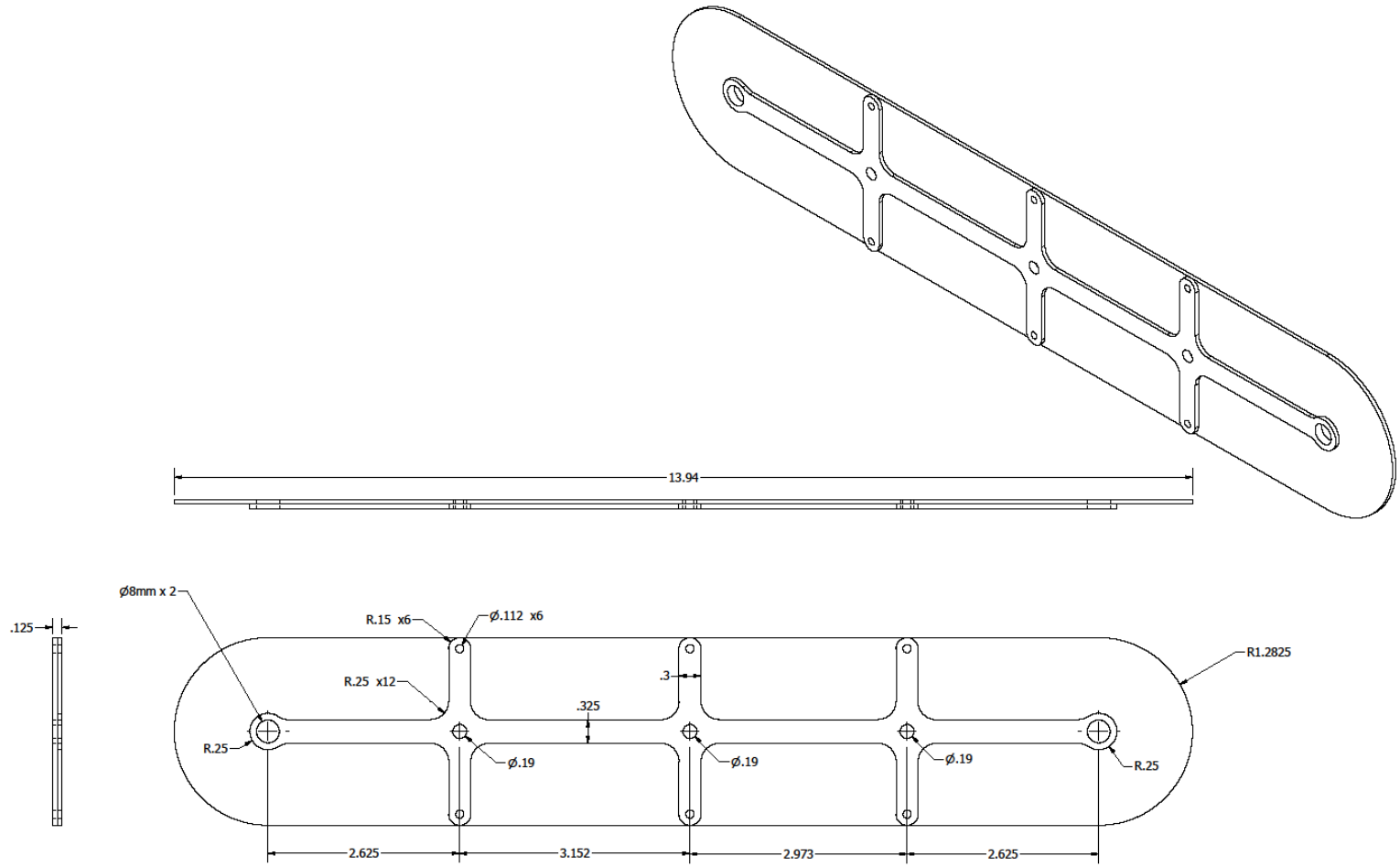

Quantity: 2
Material: Aluminum

-All holes ↧THRU
-Refer to STEP file for other dimensions
-All dimensions English Units unless otherwise noted
-Standard tolerances

Contact:
Alex Cope
bcope@vt.edu
434-806-8178

DRAWN Alex Cope	9/11/2012	VT Mechanical Engineering
CHECKED		TITLE Track Cover
QA		
MFG		
APPROVED		
SIZE C	DWG NO Track Cover	REV
SCALE	SHEET 1 OF 1	

PRODUCED BY AN AUTODESK EDUCATIONAL PRODUCT

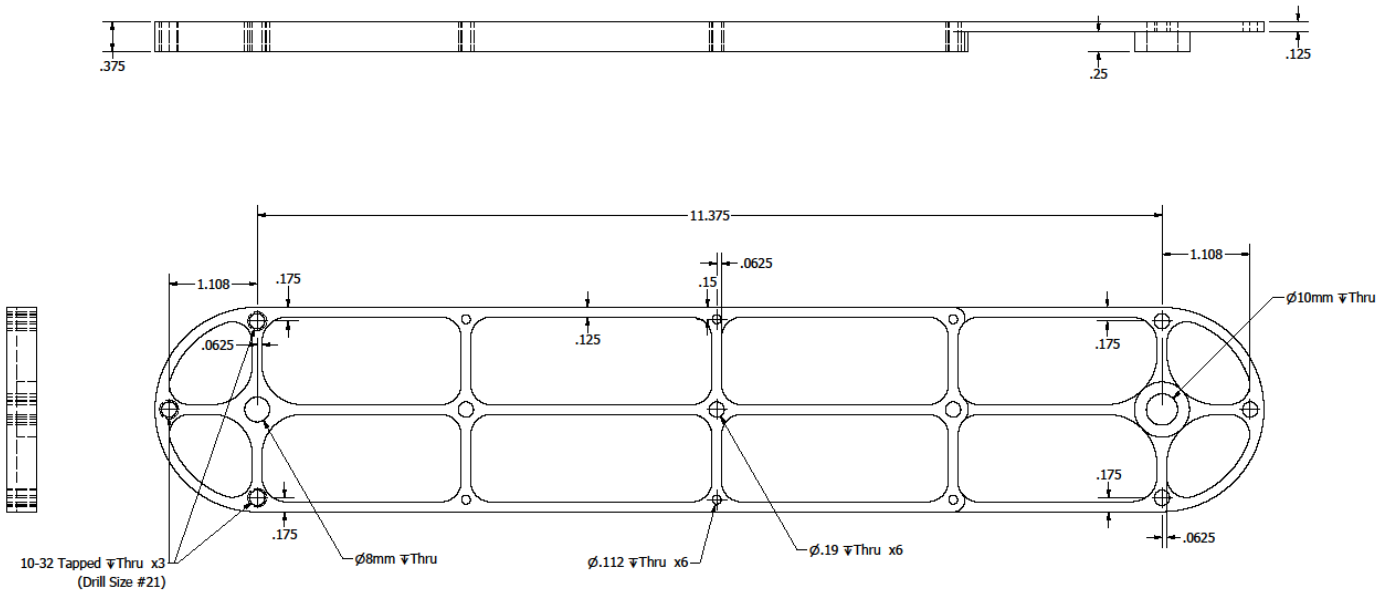

-Refer to STEP file for other dimensions
-All dimensions English Units unless otherwise noted
-Standard tolerances

Contact:
Alex Cope
bcope@vt.ed
434-806-8178

Quantity: 2

DRAWN Alex Cope	8/28/2012	VT Mechanical Engineering
CHECKED		TITLE: Track Spacer
QA		
MFG		
APPROVED		
SIZE C	DWG NO Track Spacer	REV
SCALE	SHEET 1 OF 1	

PRODUCED BY AN AUTODESK EDUCATIONAL PRODUCT

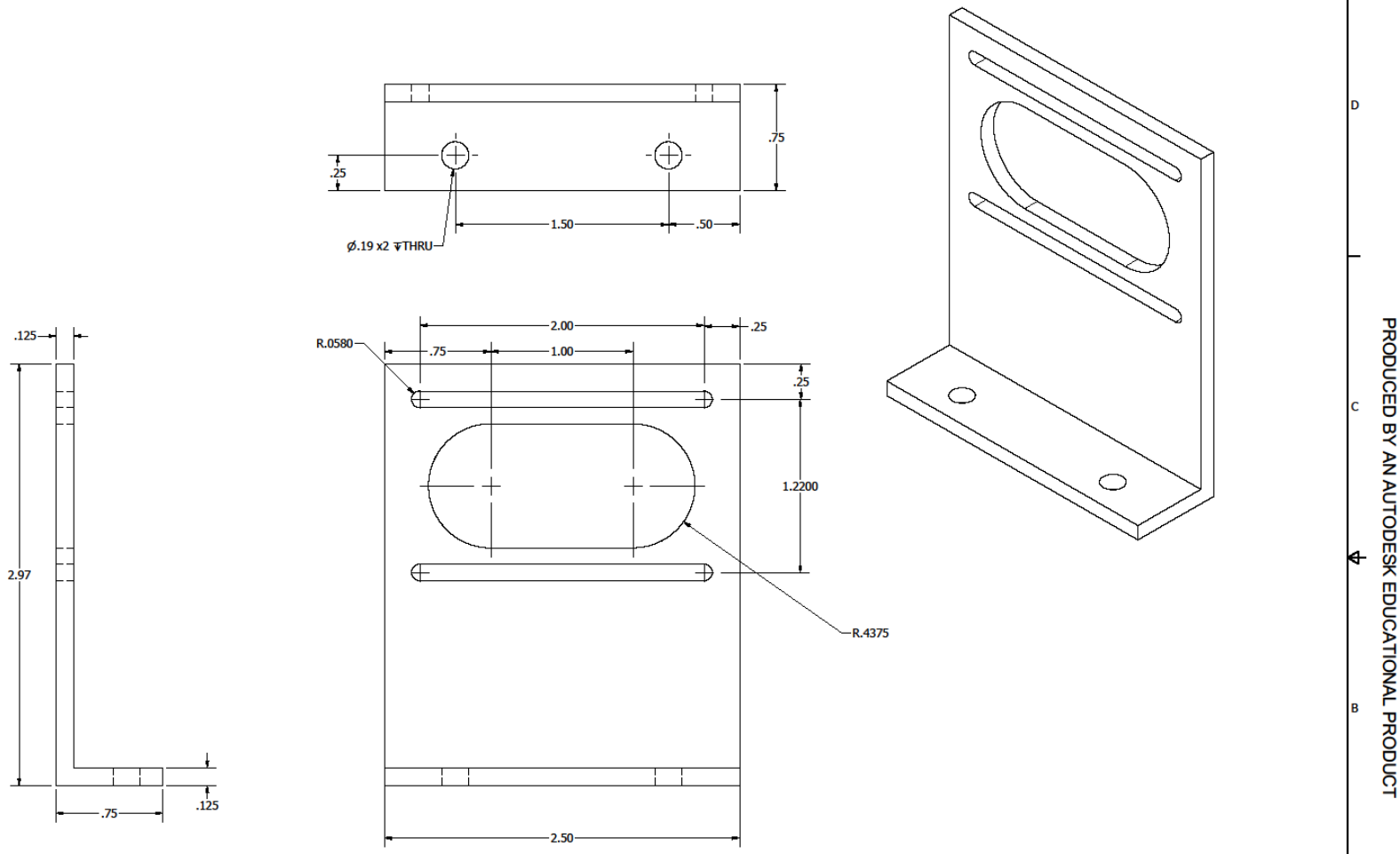

DRAWN Alex Cope	8/17/2012	Virginia Tech Mechanical Engineering
CHECKED		TITLE: Motor Mount - NEMA 17 Quantity: 1
QA		
MFG		
APPROVED		SIZE C / DWG NO Motor Mount - NEMA 17 / REV
		SCALE / SHEET 1 OF 1

PRODUCED BY AN AUTODESK EDUCATIONAL PRODUCT

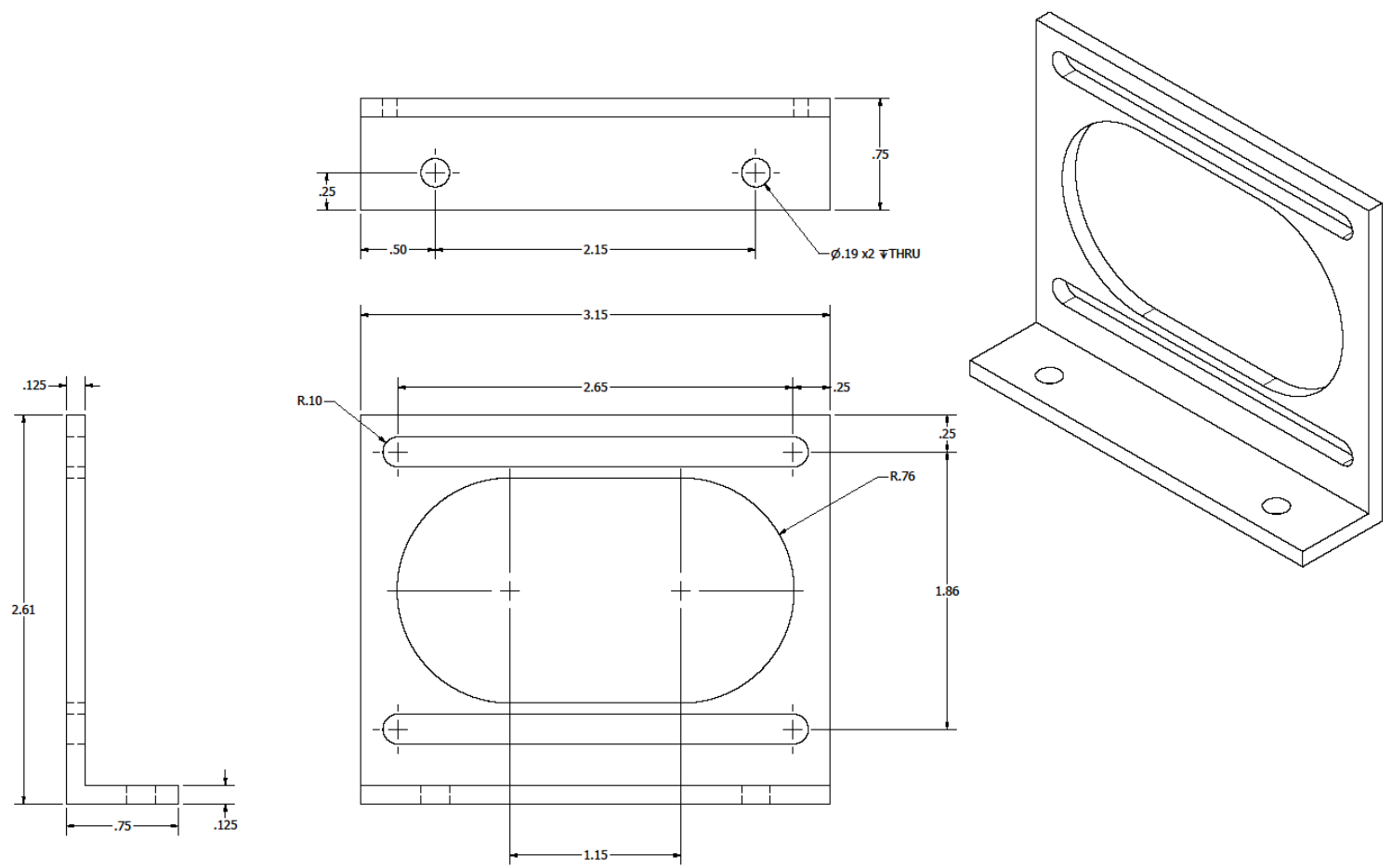

DRAWN Alex Cope	8/17/2012	Virginia Tech Mechanical Engineering
CHECKED		TITLE: Motor Mount - NEMA 23 Quantity: 2
QA		
MFG		
APPROVED		SIZE C / DWG NO Motor Mount - NEMA 23 / REV
		SCALE / SHEET 1 OF 1

Appendix II – MATLAB Code for Scissor Lift Static Solver

```
close all
clear all
clc

%% User Defined Variables

% define working slope in degrees (range is used to
% calculate incine and decline)
angle = -90:1:90;

% set payload (lbs) and weight of scissor lift
P = 5; % lbs (2kg max)
W = .66;

% define lengths (in)
L1 = .75; % length from payload to payload mount joint
l = 8; % length of member

% define working range (height of lift (in))
range = 1.5:.1:7.85;

%% System Solver on level ground

count = 0;
for H = range
count = count+1;

theta = asin(H/l);
L2 = l*cos(theta);

Rcy(count) = L1/L2*P-.5*W;
Ray(count) = .5*W+(L1+L2)/L2*P;

Rby(count) = -Rcy(count);
Rdy(count) = Rby(count)+Rcy(count)-Ray(count);

Rbx(count) = cot(theta)*Ray(count)+cot(theta)*Rby(count);
Rdx(count) = Rbx(count);

% check (all should compute to zero, my be slightly off due to rounding
errors)

Ma(count) = -L1*P+L2/2*W+L2*Rcy(count);

Mc(count) = -L2/2*W+L2*Ray(count)-(L1+L2)*P;

Md(count) = -l*cos(theta)*Rcy(count)-l*cos(theta)*Rby(count);
```

```
Me(count) = -l/2*cos(theta)*Ray(count)-
l/2*cos(theta)*Rby(count)+l/2*sin(theta)*Rbx(count);

end

Ma
Mc
Md
Me

%% Results on level ground

figure
set(gcf,'Color',[1,1,1])
plot(range,Rbx)
     xlabel('Height (in)')
     ylabel('Rbx (lb)')
     title('Results on Level Surface')

figure
set(1,'Color',[1 1 1])
subplot(3,2,1)
    plot(range,Ray)
    xlabel('Height (in)')
    ylabel('Ray (lb)')

subplot(3,2,2)
    plot(range,Rcy)
    xlabel('Height (in)')
    ylabel('Rcy (lb)')

subplot(3,2,3)
    plot(range,Rbx)
    xlabel('Height (in)')
    ylabel('Rbx (lb)')

subplot(3,2,4)
    plot(range,Rby)
    xlabel('Height (in)')
    ylabel('Rby (lb)')

subplot(3,2,5)
    plot(range,Rdx)
    xlabel('Height (in)')
    ylabel('Rdx (lb)')

subplot(3,2,6)
    plot(range,Rdy)
    xlabel('Height (in)')
    ylabel('Rdy (lb)')

%% System Solver for robot on incline/decline
```

```
count2 = 0;
for I = angle
count2 = count2+1;

Py = P*cos(I*pi()/180);
Px = P*sin(I*pi()/180);
Wy = W*cos(I*pi()/180);
Wx = W*sin(I*pi()/180);

    count = 0;
    for H = range
    count = count+1;

    theta = asin(H/l);
    L2 = l*cos(theta);

    Rax = Px+Wx;

    Rcy_slope(count,count2) = L1/L2*Py-.5*Wy;
    Ray_slope(count,count2) = .5*Wy+(L1+L2)/L2*Py;

    Rby_slope(count,count2) = -Rcy_slope(count,count2)-tan(theta)*Rax;
    Rdy_slope(count,count2) =
Rby_slope(count,count2)+Rcy_slope(count,count2)-Ray_slope(count,count2);

    Rbx_slope(count,count2) =
cot(theta)*Ray_slope(count,count2)+cot(theta)*Rby_slope(count,count2)+Rax;
    Rdx_slope(count,count2) = Rbx_slope(count,count2)+Rax;

    end

end

%% Results on sloped surface

figure
set(gcf,'Color',[1,1,1])
surf(angle,range,Rbx_slope)
    xlabel('Angle (deg)')
    ylabel('Height (in)')
    zlabel('Rbx (lb)')
    title('Results on Incline')

figure
set(gcf,'Color',[1,1,1])
subplot(3,2,1)
    surf(angle,range,Ray_slope)
    xlabel('Angle (deg)')
    ylabel('Height (in)')
    zlabel('Ray (lb)')
subplot(3,2,2)
    surf(angle,range,Rcy_slope)
    xlabel('Angle (deg)')
    ylabel('Height (in)')
```

```
    zlabel('Rcy (lb)')

subplot(3,2,3)
    surf(angle,range,Rbx_slope)
    xlabel('Angle (deg)')
    ylabel('Height (in)')
    zlabel('Rbx (lb)')

subplot(3,2,4)
    surf(angle,range,Rby_slope)
    xlabel('Angle (deg)')
    ylabel('Height (in)')
    zlabel('Rby (lb)')

subplot(3,2,5)
    surf(angle,range,Rdx_slope)
    xlabel('Angle (deg)')
    ylabel('Height (in)')
    zlabel('Rdx (lb)')

subplot(3,2,6)
    surf(angle,range,Rdy_slope)
    xlabel('Angle (deg)')
    ylabel('Height (in)')
    zlabel('Rdy (lb)')

figure
set(gcf,'Color',[1,1,1])
plot(angle,max(Rbx_slope))
     xlabel('Slope (deg)')
     ylabel('Rbx (lb)')
     title('Max Horizontal Loads on Lead Screw Nut')

Rbx_max_slope = max(max(Rbx_slope))
```

Appendix III – Scissor Lift Vibration Analysis

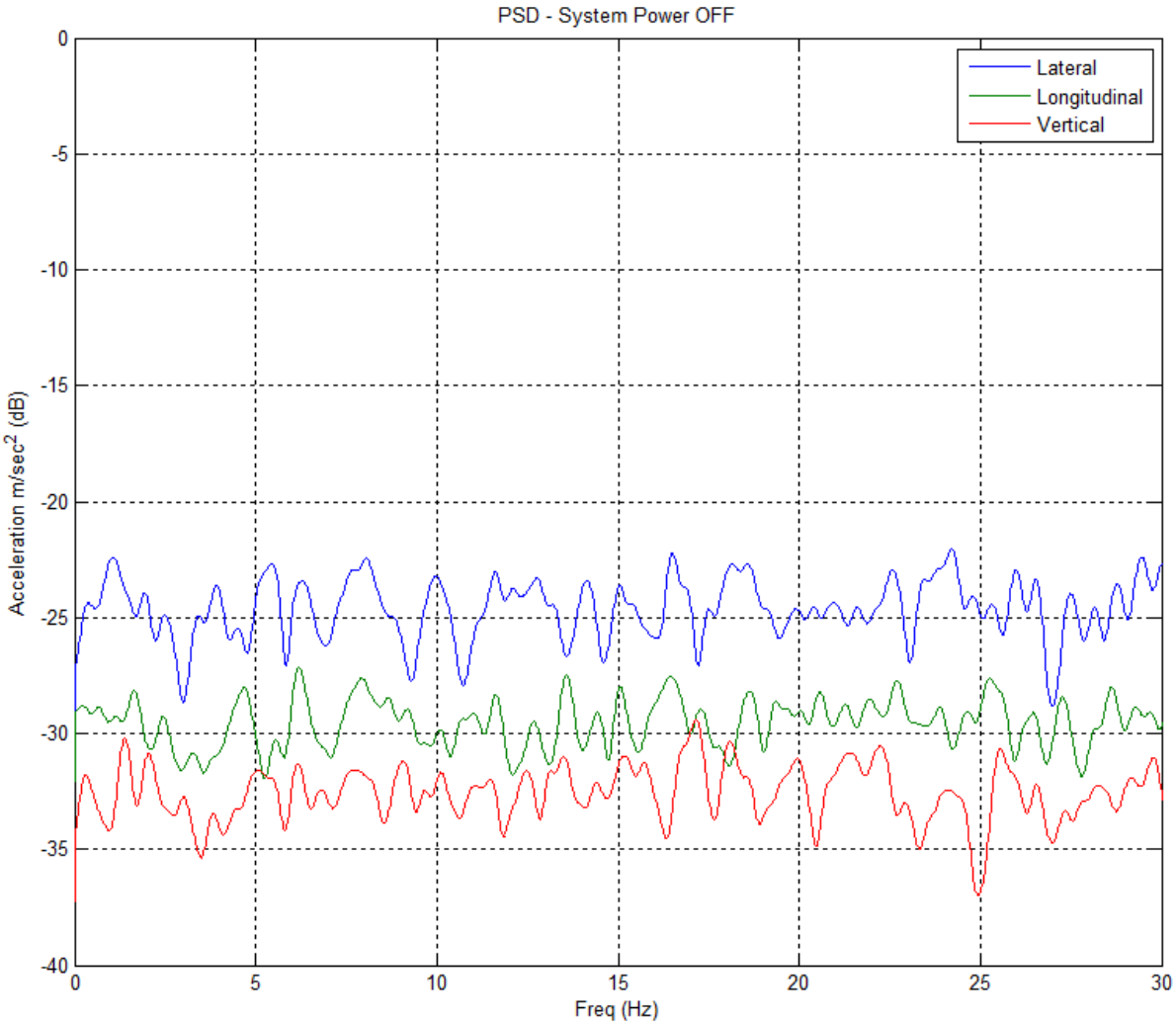

Inspection tool was stationary with no power supplied.

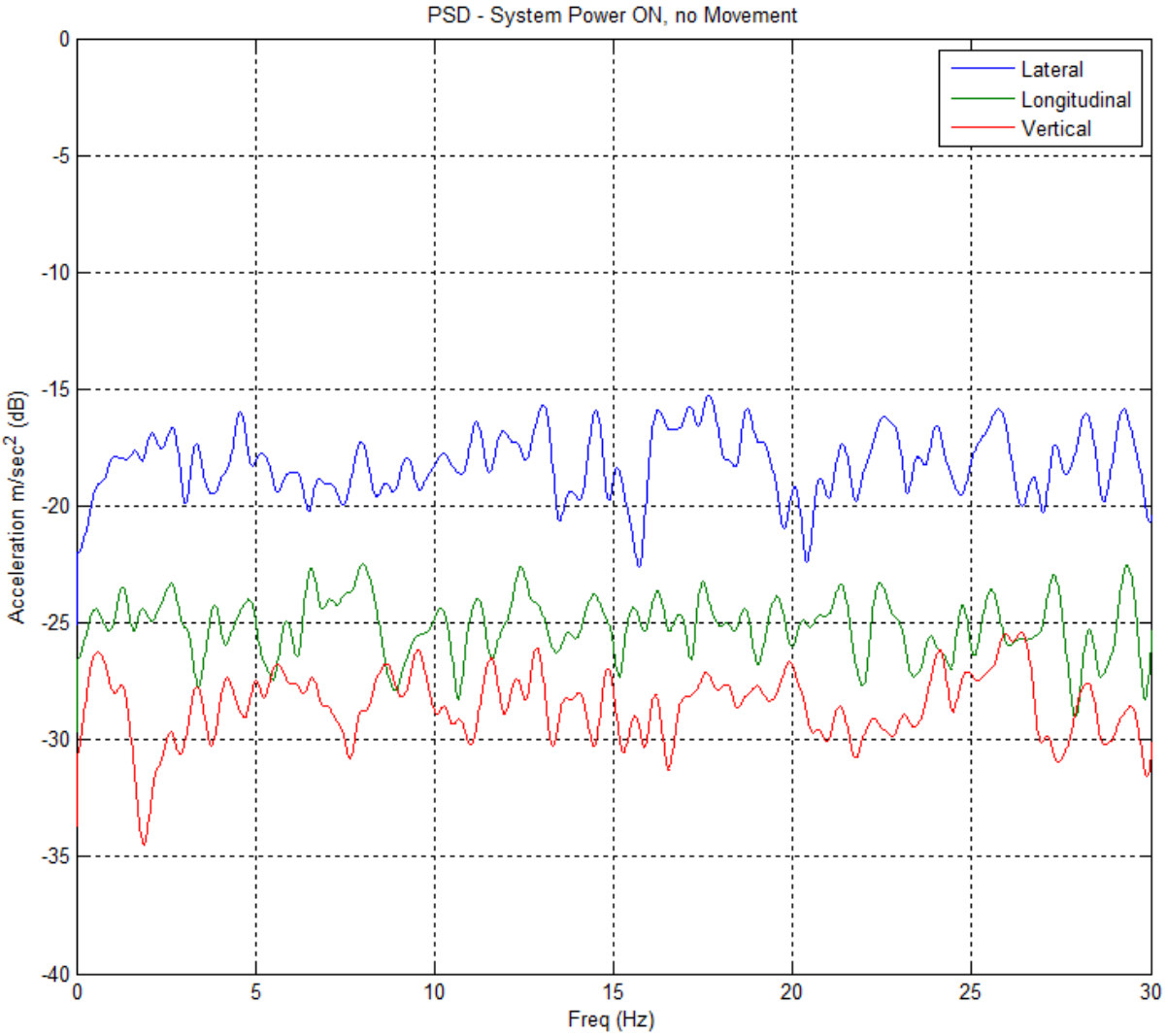

System power was on including all electronics (cameras, LIDAR, DC-DC converter, switch, PoE Injector, AXIS Video Encoder, fans, etc.) as well as power to the motors. Inspection tool was stationary with no motion.

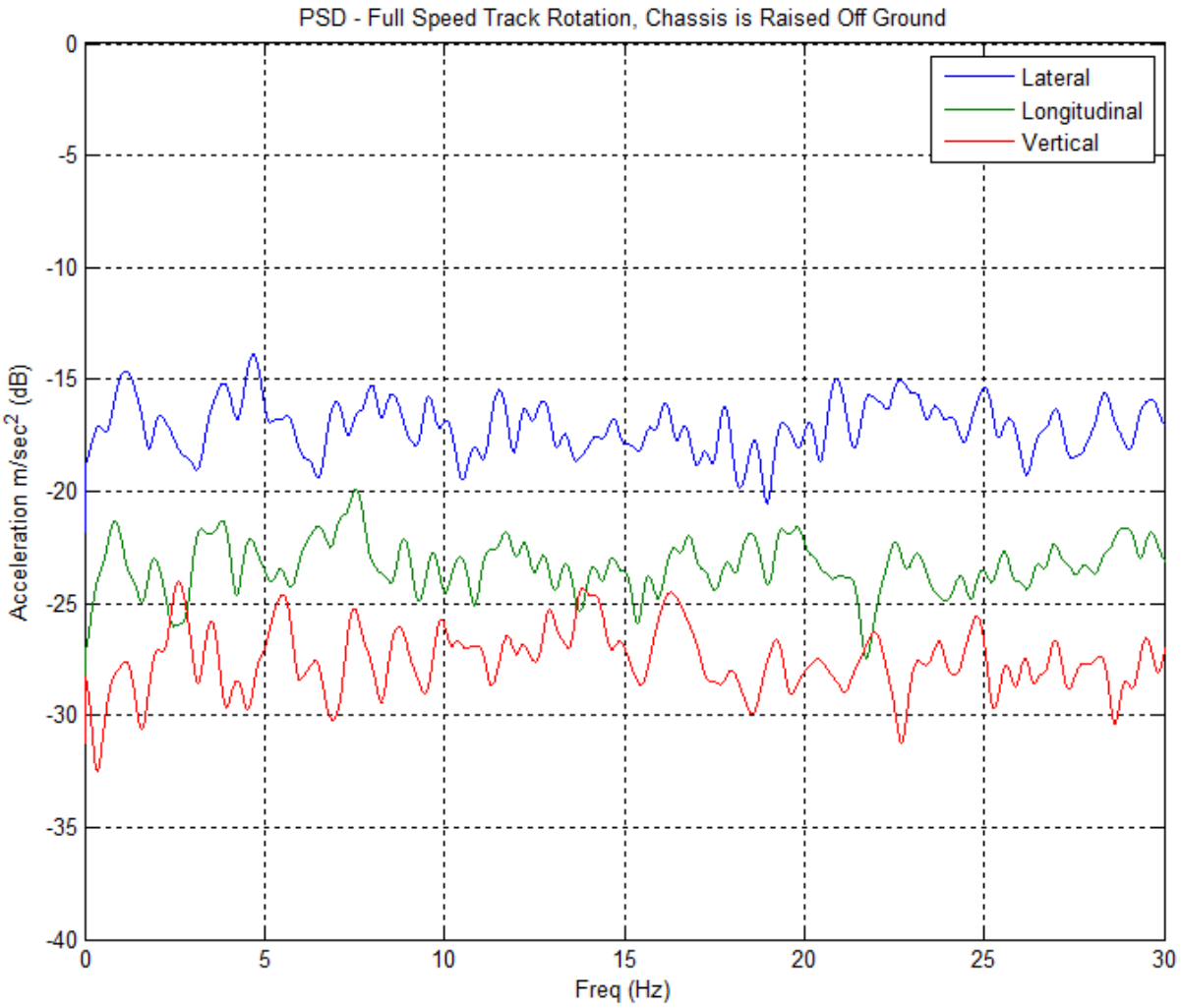

Inspection tool was fully powered and suspended on a rigid foam block which raised the tracks off the ground allowing for track rotation with no motion.

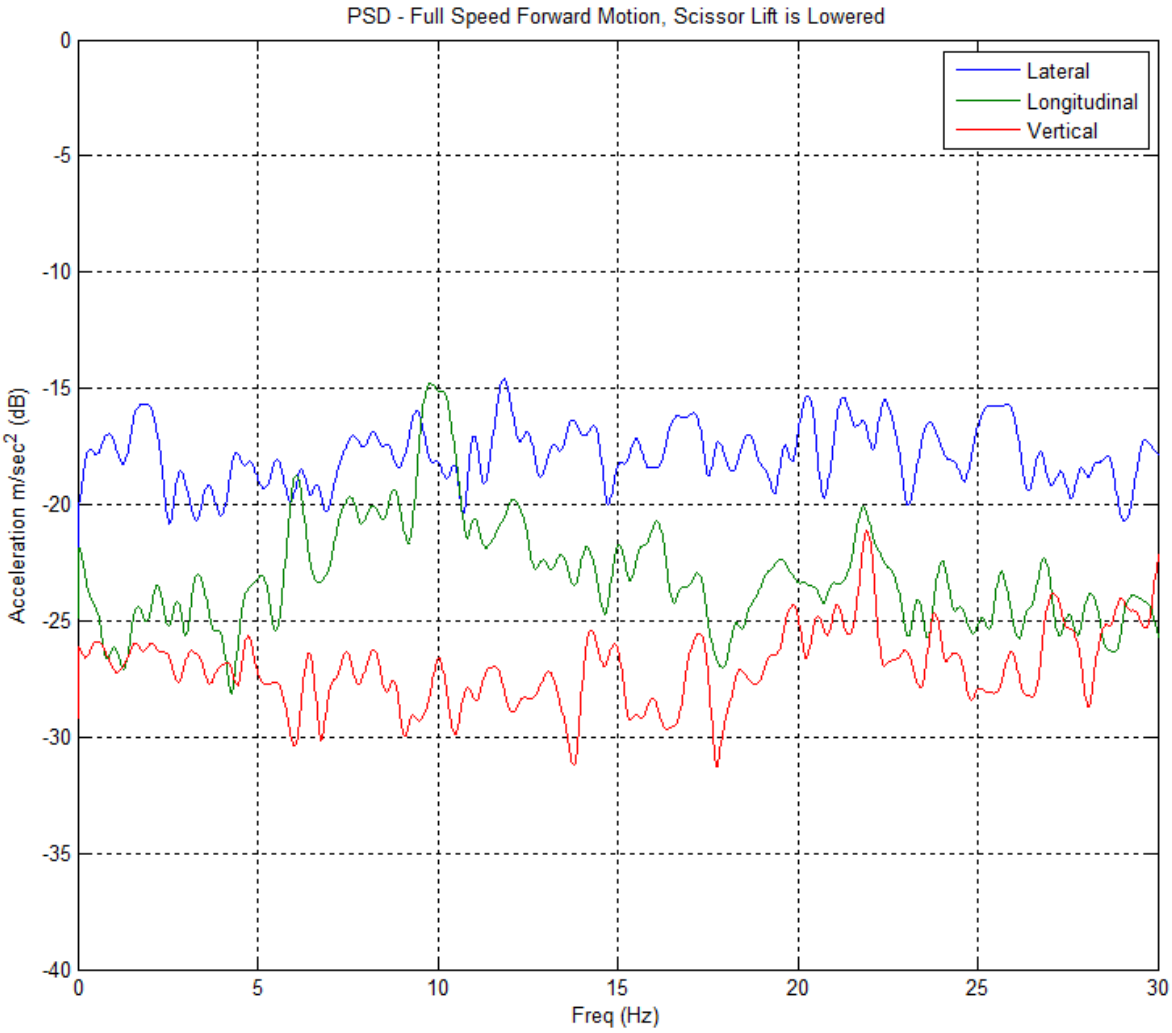

Inspection tool was driven forward at full operational speed on level ground. Ground surface was a smooth portland cement and the scissor lift was fully collapsed.

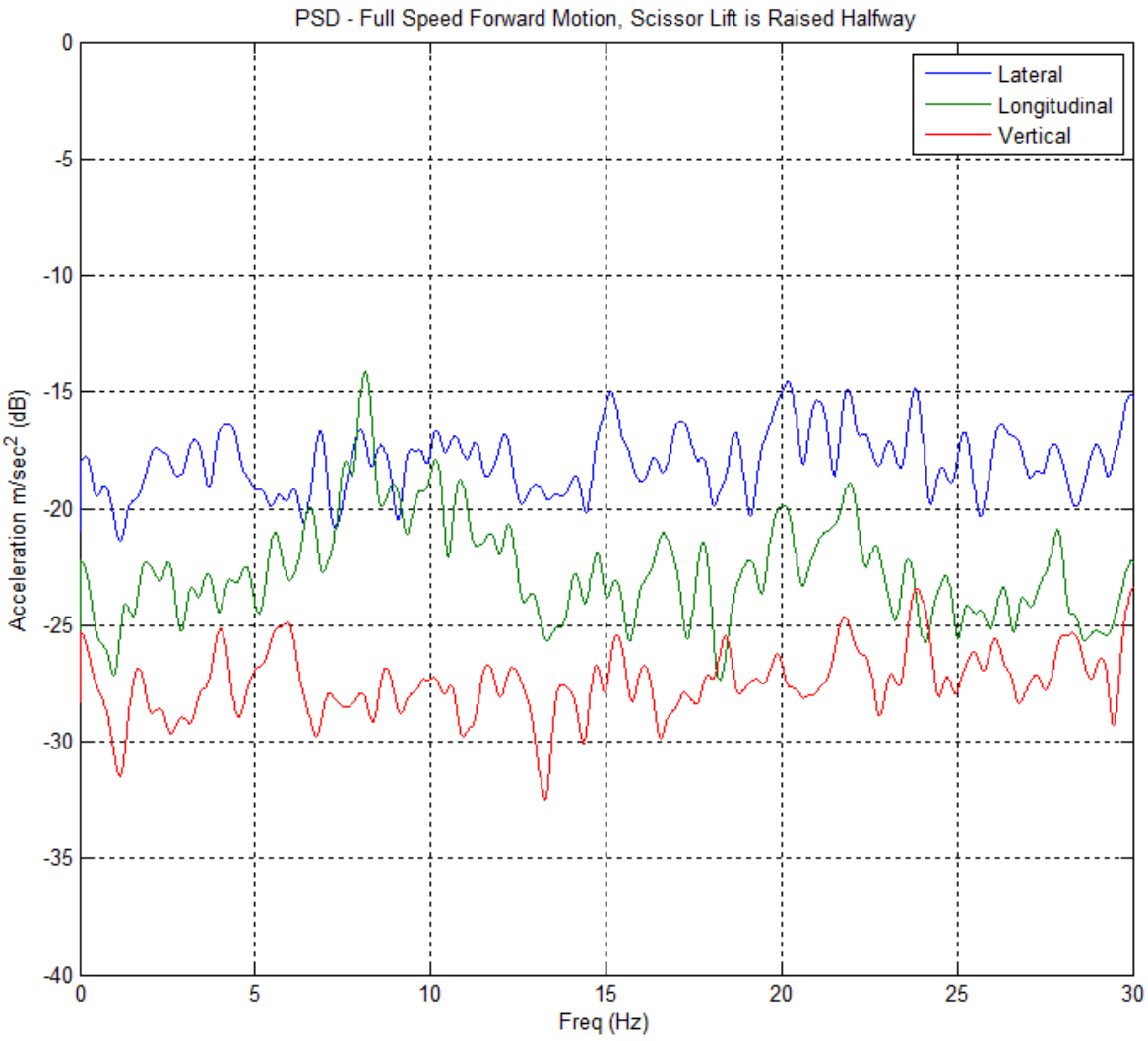

Inspection tool was driven forward at full operational speed on level ground. Ground surface was a smooth portland cement and the scissor lift was partially collapsed.

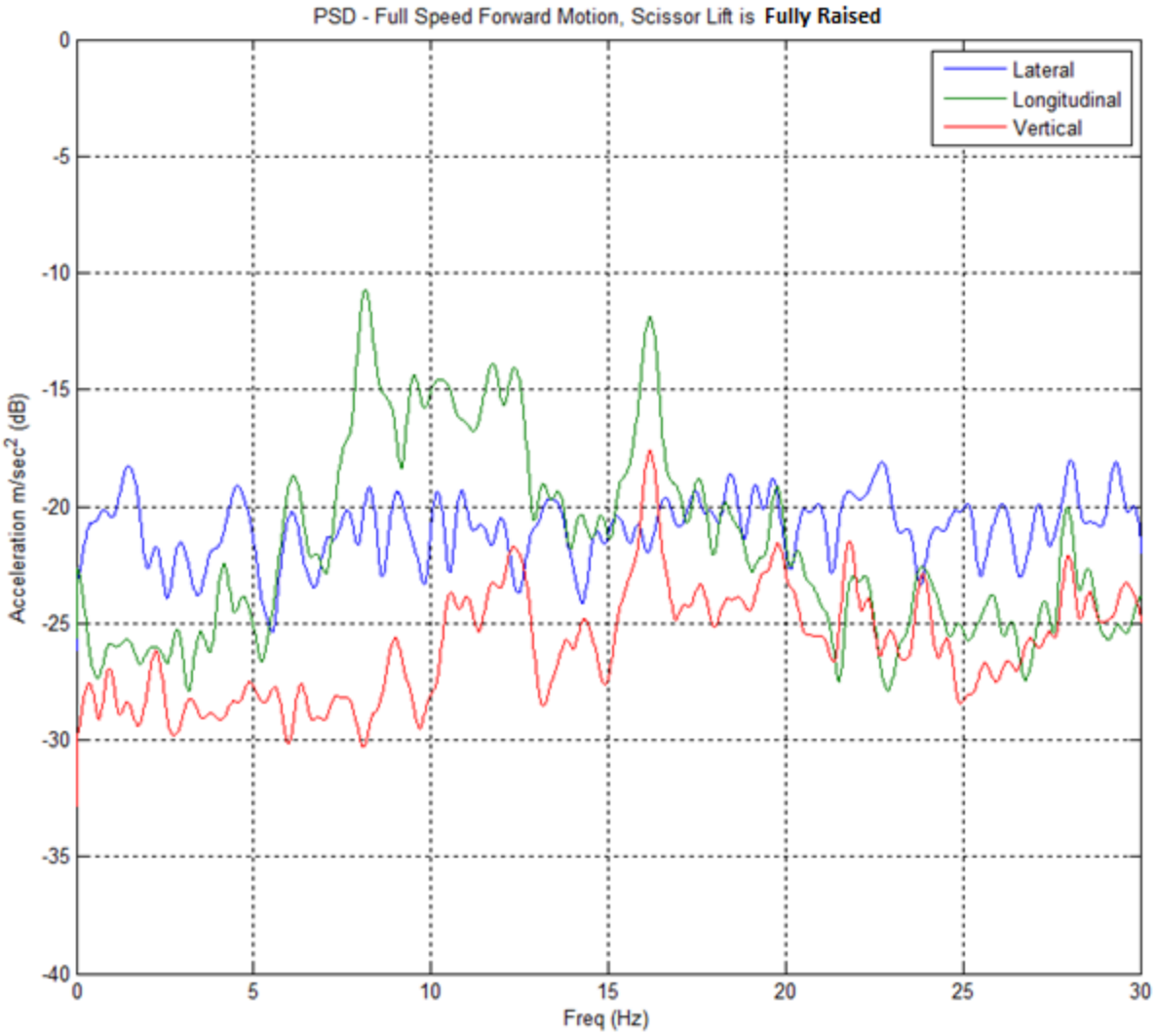

Inspection tool was driven forward at full operational speed on level ground. Ground surface was a smooth portland cement and the scissor lift was fully raised.

Appendix IV – Associated Data Sheets

DATASHEET

AXIS M7001 Video Encoder and Covert Surveillance Kit

The smallest video encoder with H.264.

- > Compact and cost-effective
- > Full frame rate in all resolutions
- > Simultaneous H.264 and Motion JPEG
- > PTZ support
- > Power over Ethernet

The one-channel AXIS M7001 Video Encoder offers a highly compact design with superb H.264 performance, providing an easy and cost-effective solution for integrating small or large numbers of analog CCTV cameras into an IP-based video surveillance system.

The palm-sized, standalone AXIS M7001 is designed for installation close to an analog camera. It supports all types of analog cameras including PTZ (pan/tilt/zoom) and PTZ domes.

AXIS M7001 is perfect for small and large analog video installations, especially where an IP network infrastructure is already in place. Its small size also makes it ideal for use in discreet surveillance applications, for example, in retail stores and banks, and in camera housings.

AXIS M7001 can deliver two simultaneous video streams, one in H.264 and another in Motion JPEG, at full frame rate in all resolutions up to D1 (720x480 in NTSC, 720x576 in PAL).

The H.264 video compression format drastically reduces bandwidth and storage requirements without compromising image quality. Motion JPEG is supported for increased flexibility. The video encoder also provides video motion detection.

AXIS M7001 is powered over Ethernet using the same cable as for data transmission, which simplifies installation. The video encoder can, in turn, feed power to the small covert camera that is included in the AXIS M7001 Covert Surveillance Kit.

Overview

GE Security's MS-PoE is a Power over Ethernet Injector that inserts 802.3af PoE into Cat.5 cable, allowing the cable between the injector and splitter to transfer data and power simultaneously. With the MS-PoE installed, the system administrator only has to use a single RJ-45 Ethernet cable to carry both power and data to each device. The MS-PoE also reduces costs and facilitates networking planning while delivering higher reliability.

Standard Features

- Complies with IEEE 802.3af Power over Ethernet, IEEE 802.3/802.3u 10/100Base-TX
- Provides DC 48V power over RJ-45 Ethernet cable to device with Ethernet port
- LED indicators for power input
- Distance up to 100 meters
- Auto-detect of PoE IEEE 802.3af equipment protects devices from being damaged by incorrect installation
- Works with EIA568, category 5, 4-pair cables for 10Base-T or 100Base-TX
- EMI standards comply with FCC, CE class B
- Convenient plug-and-play installation saves time and reduces installation costs

MS-PoE IEEE 802.3af Power over Ethernet Injector

MS-POE

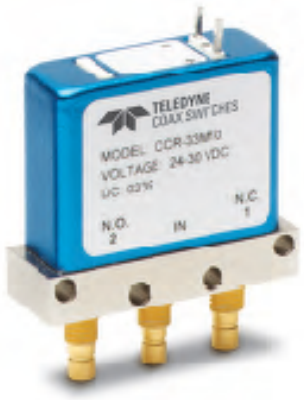

Commercial CCR-33M

75 Ohm DC-3GHz SPDT Switch

Latching

The CCR-33M switch is the first of its series, expanding our product line to include 75-Ohm designs. This SPDT is designed for optimum performance in 75-Ohm applications switching signals from a common input to either of two outputs. The characteristic impedance is 75 Ohms. The switches are small with connector spacing compatible with mini-SMB connectors.

The CCR-33M series switch is offered with either a failsafe or latching actuator. This design is compatible with the two most common mounting hole patterns.

Specifications

RF Contacts:	Break before make
Actuator	Voltage (VDC) 20°C: 12 / 15 / 28 — Current (mA): 140 / 115 / 65
Switching Time:	10 msec max
Connectors:	mini-SMB 75 Ohm Jack. In accordance with IEC 169-10, CECC 22 130, US MIL-C-39012
Weight:	1.65 oz. max
Temperature Range:	-40° C to +65° C (Operating)
Shock:	MIL-STD-202 Method 213, Condition D (500G Non Operating)
Vibration:	MIL-STD-202 Method 214, Condition D (10G RMS Non Operating)
Humidity:	Moisture Seal Available
MTBF:	7.3 Million Hours (MIL-HDBK-217F Fixed, 25° C, <1 Cycle per hour)

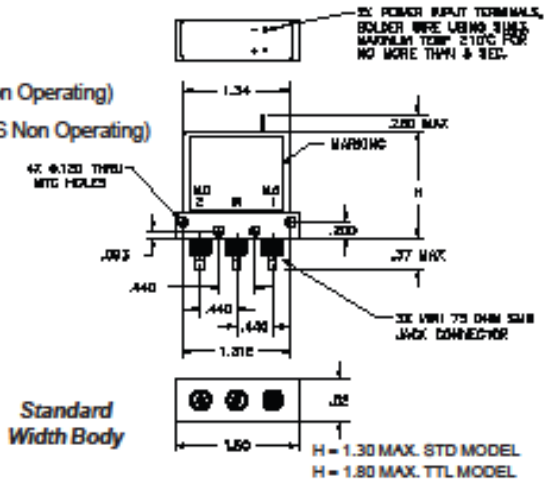

Standard Width Body

Specifications	DC-1 GHz	1-3 GHz
VSWR (max)	1.20:1	1.30:1
Insertion Loss (min)	0.20 dB	0.30 dB
Isolation (max)	80.0 dB	70.0 dB

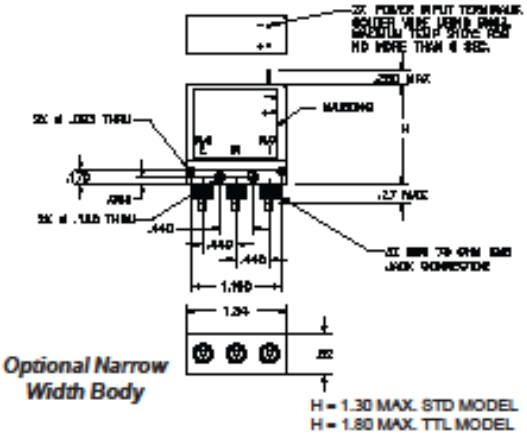

Optional Narrow Width Body

TELEDYNE COAX SWITCHES

IM Relay

- **Slim line 10x6mm, low profile 5.65mm and min. board-space 60mm²**
- **Switching current 2/5A, switching power 60W/62.5VA and switching voltage 220VDC/250VAC**
- **Low coil power consumption, 140mW standard, 100mW for high sensitive version, 50mW for ultra high sensitive version and 100mW for bistable version**
- **High dielectric and surge capability up to 2500Vrms between open contacts and 3000Vrms between coil and contacts**
- **High mechanical shock resistance up to 300g functional**

Typical applications
Telecommunication, access and transmission equipment, optical network terminals, modems, office and business equipment, consumer electronics, measurement and test equipment, industrial control, medical equipment, automotive applications

Approvals

UL 508 File No. E 111441
Technical data of approved types on request

Contact Data	standard, C standard and high dielectric version	D high current version	P high contact stability version
Contact arrangement	2 form C, 2 CO		
Max. switching voltage	220VDC, 250VAC	220VDC, 250VAC	220VDC, 250VAC
Rated current	2A	5A	2A
Limiting continuous current	2A	5A	2A
Switching power	60W, 62.5VA		
Contact material	PdRu +Au covered	AgNi +Au covered	PdRu +Au covered
Contact style	twin contacts		
Minimum switching voltage	100µV		
Initial contact resistance	<50mΩ at 10mA/20mV		
Thermoelectric potential	<10µV		
Operate time	typ. 1ms, max. 3ms		
Release time			
without diode in parallel	typ. 1ms, max. 3ms		
with diode in parallel	typ. 3ms, max. 5ms		
Bounce time max.	typ. 1ms, max. 5ms		

Max. DC load breaking capacity

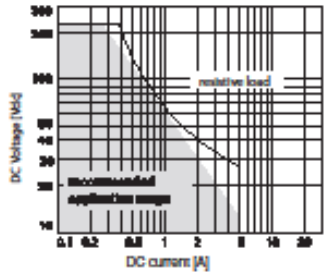

Contact Data (continued)

Electrical endurance	
at contact application 0 (≤30mW/≤10mA)	min. 2.5x10⁶ operations
cable load open end	min. 2.0x10⁶ operations
resistive, 125VDC / 0.24A - 30W	min. 5x10⁵ operations
resistive, 220 VDC / 0.27A - 60W	min. 1x10⁵ operations
resistive, 250VAC / 0.25A - 62.5VA	min. 1x10⁵ operations
resistive, 30VDC / 1A - 30W	min. 5x10⁵ operations
resistive, 30VDC / 2A - 60W	min. 1x10⁵ operations
Contact ratings, UL	220VDC, 0.24A, 60W 125VDC, 0.24A, 30W 250VAC, 0.25A, 62.5VA 125VAC, 0.5A, 62.5VA 30VDC, 2A, 60W
Mechanical endurance	10⁸ operations

Coil Data

Magnetic system	monostable, bistable
Coil voltage range	1.5 to 24VDC

Coil versions, standard version, monostable, 1 coil

Coil code	Rated voltage VDC	Operate voltage VDC	Release voltage VDC	Coil resistance Ω±10%	Rated coil power mW
00	1.5	1.13	0.15	16	140
08	2.4	1.80	0.24	41	140
01	3	2.25	0.30	64	140
02	4.5	3.38	0.45	145	140
03	5	3.75	0.50	178	140
04	6	4.50	0.60	257	140
05	9	6.75	0.90	579	140
06	12	9.00	1.20	1029	140
07	24	18.00	2.40	2880	200

All figures are given for coil without pre-energization, at ambient temperature +23°C

Coil operating range, standard version

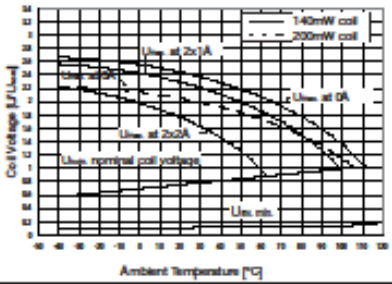

EM-500 Series

Indoor Color Micro Metal Case Camera

Features

- Super High Resolution of 550 TVL
- Choice of 3.7mm Conical Pinhole Lens, 3.7mm Flat Pinhole Lens, 4.3mm Super Cone Pinhole Lens
- Mounting bracket allows wide range of mounting flexibility
- Mini Metal Case for covert use or very discreet surveillance

Specifications

Part Number	EM-500 Series
Pickup Device	1/3" Sony ICX638 CCD
Video Format	NTSC or PAL
Picture Elements	768 x 494 (NTSC) I 768 x 494 (NTSC)
Effective Pixels (NTSC I PAL)	813 (H) x 508 (V) 410K I
Scanning System	2:1 Interlace
Scanning Frequency	H: 15.734 KHz, V: 59.94 Hz I
Horizontal Resolution	550 TVL
Sensitivity	0.2 Lux / F=2.0 (30 IRE)
S/N Ratio	Over 48dB (AGC off)
Electronic Shutter	1/60s~1/100,000s
Video Output	BNC 1.0Vp-p 75Ω
Gamma Correction	0.45
Lens Type	3.7mm Pinhole Lens
Lens Options	Conical Pinhole Lens
BLC	Auto
Gain Control	Auto
Sync Mode	Internal Sync
Environmental	Indoor Applications
Power Source	12VDC
Power Consumption	3.5W max
Operating Temp	14°F~113°F I -10°C~45°C
Dimensions (in I mm)	1" W x 1" H I 25 x 25mm
Weight (lbs I gm)	0.07lbs I 32g
Certifications	CE/FCC

Dimensions: mm/in

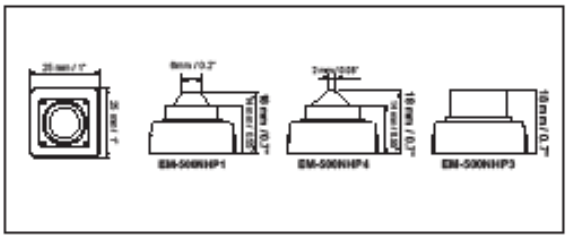

Ordering Info

EM-500HP1: Color Micro Metal Camera, 550 TVL, 3.7mm Conical Pinhole
EM-500HP3: Color Micro Metal Camera, 550 TVL, 3.7mm Flat Pinhole
EM-500HP3: Color Micro Metal Camera, 550 TVL, 4.3mm Super Cone Pinhole

MPS Series
Magnetic Proximity Sensors

Features/Benefits
- *Long life—4M operations*
- *Sealed contacts*
- *Quality construction*
- *Quick and easy installation*

Typical Applications
- *Automotive sensors and indicators*
- *Industrial sensors*
- *Factory automation equipment*

Specifications

CONTACT RATINGS: 3.0 W max. @ 30 V DC or 30 V AC max. @ 0.3 AMP max.; 1.0 msec. max. operate time (including bounce); 1.0 AMP max. carry current.

CONTACT RESISTANCE: 100 m Ω max. initial.

DIELECTRIC STRENGTH: 200 V DC min.

ELECTRICAL CIRCUIT: SPST NO (Contact Form A). Reed switch opens when magnet is removed from proximity. Contacts are held closed when magnet is within actuation range.

OPERATING TEMPERATURE: -40°F to 212°F (-40°C to 100°C).

OPERATING DISTANCE/ALIGNMENT: Operate (pull-in or make) points are nominal values with ± 10% tolerance. Release points are 110% to 150% of the operating points.

MECHANICAL & ELECTRICAL LIFE: 4 million operations.

PACKAGING: Bulk packaging, 10 switch and magnet pairs per package.

Materials

HOUSING/SPACER/COVER: ABS plastic (UL94V-0), white.

REED SWITCH: Rhodium coated reed contacts in hermetically sealed, nitrogen filled glass capsule. Closed when magnet is in close proximity. Used in closed loop circuits.

WIRE LEADS: UL 1061, 22 AWG wire: stranded, made of copper or aluminum; Length: 12 in. with ends stripped; Color: white.

POTTING (around wires): Epoxy.

MAGNETS: MPS45WGW: NdFeB
MPS80WGW: Ceramic Ferrite 8
All other models: Alnico V

ADHESIVE MOUNTING: Foam-backed, pressure-sensitive adhesive with release liner (MPS45WGW model only).

NOTE: Specifications and materials listed above are for switches with standard options. For information on specific and custom switches, consult Customer Service Center.

How To Order

Complete part numbers for MPS Series Magnetic Proximity Sensors are shown on pages E-35 thru E-39.

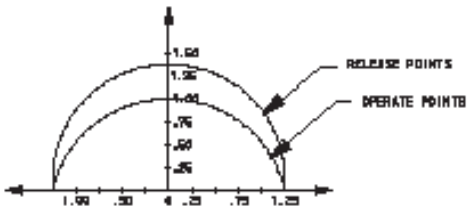

OFFSET OF CENTERLINES AND DISTANCE BETWEEN FACES OF SWITCH AND MAGNET (INCHES).

ACTUATION CHART

NOTE: UL 61058-2 Rating

PART NUMBER	SWITCH TYPE
MPS45WGW	Subminiature surface mount (adhesive or flange), side exit leads, 1" make gap.

UL 61058-2

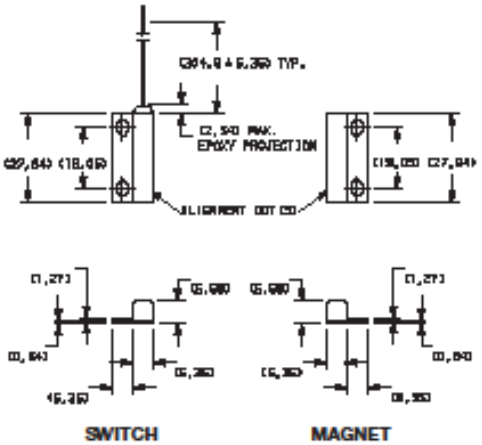

Third Angle Projection

Dimensions are shown: mm
Specifications and dimensions subject to change

Mini-Rail® Miniature Linear Guides
Product Overview

PRODUCT OVERVIEW

An economical alternative to conventional miniature linear guides, Mini-Rail requires no maintenance, is fully interchangeable with industry standard sizes and is maintained in stock for quick delivery.

Mini-Rail miniature linear guides are available in five sizes: 7, 9, 12, 15 and 20mm - in lengths up to 3600mm, meaning no cumbersome butt joints. These guides are precision manufactured out of lightweight aluminum alloys to ensure long life and corrosion resistance.

- No rolling elements
- Self-lubricating Frelon GOLD® Liner
- Withstands vibration and shock
- Corrosion-resistant - ideal in harsh environments
- Ceramic coated, aluminum rail
- Compact design- small footprint

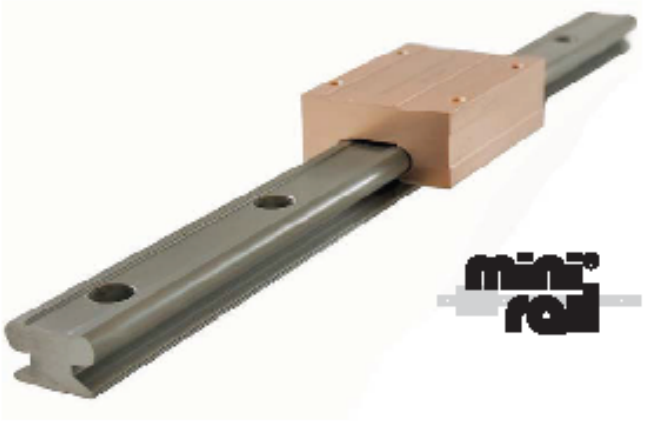

CARRIAGE CONFIGURATIONS

Precision Series: Ceramic coated rails and carriages are corrosion resistant. Frelon GOLD® self-lubricating liner delivers the best overall performance, the highest loads, the best wear life, and speeds. Most precise running clearance for high precision applications.

Compensated Precision Series: Same as Precision Series except with additional clearance provided to tolerate misalignment.

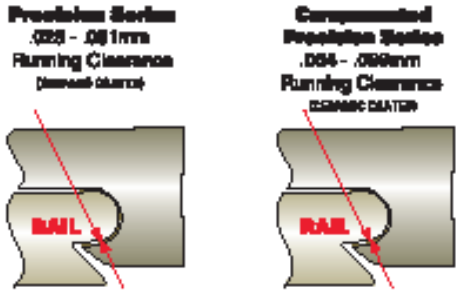

Frelon GOLD® and Frelon® J are Teflon® based materials that are truly self-lubricating. Frelon® materials are bonded to the carriage creating a one-piece unit.

APPLICATIONS

- Medical Precision
- Food Processing
- Automation
- Electronics
- Mobile Home Components
- Packaging
- Product Movement
- Printing
- Semi-conductor

ORDERING INFORMATION

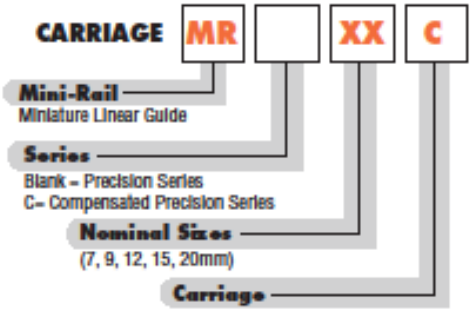

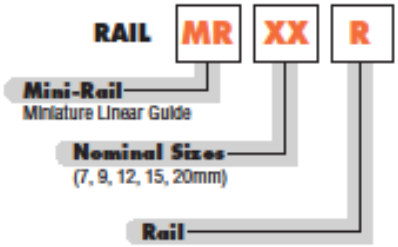

EXAMPLE: MRC20C
MR20R

See following page for Mini-Rail full assembly ordering.

Data Sheet
48V Input Mini Family
DC-DC Converter Module

Features
- DC input range: 36 - 75 V
- Isolated output
- Input surge withstand: 100 V for 100 ms
- DC output: 2 – 48 V
- Programmable output: 10 to 110%
- Regulation: ±0.2% no load to full load
- Efficiency: Up to 90%
- Maximum operating temp: 100 °C, full load
- Power density: up to 100 W per cubic inch
- Height above board: 0.43 in. (10,9 mm)
- Parallelable, with N+M fault tolerance
- Low noise ZCS/ZVS architecture
- RoHS Compliant (with F or G pin option)

Shown actual size:
2.28 x 2.2 x 0.5 in
57,9 x 55,9 x 12,7 mm

Product Overview
These DC-DC converter modules use advanced power processing, control and packaging technologies to provide the performance, flexibility, reliability and cost effectiveness of a mature power component. High frequency ZCS/ZVS switching provides high power density with low noise and high efficiency.

Applications
Distributed power, medical, ATE, communications, defense, aerospace

For details on proper operation please refer to the Design Guide & Applications Manual for Maxi, Mini, Micro Family.

Absolute Maximum Ratings

Parameter	Rating	Unit	Notes
+In to –In voltage	-0.5 to +105	Vdc	
PC to –In voltage	-0.5 to +7.0	Vdc	
PR to –In voltage	-0.5 to +7.0	Vdc	
SC to –Out voltage	-0.5 to +1.5	Vdc	
–Sense to –Out voltage	1.0	Vdc	
Isolation voltage			
in to out	3000	Vrms	Test voltage
in to base	1500	Vrms	Test voltage
out to base	500	Vrms	Test voltage
Operating Temperature	-55 to +100	°C	M-Grade
Storage Temperature	-65 to +125	°C	M-Grade
Pin soldering temperature	500 (260)	°F (°C)	<5 sec; wave solder
	750 (390)	°F (°C)	<7 sec; hand solder
Mounting torque	5 (0.57)	in-lbs (N-m)	6 each

Part Numbering
e.g. V48B12T250BL2

V48B □ □ □ **B** □ □

Output Voltage
2 = 2 V
3V3 = 3.3 V
5 = 5 V
12 = 12 V
15 = 15 V
24 = 24 V
28 = 28 V
36 = 36 V
48 = 48 V

Product Grade Temperatures (°C)

Grade		Operating	Storage
E	=	-10 to +100	-20 to +125
C	=	-20 to +100	-40 to +125
T	=	-40 to +100	-40 to +125
H	=	-40 to +100	-55 to +125
M	=	-55 to +100	-65 to +125

Output Power

Vout	Pout
2 V	100 W
3.3 V	150 W
5 V	200W
12 V	250 W
15 V	250 W
24 V	250 W
28 V	250 W
36 V	250 W
48 V	250 W, 300 W

Pin Style / Finish
Blank: Short — Tin/Lead
L: Long — Tin/Lead
S: Short ModuMate — Gold
N: Long ModuMate — Gold
F: Short RoHS — Gold
G: Long RoHS — Gold

Baseplate
Blank: Slotted
2: Threaded
3: Through-hole

■ Features :

- Universal AC input / Full range
- AC input active surge current limiting
- Built-in 5V/0.5A auxiliary power
- Built-in active PFC function, PF>0.95
- Protections: Short circuit / Overload / Over voltage / Over temperature
- Output voltage can be trimmed between 40 ~ 110% of the rated output voltage
- Forced air cooling by built-in DC fan
- High power density 10.7w/inch³
- 1U low profile 41mm
- Active current sharing up to 4000W(3+1) (Note.8)
- DC OK Signal
- Built-in remote ON-OFF control
- Built-in remote sense function
- 3 years warranty

SPECIFICATION

MODEL		RSP-1000-12	RSP-1000-15	RSP-1000-24	RSP-1000-27	RSP-1000-48
OUTPUT	DC VOLTAGE	12V	15V	24V	27V	48V
	RATED CURRENT	60A	50A	40A	37A	21A
	CURRENT RANGE	0 ~ 60A	0 ~ 50A	0 ~ 40A	0 ~ 37A	0 ~ 21A
	RATED POWER	720W	750W	960W	999W	1008W
	RIPPLE & NOISE (max.) Note.2	150mVp-p	150mVp-p	150mVp-p	150mVp-p	150mVp-p
	VOLTAGE ADJ. RANGE	10 ~ 13.5V	13.5 ~ 16.5V	20 ~ 26.4V	24 ~ 30V	43 ~ 55V
	VOLTAGE TOLERANCE Note.3	±1.0%	±1.0%	±1.0%	±1.0%	±1.0%
	LINE REGULATION	±0.5%	±0.5%	±0.5%	±0.5%	±0.5%
	LOAD REGULATION	±0.5%	±0.5%	±0.5%	±0.5%	±0.5%
	SETUP, RISE TIME	300ms, 50ms at full load				
	HOLD UP TIME (Typ.)	16ms/230VAC 16ms/115VAC at full load				
INPUT	VOLTAGE RANGE Note.5	90 ~ 264VAC 127 ~ 370VDC				
	FREQUENCY RANGE	47 ~ 63Hz				
	POWER FACTOR (Typ.)	0.95/230VAC 0.98/115VAC at full load				
	EFFICIENCY (Typ.)	83%	85%	88%	88%	90%
	AC CURRENT (Typ.)	12A/115VAC 6A/230VAC				
	INRUSH CURRENT (Typ.)	25A/115VAC 40A/230VAC				
	LEAKAGE CURRENT	<2.0mA / 240VAC				
PROTECTION	OVERLOAD	105 ~ 125% rated output power				
		Protection type : Constant current limiting, recovers automatically after fault condition is removed				
	OVER VOLTAGE	13.8 ~ 16.8V	17 ~ 20.5V	27.6 ~ 32.4V	31 ~ 36.5V	56.6 ~ 66.2V
		Protection type : Shut down o/p voltage, re-power on to recover				
	OVER TEMPERATURE	85℃±5℃ (TSW2) detect on heatsink of O/P diode; 75℃±5℃ (TSW1) detect on heatsink of power transistor				
		Protection type : Shut down o/p voltage, recovers automatically after temperature goes down				
FUNCTION	AUXILIARY POWER(AUX)	5V @ 0.5A (+5%, -8%)				
	REMOTE ON/OFF CONTROL Note.6	Power on : short between on/off(pin6) & -S(pin2) on CN50 Power off : open between on/off(pin6) & -S(pin2) on CN50				
	DC OK SIGNAL	The TTL signal out, PSU turn on = 3.3 ~ 5.6V ; PSU turn off = 0 ~ 1V				
	OUTPUT VOLTAGE TRIM Note.6	Adjustment of output voltage is possible between 40 ~ 110% of rated output				
	CURRENT SHARING(CS)Note.7	Please refer to function manual				
ENVIRONMENT	WORKING TEMP.	-20 ~ +60℃ (Refer to output load derating curve)				
	WORKING HUMIDITY	20 ~ 90% RH non-condensing				
	STORAGE TEMP., HUMIDITY	-40 ~ +85℃, 10 ~ 95% RH				
	TEMP. COEFFICIENT	±0.02%/℃ (0 ~ 50℃)				
	VIBRATION	10 ~ 500Hz, 2G 10min./1cycle, 60min. each along X, Y, Z axes				
SAFETY & EMC (Note.4)	SAFETY STANDARDS	UL60950-1, TUV EN60950-1 approved				
	WITHSTAND VOLTAGE	I/P-O/P:3KVAC I/P-FG:1.5KVAC O/P-FG:0.5KVAC				
	ISOLATION RESISTANCE	I/P-O/P, I/P-FG, O/P-FG:100M Ohms/500VDC				
	EMI CONDUCTION & RADIATION	Compliance to EN55022 (CISPR22)				
	HARMONIC CURRENT	Compliance to EN61000-3-2,-3				
	EMS IMMUNITY	Compliance to EN61000-4-2,3,4,5,6,8,11; ENV50204, EN55024, EN61000-6-2, EN61204-3, heavy industry level, criteria A				
OTHERS	MTBF	35K hrs min. MIL-HDBK-217F (25℃)				
	DIMENSION	295*127*41mm (L*W*H)				
	PACKING	1.9Kg; 6pcs/12.7Kg/0.99CUFT				

NOTE

1. All parameters NOT specially mentioned are measured at 230VAC input, rated load and 25℃ of ambient temperature.
2. Ripple & noise are measured at 20MHz of bandwidth by using a 12" twisted pair-wire terminated with a 0.1uf & 47uf parallel capacitor.
3. Tolerance : includes set up tolerance, line regulation and load regulation.
4. The power supply is considered a component which will be installed into a final equipment. The final equipment must be re-confirmed that it still meets EMC directives.
5. Derating may be needed under low input voltages. Please check the derating curve for more details.
6. The power supply unit will have no output if the shorting connector is not assembled. It contains two shorting wires: one is from on/off(pin6) to -s(pin2) and the other is from Vcc(pin8) to Vcc(pin10). Please refer to function manual for details.
7. In parallel connection, maybe only one unit operate if the total output load is less than 5% of rated load condition.
8. Please consult MEAN WELL for applications of more units connecting in parallel.

Sure step® Stepping System Motors

Stepping Motors

SureStep® Series Specifications – Connectorized Bipolar Stepping Motors										
Bipolar Stepping Motors		High Torque Motors					Higher Torque Motors			
		STP-MTR-17040	STP-MTR-17048	STP-MTR-23055	STP-MTR-23079	STP-MTR-34066	STP-MTRH-23079	STP-MTRH-34066	STP-MTRH-34097	STP-MTRH-34127
Price		<—>	<—>	<—>	<—>	<—>	<—>	<—>	<—>	<—>
NEMA Frame Size		17	17	23	23	34	23	34	34	34
Maximum Holding Torque	(lb-in)	3.84	5.19	10.37	17.25	27.1	17.926	26.738	50.159	80.7366
	(oz-in)	61.4	83	166	276	434	286.81	427.81	802.54	1291.77
	(N-m)	0.44	0.59	1.17	1.95	3.06	2.0253	3.0210	5.6671	9.121
Rotor Inertia	($oz\text{-}in^2$)	0.28	0.45	1.483	2.596	7.66	2.60	7.66	14.80	21.90
	($kg\text{-}cm^2$)	0.051	0.082	0.271	0.475	1.40	0.476	1.40	2.71	4.006
Rated Current (A/phase)		1.7	2.0	2.8	2.8	2.8	5.6	6.3	6.3	6.3
Resistance (Ω/phase)		1.6	1.40	0.75	1.10	1.11	0.40	0.25	0.30	0.49
Inductance (mH/phase)		3.03	2.65	2.36	3.82	7.70	1.18	1.52	2.07	4.14
Basic Step Angle		1.8°								
Shaft Runout (in)		0.002 in [0.051 mm]								
Max Shaft Radial Play @ 1lb load		0.001 in [0.025 mm]								
Perpendicularity		0.003 in [0.076 mm]								
Concentricity		0.002 in [0.051 mm]								
Maximum Radial Load (lb [kg])		6.0 [2.7]		15.0 [6.8]		39.0 [17.7]	15.0 [6.8]	39.0 [17.7]		
Maximum Thrust Load (lb [kg])		6.0 [2.7]		13.0 [5.9]		25.0 [11.3]	13.0 [5.9]	25.0 [11.3]		
Storage Temperature Range		-20°C to 100°C [-4°F to 212°F]								
Operating Temperature Range		-20°C to 50°C [-4°F to 122°F] (motor case temperature should be kept below 100°C [212 °F])								
Operating Humidity Range		55% to 85% non-condensing								
Weight (lb [kg])		0.7 [0.3]		1.5 [0.68]	2.2 [1.0]	3.9 [1.8]	2.3 [1.0]	3.8 [1.7]	6.1 [2.8]	8.8 [4.0]
Insulation Class		130°C [269°F] Class B								
Agency Approvals		CE (complies with EN55014-1 (1993) and EN60034-1:5.11)								
Design Tips		Allow sufficient time to accelerate the load and size the step motor with a 100% torque safety factor. DO NOT disassemble step motors because motor performance will be reduced and the warranty will be voided. DO NOT connect or disconnect the step motor during operation. Mount the motor to a surface with good thermal conductivity, such as steel or aluminum, to allow heat dissipation. Use a flexible coupling with "clamp-on" connections to both the motor shaft and the load shaft to prevent radial and thrust loading on bearings from minor misalignment.								
Accessory Extension Cable		STP-EXT-020					STP-EXTH-020			

Dynamixel
24/28 Series

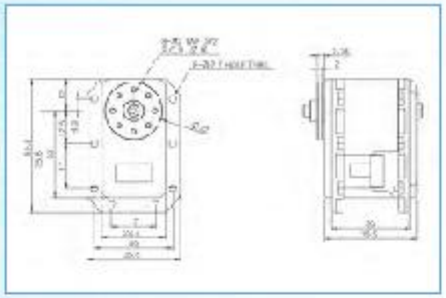

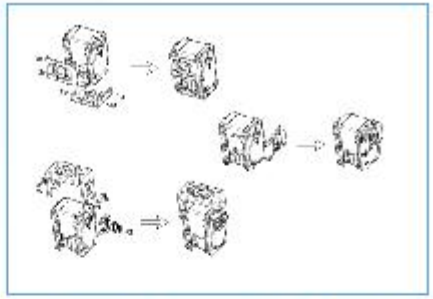

[24/28 Series Dyanmixels & Brackets](#)
(Click to View Full Line)

Model	RX-24F (Visit Product Page)	RX-28 (Visit Product Page)	MX-28 (Visit Product Page)
Stall Torque @ Max Voltage	2.6N.m (26.5 kg-cm)	3.7N.m (37.7 kg-cm)	3.1N.m (31.6 kg-cm)
Speed (RPM)	126	85	67
Nominal Operating Voltage	12v	12-18.5v	11.1-14.8v
Stall Current Draw	2.4A	1.9A	1.7A
Dimensions	35.6x50.6x35.5 mm	35.6x50.6x35.5 mm	35.6x50.6x35.5 mm
Weight	67g	72g	72g
Resolution	0.29°	0.29°	0.088°
Operating Angle	300	300	360
Gear Reduction	193 : 1	193 : 1	193 : 1
Geartrain Material	Hardened Steel	Hardened Steel	Hardened Steel
Onboard CPU	ATMega8 (ATMEGA8-16AU @ 16MHZ, 8 Bit)	ATMega8 (ATMEGA8-16AU @ 16MHZ, 8 Bit)	Cortex M3 (STM32F103C8 @ 72MHZ, 32 Bit)
Position Sensor	Potentiometer	Potentiometer	Magnetic Encoder
Com Protocol	RS-485	TTL	TTL/RS-485
Com Speed	1mbps	1mbps	3mbps
Compliance/PID	Compliance	Compliance	PID
Dimensional Drawing	PDF	PDF	PDF

http://www.trossenrobotics.com

Dynamixel
106 Series

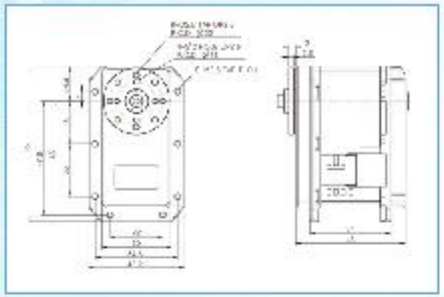

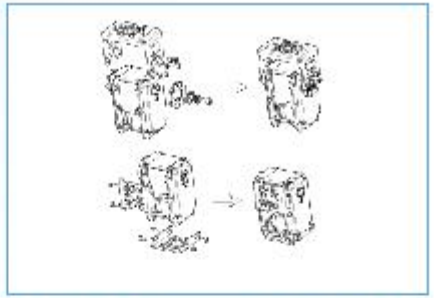

106 Series Dyanmixels & Brackets
(Click to View Full Line)

Model	EX-106+ (Visit Product Page)	MX-106 (Visit Product Page)
Stall Torque @ Max Voltage	10.9N.m (111 kg-cm)	10.0N.m (101 kg-cm)
Speed (RPM)	91	55
Nominal Operating Voltage	12-18.5v	11.1-14.8v
Stall Current Draw	7A	6.3A
Dimensions	40.2x65.1x46 mm	40.2x65.1x46 mm
Weight	154g	153g
Resolution	0.29°	0.088°
Operating Angle	251	360
Gear Reduction	184 : 1	225 : 1
Geartrain Material	Hardened Steel	Hardened Steel
Onboard CPU	ATMega8 (ATMEGA8-16AU @ 16MHZ, 8 Bit)	Cortex M3 (STM32F103C8 @ 72MHZ, 32 Bit)
Position Sensor	Magnetic Encoder	Magnetic Encoder
Com Protocol	RS-485	TTL/RS-485
Com Speed	1mbps	3mbps
Compliance/PID	Compliance	PID
Dimensional Drawing	PDF	PDF

http://www.trossenrobotics.com

Arduino MEGA 2560

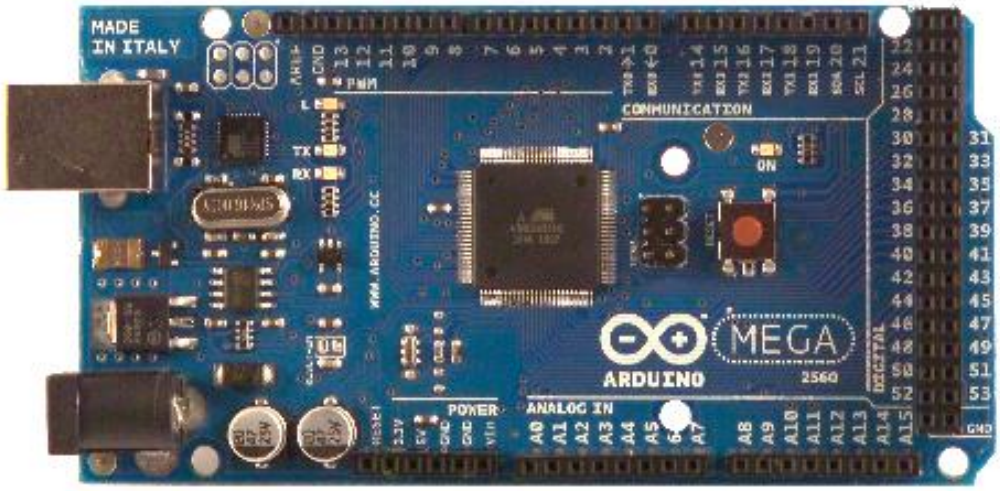

CE

Product Overview

The Arduino Mega 2560 is a microcontroller board based on the ATmega2560 (datasheet). It has 54 digital input/output pins (of which 14 can be used as PWM outputs), 16 analog inputs, 4 UARTs (hardware serial ports), a 16 MHz crystal oscillator, a USB connection, a power jack, an ICSP header, and a reset button. It contains everything needed to support the microcontroller; simply connect it to a computer with a USB cable or power it with a AC-to-DC adapter or battery to get started. The Mega is compatible with most shields designed for the Arduino Duemilanove or Diecimila.

Index

NETGEAR ProSafe

ProSafe® 5-port and 8-port Gigabit Desktop Switches 10/100/1000 Mbps

GS105v3, GS108v3

Data Sheet

Gigabit Power, 10/100 Simplicity

- Connects up to 10x faster than Fast Ethernet for maximum performance†
- Up to 60% lower power consumption[1]
- Auto power-down mode saves energy when port is unused
- Simple to combine Fast Ethernet and Gigabit devices in your network
- Plug-and-play installation delivers ease of use

Features

- ProSafe 5- and 8-port Gigabit Desktop Switches connect your network with the dual advantages of performance and convenience
- Fast, auto-switching Ethernet connection integrates 10, 100, and 1000 Mbps devices into your network
- Supports Windows® and Macintosh® platforms
- LEDs make it easy to monitor link, speed, and activity
- AutoUplink™ technology automatically adjusts for two common types of cables
- Compact metal case for desktop or wall mounting

NETGEAR Green

- Up to 60% lower power consumption[1]
- Auto power-down mode saves energy when port is unused
- Packaging manufactured with at least 80% recycled materials

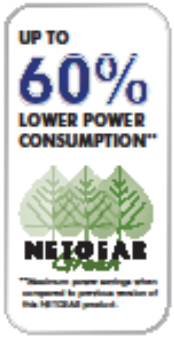

24/7 TECHNICAL SUPPORT

1-888-NETGEAR (638-4327)
Email: info@NETGEAR.com